Spectral Selective Coatings based on Aluminium Oxide and Related Materials

INAUGURALDISSERTATION

zur
Erlangung der Würde eines Doktors der Philosophie

vorgelegt der
Philosophisch-Naturwissenschaftlichen Fakultät
der Universität Basel

von
Jürgen Geng
aus Tiengen am Hochrhein (Deutschland)

Basel, 2000

Preface

The present thesis is the result of about three and a half year of research in the group of Peter Oelhafen at the Institute of Physics, University of Basel.

Questions of both fundamental and applied nature arose and especially this mixture was the major source of motivation. As a result, various problems were treated far from being solely relevant to the present topic. Such a wide field can only be cultivated in an open-minded research group and with help of external partners. Indeed, a lot of people participated in the development of ideas and new concepts, either by experimental support and/or fruitful discussions. They are gratefully acknowledged at the end of this report.

I have to admit that the spectral selective aluminium oxide coatings were *not only* the result of systematic investigations. Particularly the starting point was a miscarried trial to produce an aluminium mirror: a dark gray selective surface was the result. Usually, such a sample would have immediately been thrown into the litter bin – fortunately not in this case. Dr. Paul Gantenbein and Dr. Andreas Schüler encouraged me to get to the bottom of this effect and about half a year of misses and fallacies followed. Eventually, I identified a small leakage in the vacuum deposition system to be responsible. A systematic approach and the process optimization could be started, opening windows to some fascinating topics.

An accidental discovery is nothing one should be ashamed of. In fact, most of the important historical innovations were started by an accident and I am convinced there are more than confessed. Of course, the present work is only the result of a rather unimportant accident – compared to the invention of the X-ray tube, the discovery of radioactivity or the birth of many modern materials.

I would like to thank the proof-readers Dr. Teresa de los Arcos, Dr. Michael Gunnar Garnier and Renate Bächle for their critical remarks concerning both content and language.

Abbreviations

ABP	asymmetric bipolar pulsing
a-C:F	amorphous fluorinated carbon
a-C:H	amorphous hydrogenated carbon
AFM	atomic force microscopy
AM 1.5	atmospheric mass equivalent 1.5
CPE	constant pass energy
CRR	constant retardation ratio
DC	direct current
ESCA	electron spectroscopy for chemical analysis
ESEM	environmental scanning electron microscopy
EW - equation	Edward - Wilkinson equation [61]
FWHM	full width half maximum
FTIR	Fourier transform infrared
HV	high vacuum
IEA	international energy agency
IR	infrared
JDOS	joined density of states
KPZ - equation	Kardar - Parisi - Zang equation [62]
Me	placeholder for any metal
NIR	near infrared
PACVD	plasma assisted chemical vapour deposition
PES	photoelectron spectroscopy
PTFE	polytetrafluoroethylene
PVD	physical vapour deposition
QMB	quartz micro balance
RF	radio frequency (13.56 MHz)
RMS	root mean square
SEM	scanning electron microscopy
SOS - model	solid - on - solid model
STP	standard temperature and pressure
UHV	ultra high vacuum
UPS	ultraviolet photoelectron spectroscopy
UV	ultraviolet
VIS	visible light
XPS	X-ray photoelectron spectroscopy

Contents

Introduction 1

1 Basic concepts 5

1.1 Spectral selectivity 5

1.1.1 Different methods of producing the same 7

1.1.2 Figure-of-merit 8

1.2 Dynamical film growth 9

2 Experimental set-up 15

2.1 Film deposition 15

2.1.1 Magnetron sputtering 15

2.1.2 PACVD 18

2.2 Film characterization 18

2.2.1 Measurement of the deposition rate 18

2.2.2 Electron spectroscopy 18

2.2.3 Real-time specular reflectance measurement 23

2.2.4 Hemispherical, diffuse and direct reflectance 23

2.2.5 Determination of the surface morphology 24

2.2.6 Accelerated aging tests 25

3 Results 27

3.1 The absorber layer 27

3.1.1 Deposition rate 28

3.1.2 Electron spectroscopy 31

3.1.3 Real time process control 42

3.1.4 Optical properties 46

3.1.5 Structure and morphology 51

3.2 The cover layer 62

3.2.1 Al_2O_3 62

3.2.2 a-C:H 63

3.2.3 a-C:F 66

3.3 TiO_x: An alternative material? 73

4 Discussion 75
4.1 Deposition and chemistry 75
4.2 Dynamical growth and the random surface 76
4.2.1 Comparison with theoretical and numerical models 76
4.2.2 Comparison to other experimental results 81
4.3 Optics and applications 82
4.3.1 Absorbance and reflectance 82
4.3.2 Stability and wettability 83

Résumé 85

Related articles: 99

A Optical selective coatings based on microstructured aluminium oxide 101

B Changing TiN film morphology by plasma biasing 103

C Photoelectron Spectroscopy Study of Al-Cu Interfaces 105

D A Photoelectron Spectroscopy Study of Ti/Cu Interfaces 107

Acknowledgments 109

Introduction

The outstanding role of renewable energy for the future power generation is indisputable and shall not be outlined here once more. Besides photovoltaics and other solar based techniques, photothermal solar energy conversion is one of the major areas under current progress. Many of the essential problems have been solved up to now. Nevertheless, it is ever challenging to look for a better device with a higher figure-of-merit and new fields of applications. At this point, it is not sufficient to orient one's ideas only to the economical list of things desired. Fundamental research in new and putative old fields has to come into play. Thereby, existing knowledge has to be reopened and examined for a possible symbiosis. Materials science is a field where such interdependencies have long been recognized to be very fruitful. Chemistry, physics and, last but not least, biology have merged and each discipline contributes valuable impulses to the whole. This is particularly true for surface and interface science, e.g. sensorics, interface or surface engineering.

Spectral selectivity is a prerequisite for a satisfactory performance of a photothermal system. Thin film technology has proven to be one possibility to meet this demand by suitable layers or stacks. A short introduction to this field is given in section 1.1. One promising idea is to achieve spectral selectivity by so called *wavelength discrimination*, i.e. the electromagnetic peculiarities of a very rough surface with protuberances in the order of the wavelength of the visible light.

The properties of thin optical films do not only depend on the material under investigation but also on the interface chemistry and the growth dynamics. The latter is a fascinating and fairly new field of research forasmuch as it deals with nonlinear and/or nonlocal systems with their unforeseen properties. Various theoretical approaches for the description of random surface evolution have been proposed ([1] and references therein). They range from numerical kinetic simulations to continuum analytical models in which the local height $h(\vec{r}, t)$ at position $\vec{r}$ is studied as a function of deposition time t under the influence of different relaxation terms. Within the last years, a few theories intended to describe the counteracting of surface diffusion and shadowing during sputter deposition and erosion [2–8]. These models gave valuable insight in the mechanisms leading to columnar or needle-like surface structures. A short survey shall acquaint the reader with the peculiarities of this topic (section 1.2).

For its wide field of applications, e.g. as mirror or electrical contact material, aluminium films have drawn a lot of attention to the materials science community.

A self-similar aluminium surface morphology was discovered by Yan *et al.* [9], when AFM investigations were undertaken on magnetron sputtered aluminium films. Moreover, a fairly linear increase of the roughness with temperature was found. Unfortunately, the scaling behaviour was not determined in their work. On the contrary,

AFM studies by Lita and Sanches [10] revealed two different scaling regimes for magnetron sputtered pure Al films: Almost no roughening below 300 nm thickness and a roughness exponent of $\beta \approx 0.55$ above this limit.

Wan *et al.* [11] studied the evolution of magnetron sputtered aluminium films by SEM and TEM. A high power DC supply of about 10 kW was used, whereby the substrate temperature increased significantly from ambient temperature to 480°C after 5 min of deposition. They observed very rough films with a low density, while the appearing columnar structures grew with deposition time. This structure was suggested to result from a counteracting of defect production, preferential resputtering, enhanced diffusion, agglomeration and recrystallization of particles. Unfortunately, no details were given on the base pressure or any residual gas content.

It has long been recognized, that the optical properties of aluminium films are inherently related to the vacuum environment during their deposition. Typically, the optical constants change significantly even if only very low oxygen contamination is present [12, 13].

The performance of Al mirrors for large optical telescopes is related to an ultra low IR emittance. This motivated Wang *et al.* [14] to study the correlation of roughness, impurity level, IR emittance and sputter conditions. The main results were, that low working pressures, short target-substrate distances and a high purity process condition decreased the IR emittance. A similar study concerning the optical reflectance and roughness as a function of gas pressure and substrate temperature was presented by Furukawa *et al.* [15].

Several authors reported on the properties of aluminium - oxygen coatings with different oxygen content. Sproul *et al.* [16] produced gray aluminium films at an intermediate oxygen partial pressure (0.04 mTorr), while clear films were produced beyond 0.08 mTorr. Kelly and Arnell [17] identified a significant variation in coating structure with oxygen content. They proposed a new structure zone model describing pulsed magnetron sputtered aluminium oxide coatings. A chemical analysis by Stauder *et al.* [18] showed a mixture of a α-Al(O) supersaturated solid solution and amorphous Al_2O_{3-x} in the intermediate range between pure Al and amorphous Al_2O_3. Verkerk and Braenkart [19] utilized the growth properties of aluminium - oxygen coatings to develop diffusely reflecting layers for liquid crystal displays. The films were evaporated under a low but controlled O_2 or H_2O background pressure. This way, they were able to produce very rough metallic films with the desired reflection properties. For no and high oxygen content, however, rather smooth films were produced. Similar results were also found for aluminium alloys like Al-1%Si [20] and Al-20%Sn [21]. In the latter work, anomalous whisker growth and a pronounced roughness occurred in the presence of oxygen. Lee *et al.* [22] investigated the interdependence of oxygen partial pressure, baking temperature, refractive index and surface roughness for several metal oxides produced by ion beam sputter deposition. They found that there exists an optimum range of oxygen partial pressure and baking temperature to produce dielectric films with maximum optical quality.

By the growth models and experimental observations of rough sputter deposited films and the relation between oxygen impurity level and optical properties one is encouraged to search for a set of optimum parameters which leads to very rough, metallic AlO_x films[1]. In this way, it should be possible to achieve a suitable surface

[1] In the following, MeO_x denotes non-stoichiometric oxides, not necessarily homogeneous, i.e.

structure to develop a spectral selective behaviour.

In this work, the chemical properties, e.g. bonding type, metallic nature and interface chemistry, were investigated by photoelectron spectroscopy. The dynamical growth was followed by surface profile data (AFM, SEM) and *real-time* specular reflectance measurements. The optical properties were identified by spectrophotometry and correlations were found between the optical and the morphological results.

The report in hand is structured as follows: The first chapter is designed to acquaint the reader with the basic concepts of spectral selectivity and dynamical film growth. After that, a short description of the experimental set-up and the data evaluation is presented. Chapters 3 and 4 deal with the experimental results and their discussion. Finally, a résumé in form of a short summary and some prospects for future work is given. The appendices consist of publications, which were written in the course of this work and which are related to the topic presented here. If necessary, they are referred to.

---

including composite Me-Me_xO_{1-x} materials

Chapter 1

Basic concepts

1.1 Spectral selectivity

A solar thermal system should almost perfectly convert the solar light into heat. For this reason, one crucial part of such a system is the light absorbing surface. It collects the fraction

$$\alpha_{\rm s} = \frac{1}{I_{\rm s}} \int\limits_0^{\infty} \int\limits_0^{2\pi} \int\limits_0^{\pi/2} [\alpha(T,\lambda,\vartheta,\varphi) \cdot j_{\rm s}(\lambda,\vartheta,\varphi)] \cos\vartheta \, sin\vartheta \, d\lambda \, d\varphi \, d\vartheta \tag{1.1}$$

of the incoming light current

$$I_{\rm s} = \int\limits_0^{\infty} \int\limits_0^{2\pi} \int\limits_0^{\pi/2} j_{\rm s}(\lambda,\vartheta,\varphi) \; \cos\vartheta \, sin\vartheta \, d\lambda \, d\varphi \, d\vartheta \quad . \tag{1.2}$$

φ and ϑ are the polar and azimuthal angles for the incident light of wavelength λ. $j_s(\lambda,\vartheta,\varphi)$ denotes the intensity of the actual solar spectrum per solid angle $d\Omega = \sin\vartheta \, d\vartheta \, d\varphi$ and wavelength interval $d\lambda$. $\alpha(T,\lambda,\vartheta,\varphi)$ is the angle and wavelength dependent absorbance of the surface, which may be explicitly a function of the absorber temperature T. The additional $\cos\vartheta$ expresses a *Lambertian* behaviour of the surface. This means, that the absorber area A is reduced to $A\cos\vartheta$ when viewed from an angle ϑ. This behaviour is strictly speaking only valid for a black body and is an approximation otherwise [23].

The solar absorbance $\alpha_{\rm s}$ is only one side of the story. Every surface with $T > 0\,{\rm K}$ emits thermal radiation according to the *Stefan-Boltzmann* law

$$I_T = \varepsilon_T \, \sigma \, T^4 \quad , \tag{1.3}$$

where

$$\varepsilon_T = \frac{1}{I_{\rm BB}} \int\limits_0^{\infty} \int\limits_0^{2\pi} \int\limits_0^{\pi/2} [\varepsilon(T,\lambda,\vartheta,\varphi) \cdot j_T(\lambda)] \cos\vartheta \, sin\vartheta \, d\lambda \, d\varphi \, d\vartheta \tag{1.4}$$

is the thermal emittance of the body and

$$I_{\rm BB} = \int_0^{\infty} \int_0^{2\pi} \int_0^{\pi/2} j_T(\lambda)\ \cos\vartheta\, sin\vartheta\, d\lambda\, d\varphi\, d\vartheta \qquad (1.5)$$

the heat radiation of a black body at temperature T. Here, φ and ϑ are the polar and azimuthal angles for the *emitted* light of wavelength λ. Moreover,

$$j_T(\lambda) = \frac{2hc^3}{\lambda^5} \frac{1}{e^{\frac{hc}{kT\lambda}} - 1} \qquad (1.6)$$

is the black body radiation current density per solid angle and wavelength interval according to *Planck's* law.

In the ideal case of no parasitic heat sink, a hot surface therefore receives an amount of energy which is equal to the difference between the absorbed light (characterized by α_s) and the heat radiation it emits (characterized by ε_T). One may therefore think of a surface with $\alpha_s \equiv 1$ and $\varepsilon_T \equiv 0$ for all values of λ. However, *Kirchhoff's* law tells us

$$\alpha(T, \lambda, \vartheta, \varphi) = \varepsilon(T, \lambda, \vartheta, \varphi) \qquad \forall\, \lambda \quad , \qquad (1.7)$$

which is a consequence of thermodynamics, so that it is impossible to construct a surface which absorbs light of wavelength λ and does not simultaneously emit thermal radiation at this wavelength. A comprehensive textbook survey on the absorption, reflection and emission of light is given by Würfel [23].

Fortunately, the solar spectrum and the black body radiation at typical absorber temperatures, e.g. 100°C, are well separated as can be seen in figure 1.1. A step-like function for α_s and ε_T is therefore appropriate if the absorbance for sunlight is intended to be maximum and the thermal radiation minimum. Another important relation for the experimental determination of the optical parameters for opaque surfaces follows from energy conservation:

$$R(T, \lambda, \vartheta, \varphi) = 1 - \alpha(T, \lambda, \vartheta, \varphi) \quad , \qquad (1.8)$$

where $R(T, \lambda, \vartheta, \varphi)$ is the so called *hemispherical reflectance*, i.e. integrated over all reflection angles. If one assumes only near normal incidence ($\vartheta \approx 0$), rotational symmetry and a temperature independent absorbance, equation (1.8) reduces to

$$R(\lambda) = 1 - \alpha(\lambda) \quad . \qquad (1.9)$$

A step-like near normal hemispherical reflectance $R(\lambda)$ is therefore aspired for a selective surface. Figure 1.1 illustrates these principles for both the ideal case and an aluminium oxide film produced in this work. The optimum step position depends strongly on the temperature of the absorber and therefore on the field of application (see also section 1.1.2).

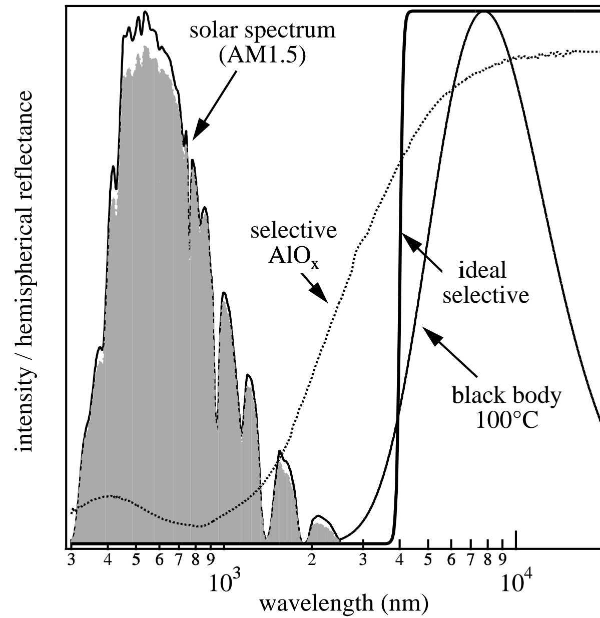

Figure 1.1: Principles of spectral selectivity. The solar spectrum is well separated from the black body radiation at 100°C. An ideal selective surface should have a step-like hemispherical reflectance (black line). The step position depicted in the graph is optimum for an absorber at 100°C and without concentration of the sunlight [24]. The near normal hemispherical reflectance of a real selective surface of AlO_x produced in this work (shallow dotted line) is also shown. The gray area is the absorbed fraction of the incoming solar radiation.

1.1.1 Different methods of producing the same

There are numerous articles, books and patents reporting on methods to achieve selectivity [24–26]. Here, only a few examples shall be given.

Some homogeneous materials show intrinsic selectivity, i.e. HfC or W [24,25], metals with an appropriate plasma edge position. However, none of these materials found up to now have a figure-of-merit (see section 1.1.2) which is satisfying for a standard application.

Most of the research has therefore concentrated on composite articles like absorber - reflector tandems. Such a tandem utilizes the IR reflectance of a substrate material like copper or aluminium and the UV-VIS absorbance of an IR-transparent film on top of it. The absorber material may, for instance, be a semiconductor with a band gap chosen so to let the infrared pass and absorb the visible. Another possibility is to choose a so called *composite* or *cermet* layer. These layers consist of a dielectric matrix which includes small metal particles. A few examples are Me-Al_2O_3 [25, 27, 28], Me-AlN [29, 30] or a-C:H/Me [31, 32] films, among many others. The selectivity is achieved by a phenomenon comprehensively described elsewhere [33–39]. Furthermore, some of these materials are designed to have a multilayered structure or graded refractive index to increase selectivity by interference effects. The simplest application of this method is a $\lambda/4$ antireflecting top coating.

Another promising mechanism has also been widely used for the establishment of deep black or selective surfaces [40–46]: the peculiarities of textured and random rough surfaces interacting with electromagnetic radiation, also called *wavelength discrimination* ([24] and references therein). As an example, niobium whiskers have been produced in our group [47] with protuberances in the order of the wavelength of the visible light. These irregularities scatter the visible light by a large extend and therefore, if there is some absorbance, it is significantly increased. However, for long IR waves, the surface appears to be flat and mirror-like. In principle, this effect can be easily understood by such simple arguments. But, a correct theoretical description of the crossover regime is still required [48]. For wavelengths much larger than the correlation length of the surface structures, *effective medium theories* [33, 34] and classical perturbation theories [48–54], i.e. the *Born* approximation, are applicable. The former are also used to describe the optical phenomena for composite films, the latter to describe the scattering from evoluting random growth fronts (see section 1.2). On the contrary, if wavelengths are much smaller than the surface structures, classical ray optics applies. However, none of these *classical* theories covers the intermediate regime.

The aluminium oxide films presented in this work take advantage of *all* the mechanisms mentioned above. These films consist of an inhomogeneous Al-Al_2O_3 metallic cermet, have a very high surface roughness and are covered with an antireflection coating to decrease reflection losses.

1.1.2 Figure-of-merit

The efficiency of a solar energy collector, i.e. the ratio of extracted heat flux I_Q to the incident solar power density is given by

$$\eta := \frac{I_Q}{CI_s} = \alpha_s - \frac{\varepsilon_T \sigma T^4 - \varepsilon_{T_0} \sigma T_0^4}{CI_s} \quad , \tag{1.10}$$

where T is the absorber temperature and T_0 the ambient temperature. If the incident solar flux I_s is concentrated before it hits the absorber, $C > 1$ denotes the concentration factor of the system.

The maximum absorber temperature is adopted for $\eta = 0$, that is, when no heat is extracted. Under the assumption that the thermal emittance is only slightly depending on the absorber temperature ($\varepsilon_T \approx \varepsilon_{T_0}$), this maximum temperature is solely determined by the ratio α_s/ε_T. This ratio is sometimes overemphasized as it is used as *the* figure-of-merit for a selective surface. But, as a matter of fact, almost all systems extract heat and therefore work below their maximum temperature. So the efficiency is determined by α_s and ε_T separately. For example, even at small values of C and moderate temperatures, ε_T loses its importance compared to α_s. Moreover, a surface with $\alpha_s = 1$ and $\varepsilon_T = 0.1$ wins in comparison to another with $\alpha_s = 0.5$ and $\varepsilon_T = 0.05$ under nearly all conditions, though their α_s/ε_T value is identical. A detailed survey on this topic is given by Seraphin and Meinel [24].

Therefore, the figure-of-merit of a solar absorber is the energy efficiency $\eta(T, T_0, C, I_s)$, rather than just the ratio α_s/ε_T.

1.2 Dynamical film growth

The evolution of a boundary far from equilibrium, called *dynamical growth*, is an interdisciplinary topic not only restricted to *interfaces* in the common sense, i.e. between two phases or media. Some other examples would be the *interface* between a growing cell cluster and its surrounding, a city-environs boundary, a coast line, the evoluting surface of the alps or the boundary of a galaxy. Though the time and length scales for these examples vary over a wide range, they can be described by the same basic concepts. The laws of thermodynamics fail in providing a theoretical description and other models have to come into play.

Obviously, when dealing with thin film growth the word *interface* belongs to the boundary between the growing film and the process gases involved, i.e. the *surface*. The dynamical properties of a surface are based on

- deposition rate, i.e. the number of particles per unit time impinging on the surface
- sticking probability
- reemission of particles
- adatom mobility and relaxation mechanisms
- substrate temperature, which influences the time scale for a rearrangement of particles
- angle of incidence
- impurities
- ...

Moreover, interdependencies of these parameters are expected. A profound discourse on the basic concepts and mathematical descriptions is presented by Barabási and Stanley [1] or Krug [55]. In the following, only a short overview is given.

Basic ideas

First, let us consider the so called *solid-on-solid* model (SOS-model), which neglects voids and holes during film growth. Therefore, the surface height at a point x and time t is unambiguously assigned to a single valued function $h(x,t)$. The mean value of this function is given by[1]

$$\bar{h}(t) = \frac{1}{L}\int_0^L h(x,t)\,dx \qquad (1.11)$$

[1] For the sake of simplicity, some formulas are given in their 1D form

with the system size L. In the case of constant deposition rate, this value increases linearly with time. The roughness of the surface is characterized by the so called *interface width*

$$w(L,t) = \sqrt{\frac{1}{L}\int_0^L [h(x,t) - \bar{h}(t)]^2\, dx} \quad , \tag{1.12}$$

i.e. the RMS deviation from the mean height. In the *dynamic scaling* approach, the interface is assumed to have a *self-affine* shape with a width of the form[2]

$$w(L,t) = L^{\alpha}\, f\left(\frac{t}{L^z}\right) \quad . \tag{1.13}$$

$f(\varrho)$ is a scaling function with the asymptotic behaviour

$$f(\varrho) \sim \begin{cases} \varrho^{\beta} & for \quad \varrho \ll 1 \\ const & for \quad \varrho \gg 1 \end{cases} \quad . \tag{1.14}$$

Though it has proven to be very fruitful for the description of dynamical growth [1], there is no rigorous evidence for the scaling hypothesis described by equation (1.13) [56, 57]. Of course, the *self-affinity* of a random surface is only valid in a statistical sense, i.e. the surface shows the same *statistical properties* under a certain rescaling of x, h and – in the case of a dynamical process – t.

A function very closely related to the interface width is the ensemble averaged *local width* $\omega(r,t)$. It measures the interface width for a finite window of size r, which means that L is replaced by r in equation (1.12) and that an ensemble average is performed. The local width is very useful for a description of large systems, i.e. $L \to \infty$.

The square of the local width shows the same scaling behaviour as the *equal time height-height correlation function*, which measures the ensemble averaged height difference between two points separated by a d-dimensional vector $\vec{r}$.

The relationship between $\omega(r,t)$ and $w(L,t)$ for a large system under the assumption of an isotropic surface is given by (see e.g. [54])

$$\omega(r,t) = w(t)\; g\left(\frac{r}{\xi(t)}\right), \quad L \gg \xi(t) \quad , \tag{1.15}$$

where $\xi(t)$ is the lateral correlation length, $w(t) = \lim_{L\to\infty} \omega(L,t)$ and $g(\varrho)$ a scaling function of the form

$$g(\varrho) = \begin{cases} \varrho^{\alpha} & for \quad \varrho \ll 1 \\ 1 & for \quad \varrho \gg 1 \end{cases} \quad . \tag{1.16}$$

[2]Sometimes denoted by *Family-Vicsek* scaling

From equations (1.12) to (1.16) one can deduce the asymptotic behaviour of $\omega(r,t)$:

$$\omega(r,t) \sim \begin{cases} r^{\alpha} & for \quad r \ll \xi(t) \sim t^{1/z} \\ w(t) \sim t^{\beta} & for \quad r \gg \xi(t) \end{cases} \quad . \tag{1.17}$$

To get an idea of the properties of this function, imagine a Sunday walk along a straight way within the alps. The roughness or strictly speaking the *local width* ω of your path certainly depends on the distance r you go: it will be only a few centimetres if you take a step, but much larger if you go ten kilometres. Furthermore, it will not increase anymore after a certain distance, even if you traverse the alps totally[3]. This distance is called the *lateral correlation length* $\xi(t)$, where t is a time scale, in which the alps were folded. In fact, there was no test person to investigate the early stages.

α, β and z are called *roughness*, *growth* and *dynamic* exponent, respectively. In particular, they are not independent for processes obeying the scaling law equation (1.13), but are linked by the relation $z = \alpha/\beta$ [1,55]. There is a peculiarity with the roughness exponent α, which is worth to be mentioned. It is not a measure of the roughness itself but of how it changes with length scale [58]. A certain set (α,β,z) characterizes a unique *universality class* of dynamical growth.

Theoretical models

There exists a large number of theories to describe the dynamical growth of surfaces and interfaces. A few of them shall be shortly outlined here to introduce their fundamental ideas.

One approach is to simulate the deposition process by lattice models using simple sticking and relaxation rules (*kinetic models*). As an example, in the *random deposition model* particles fall down vertically onto a surface where they instantaneously stick. No interparticle force or relaxation is taken into account. The incoming particle flux is assumed to be random and not correlated in both space and time. As a consequence, the surface evolves also in an uncorrelated way, because the growth velocity at a certain position does not depend on the height of the neighbouring sites. More sophisticated models are comprehensively studied in [1], e.g. the *ballistic deposition* or the *random deposition with surface relaxation.* A very famous model is the *Eden-model*, developed to describe the growth of densely packed cell colonies [59]. It was the first model studied in the framework of dynamical scaling and self-affinity [56,57]. These classical kinetic models base on instantaneous sticking and relaxation. Giving up this simplification, Sarma and Tamborena [60] discovered a new universality class for molecular beam epitaxy with a growth exponent of 0.375.

In contrast to the kinetic models, *stochastic growth equations* are continuum models of the general form

$$\frac{\partial h(\vec{r},t)}{\partial t} = F(h, \nabla h, \nabla^2 h, (\nabla h)^2, \ldots, \vec{r}, t) + \eta(\vec{r},t) \quad . \tag{1.18}$$

[3] Under the assumption, that you don't take only special paths which cross the Mont Blanc always at the end.

η denotes an uncorrelated noise originating from the deposition process, for instance. A certain growth equation is often closely related to a corresponding kinetic model. The first nontrivial *linear* stochastic equation was introduced by Edward and Wilkinson (*EW - equation*) [61], which includes a *surface tension* term ($\sim \nabla^2 h$), smoothing out the surface. This model belongs to the same universality class as the kinetic *random deposition with surface relaxation*. The EW-equation can be analytically solved, whereby the roughness exponent for a two dimensional ($d = 2$) lattice is zero. Therefore, it is not able to describe macroscopic surface roughening, although it leads to a correlated surface.

A lot of attention is paid to the *nonlinear* equation introduced by Kardar, Parisi and Zhang (*KPZ - equation*) [62]. In addition to the surface tension term of the EW - equation, the nonlinear, quadratic term $\nu(\nabla h)^2$ was added. It describes the growth (or erosion) at positions of strong local slopes, e.g. at step edges. The scaling exponents for the KPZ-equation are unambiguous for $d = 1$: $\alpha = 1/2$, $\beta = 1/3$ and $z = 3/2$. However, in $d \geq 2$ they depend on the strength of the different terms and only numerical results are known (see e.g. [63, 64]). Particularly, the KPZ-equation leads to an excess velocity $\partial \langle h \rangle / \partial t$ of the surface, even if the *driving force*, i.e. the deposition rate, is zero. This means that mass conservation is violated. Furthermore, it does not describe structures with large columns and deep grooves, which have been found to be typical for sputter deposited films [65–67]. Structures like these were especially reported for aluminium [9, 14, 68] and aluminium - oxygen coatings [17].

From a theoretical point of view, one should be able to describe sputter deposition and erosion by the same mathematical framework. Therefore, nonlinear growth equations were also set up to describe the peculiarities of surface roughening during sputter erosion [69–71], e.g. the ripple formation in silver [72] or the self-affine properties of sputtered graphite [73].

All these theories and models are *local*, i.e. F has been set as a function of the local properties ∇h, $\nabla^2 h$, $(\nabla h)^2, \ldots, \vec{r}, t$ only. However, shadowing of incident particles by surface protuberances may have a significant influence on the evolution of a rough surface. In particular, this is true if the angle of incidence is distributed over a wide range - as it is for sputter deposition. Therefore, the whole set of $\{h(\vec{r}, t)\}$ has to be taken into account. *Non-local* models [3–8] take the influence of this effect into consideration. These non-local models will be discussed in chapter 4.

Experimental methods of morphology characterization

Experimental techniques to determine the roughness properties of a surface or interface are numerous. Obviously, scanning probe microscopy is well suited to get direct access to the surface topography. Both AFM (atomic force microscopy) and STM (scanning tunnel microscopy) have been used in this field [9, 73–76].

Electron microscopy, i.e. SEM and TEM, is also widely used for structure and morphology characterization. As an example, Thornton worked out a so called *three - zone model* for the growth of sputtered thin metal films on the basis of side view SEM micrographs [67].

In contrast to this real-space methods, diffraction techniques are able to measure the $\vec{k}$ - space properties of a surface profile. In principle, the reflectance of a surface

is completely determined by the optical constants and the statistical properties of the surface. However, as already pointed out in section 1.1.1, most of the theoretical calculations rely on perturbation expansions. The same also holds for many experimental diffraction techniques used to characterize the surface roughness. Indeed, for the major part of technical applications, one is interested in perfectly flat surfaces, e.g. mirrors, and the roughness is in fact only a small perturbation of the flat surface. Within diffraction techniques, angle-resolved X-ray [75–79], electron and light scattering [80–83] are employed for different length scales.

Chapter 2

Experimental set-up

2.1 Film deposition

The films investigated throughout this work were predominantly prepared by plasma assisted deposition techniques. These include magnetron sputtering, reactive magnetron sputtering, plasma assisted chemical vapour deposition (PACVD) and combinations of these.

Figure 2.1 shows a schematic drawing of the high vacuum (HV) deposition chamber with a volume of approximately 150 l. A conventional turbomolecular - rotary pumping unit establishes a minimum base pressure of $5 \cdot 10^{-7}$ mbar. However, the pressure can be improved by one order of magnitude with the aid of a liquid nitrogen cooling trap. Three mass flow controllers[1] regulate the gas flow of the different working gases. Moreover, the process pressure can be adjusted by a throttle valve which controls the pumping speed. The substrates are located on a rotatable carousel to place them in the desired position. The substrate holder can be heated up to a maximum of 400°C and the temperature is measured by a chromel-alumel thermocouple at the backside. Furthermore, this holder can be electrically connected to a DC voltage supply for biasing. Substrate precleaning can be done with a *Kaufmann* ion source[2] with typical 8 mA beam current at an acceleration voltage of 500 V. By means of a sample dispenser system it is possible to mount up to eleven substrates during a series of depositions without breaking the vacuum. A small HV system is set up to transfer samples *in situ* to a photoelectron spectroscopy analyzer (section 2.2.2).

In the following, short descriptions of the deposition techniques are presented.

2.1.1 Magnetron sputtering

Owing to its ability for the deposition of high quality films at high deposition rate and low process pressure, the magnetron sputtering technology has emerged as one of the most important working horses for thin film production [84]. In principle, magnetron sputtering is, among conventional diode sputtering and ion source sputtering, one realization of physical vapour deposition (PVD). In PVD, charged ions

[1] MKS PR-3000
[2] ION TECH Model 3.0-1500-100

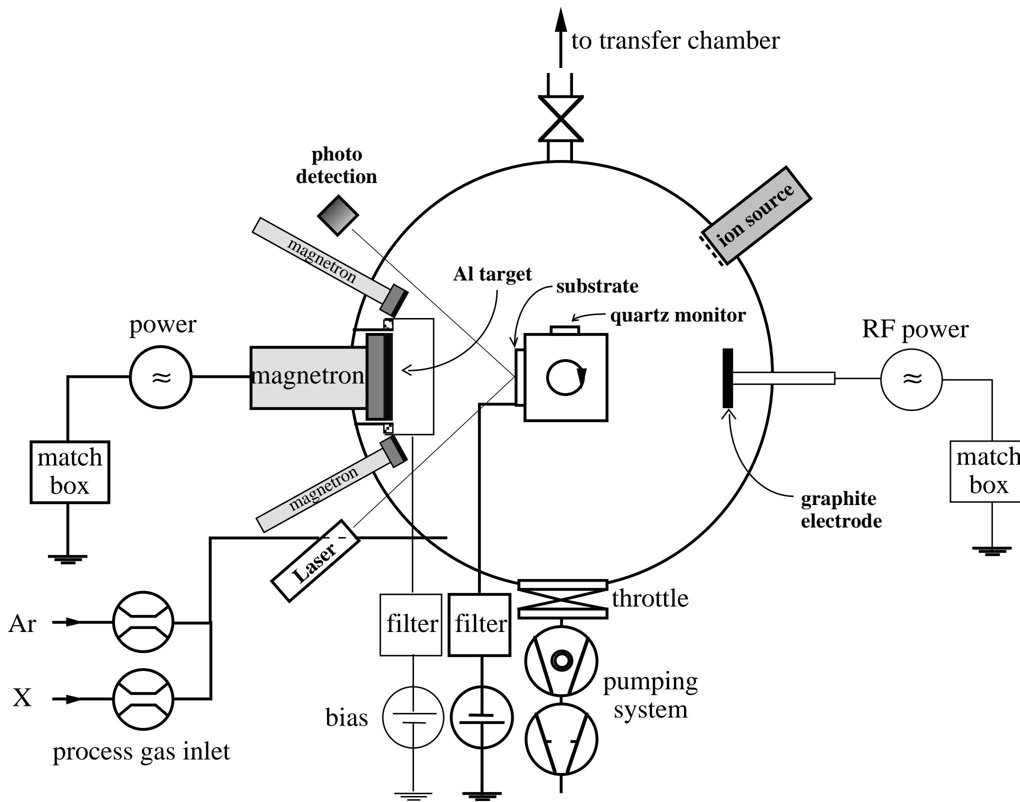

Figure 2.1: Schematic drawing of the deposition chamber

are accelerated by a potential drop towards a target electrode. As a result, atoms are disentangled from the target and deposited on the counter surface.

The magnetrons used in this work consist of planar circular cathodes backed by water cooled permanent magnets and covered by sheets of pure metal target material. The magnetic field in front of the target causes an extended path length for plasma electrons, resulting in a higher collision rate and therefore in an increased density and confinement of the plasma in the vicinity of the target. Because the magnets are arranged to form a toroidal confinement field the target erosion is inhomogeneous, forming a ring shaped groove (see e.g. [84]). The whole sputtering assembly consists of a central large magnetron of about 10 cm diameter and two smaller ones (2.5 cm in diameter) symmetrically arranged (figure 2.1). Thereby, the outer magnetrons are equipped with identical targets to improve film homogeneity. This way, a simultaneous co-deposition of two different target materials is possible. However, most of the samples presented here were prepared by only using the central magnetron. Examples for the use of the outer magnetrons can be found in [85] and the diploma thesis of Springer [86], who characterized nickel containing aluminium oxide films.

The target-substrate distance can be varied from 3 to 8 cm by moving the target cathode. Biasing of the substrate enables one to alter the energy and flux of charged particles to the growing film. Alternatively, an additional electrode close to the plasma region was mounted to change the plasma potential (see also Appendix B). The latter method was employed for its better feasibility in large area deposition

systems.

In order to form metal oxide films of different stoichiometry, a noble-gas / oxygen mixture was fed into the reactor at a total gas flow of 40 sccm (cubic centimetre per minute at STP). The typical process pressure was $1.7 \cdot 10^{-2}$ mbar. A detailed investigation on the deposition parameters is given in section 3.1.1.

Several different commercially available power supplies were used to drive the magnetrons: DC power[3], RF power[4] and asymmetric bipolar pulsed (ABP) power[5]. The latter turned out to be very stable in the transition regime between metallic and oxidic deposition while it provides a high deposition rate at moderate power (section 3.1.1).

It is well known that undesirable arcing and microarcing (dielectrical breakdown) occurs during DC reactive sputtering of metal oxides from metal targets [16,17]. This is caused by charging of insulating oxidic regions on the target surface, the so called *poisoned* areas. Even for low oxygen partial pressure, in the metallic regime of the target, microarcs were observed on non-eroded parts. Asymmetric bipolar pulsing overcomes this problem by periodic short pulses of the opposite polarity (figure 2.2). During these pulses any charging of oxidic areas is discharged by plasma electrons attracted to the positive surface. Moreover, the Ar^+ bombardment of the insulating areas is supported [87, 88]. Nevertheless, the high deposition rate known from DC sputtering is maintained because the duty cycle is small, i.e. short moderately biased pulses are sufficient.

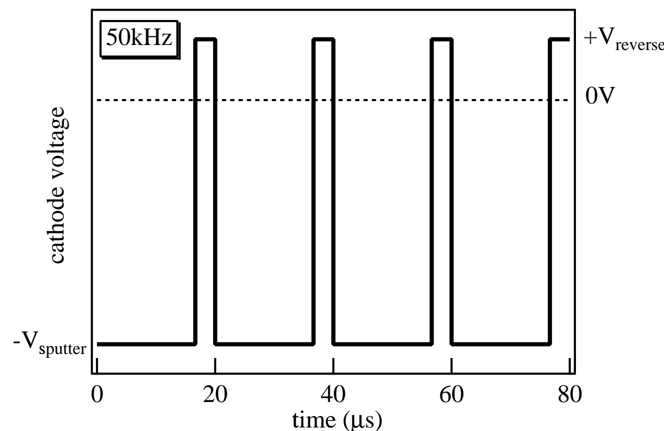

Figure 2.2: Cathode voltage *vs.* time for a pulse frequency of 50 kHz and a duty cycle of 20 %

RF sputtering is an alternative approach to solve the problem of arcing in reactive sputtering. It usually employs a sinusoidal plasma excitation at 13.56 MHz, capacitively coupled to the target electrode. The difference in mobility of electrons and ions results in a DC potential drop in front of the target, the so called *self bias*.

[3] MDX Magnetron Drive, Advanced Energy
[4] RFX-600 and corresponding matching network ATX-600, Advanced Energy
[5] RPG-50, ENI Power Systems

Typical values of a few hundreds of volts form at a power of about 100 W RF. However, the deposition rate is considerably lower than the DC value at the same power level [17, 89] (see also section 3.1.1).

For these reasons, most of the oxidic films in this work were produced by pulsed magnetron sputtering, typically at 50 kHz, 5 % duty cycle (1056 ns) and 80 W. Besides, to investigate the influence of the discharge parameters on the growth, variation of the pulse frequency and power was undertaken (see e.g. section 3.1.1).

2.1.2 PACVD

The a-C:H (amorphous hydrogenated carbon) and a-C:F (amorphous fluorinated carbon) top layers presented in section 3.2 were produced by PACVD. As in conventional CVD, the film grows from precursors in the gas phase. In the plasma, however, energetic electrons are able to break chemical bonds, activate molecules and initiate chemical reactions, which would require elevated substrate temperature in conventional CVD.

The a-C:H and the a-C:F films originate from CH_4 and C_3F_8 precursors, respectively. In the former case, the magnetron was operated with pure CH_4 gas. As a result, the aluminium target was intentionally poisoned with a carbon layer to avoid aluminium atoms to be sputtered. This method was not feasible in the case of a-C:F (see section 3.2). Therefore, it was necessary to add an additional RF driven graphite electrode (figure 2.1) to produce these layers without any metal incorporation.

2.2 Film characterization

The deposited films were investigated by a variety of different techniques, which may be divided into *in situ* methods (sections 2.2.1-2.2.3), i.e. without breaking the vacuum, and *ex situ* methods (sections 2.2.4-2.2.6) after removing the samples from the deposition chamber.

2.2.1 Measurement of the deposition rate

In reactive magnetron sputtering, the deposition rate often undergoes drastic changes as a function of reactive gas content, as a consequence of target poisoning. Therefore, it is inalienable to follow this parameter, which, properly interpreted, even gives insight into some characteristics of the growing film. The deposition rate was monitored *in situ* by a quartz micro balance (QMB). This method measures the mass increase on a piezoelectric crystal by following the natural frequency changes of an oscillating circuit. Because only the mass deposition and not the thickness is directly accessible this way the latter was also determined *ex situ* by a step profilometer[6].

2.2.2 Electron spectroscopy

One of the most interesting features of a growing film is its electronic structure, which is directly related to physical and chemical properties. A powerful tool in this

[6] α-step, Tencor Instruments

field is photoelectron spectroscopy (PES or ESCA). It employs the photoelectric effect by an energy dispersive measurement of the electron ejection rate from the sample. Because of the inherent surface sensitivity of a few monolayers of atoms PES allows to study the electronic and related properties of surfaces and interfaces during their stepwise formation. XPS (X-ray photoelectron spectroscopy) supplies valuable information concerning both stoichiometry (peak areas) and chemical state (peak shifts) of the atomic species. Moreover, the UPS (ultraviolet photoelectron spectroscopy) technique maps valence states and it clearly identifies metallic material via the existence of a Fermi edge.

Principles

Photons of energy $h\nu$ impinging on the sample release electrons from bounded states (binding energy E_B with respect to the Fermi level $E_\mathrm{F} \equiv 0$). Owing to this photoionization (step 1) core holes are left and screening effects come into play. During their way to the surface some of the electrons suffer energy losses due to interactions with the solid, e.g. plasma excitations, inelastic electron-electron and electron-phonon scattering (step 2). Furthermore, they have to traverse the surface region to leave the sample and therefore to overcome the workfunction Φ (step 3). Eventually, the undisturbed electrons enter the vacuum with a kinetic energy

$$E_\mathrm{kin} = h\nu - |E_\mathrm{B}| - \Phi \quad , \tag{2.1}$$

referred to the vacuum level $E_\mathrm{vac} = 0$.

A photoelectron spectrum consists therefore not only of features corresponding to undisturbed primary electrons of energy E_B but also of electrons with discrete energy losses (plasmon excitations) and an additional broad featureless background of inelastically scattered electrons.

This model, the so called *three step model* [90], which is undoubtably a simplification of the actual multi-particle problem, has proven to be very fruitful for the interpretation of experimental data. A detailed description and a presentation of more rigorous models can be found in [91, 92].

The peak area of the primary peak is proportionate to the amount of excited atoms and the transition matrix element for the photoionization process. In classical perturbation theory [93], the photoionization cross section is calculated using *Fermi's golden rule* and the dipole approximation for the interaction of the electron with the photon field:

$$\sigma_{fi} \sim \frac{2\pi}{\hbar} \cdot |\langle f|\vec{r}|i\rangle|^2 \cdot \delta(h\nu - (E_f - E_i)) \quad . \tag{2.2}$$

The delta-functional expresses energy conservation[7]. A quantitative XPS analysis can be done by employing theoretical ionization cross sections (e.g. [94]) or using reference measurements.

A key feature of ESCA is that atomic states appear at different binding energy, depending on their chemical surrounding. This peculiarity, called *chemical shift*, often

[7] For crystalline systems $\vec{k}$- conservation is also obeyed but it is relaxed for disordered materials

allows to distinguish between atoms belonging to different chemical compounds. An Al 2s core level, for instance, appears at 117.9 eV in metallic aluminium, whereas in alumina it has a binding energy of about 120.8 eV. An atomic level of higher oxidation state (e.g. Al in Al_2O_3) typically shows a higher binding energy due to the extra coulombic potential the electron has to overcome to leave the core hole.

The apparatus

Experimental details of the ESCA system used in the main part of this work follow. However, some of the experiments presented in the appendices were performed on different machines. For details concerning these apparati the reader is referred to the experimental sections of the appended articles.

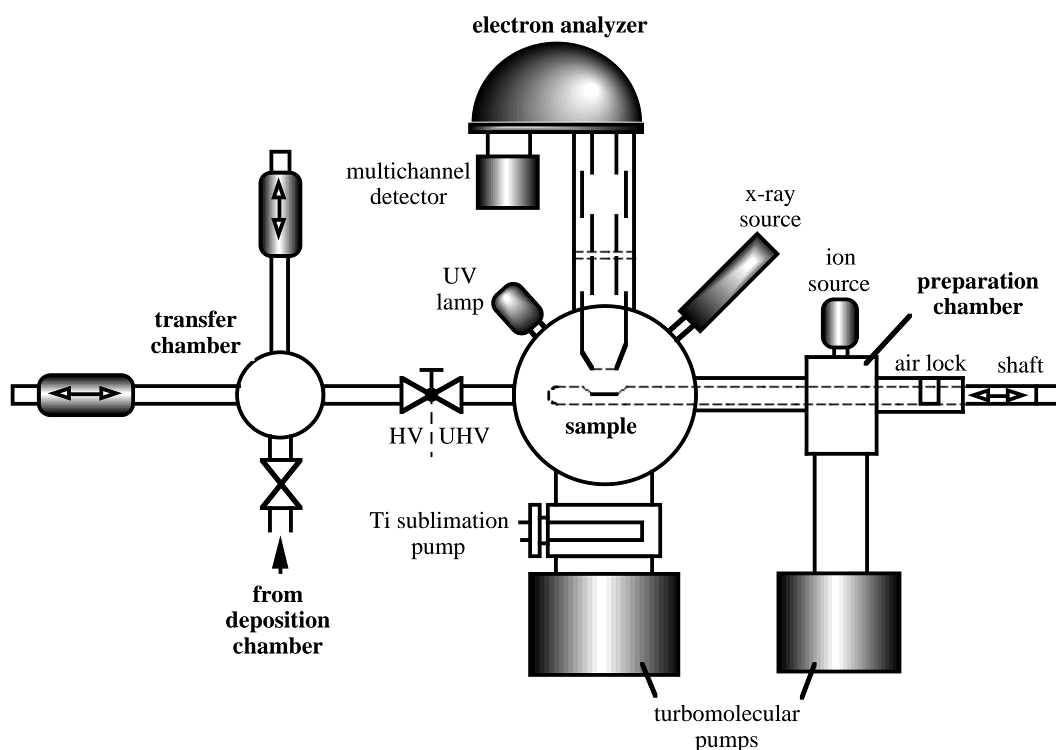

Figure 2.3: Schematic drawing of the analyzer chamber and the transfer system

The PES investigations were done in a separate UHV analyzer chamber. UHV (ultra high vacuum: $p < 10^{-8}$ mbar) is a prerequisite for PES because of the limited mean free path of the electrons in the residual gas of an HV system. Figure 2.3 shows the main components of the analyzer system, including the *in situ* transfer from the deposition chamber and an additional load lock for *ex situ* samples. The latter was reasonably employed only for qualitative analysis and comparative studies of samples with the same history.

The electron detection consisted of a spherical energy analyzer[8] and an electron multiplier. To increase the counting rate, the system was upgraded in the course of

[8] Leybold EA10

this work for multichannel detection[9] (MCD). In addition, a new data acquisition software[10] was put to use. Apart from the higher counting rate due to the MCD detection, the specifications were similar for both the old and the upgraded system.

The analyzer can be operated in the constant pass energy mode (e.g. CPE 30: constant pass energy 30 eV) or in the constant retardation ratio mode (e.g. CRR 3: constant retardation factor 3). In the CPE mode the spherical deflection unit, which acts as a narrow band pass for the electrons, is held at a constant pass energy E_{pass}. The electron energy is selected by biasing the whole deflection unit, including its entrance slit and the detector. The resolution of the analyzer is constant in this mode, because it is directly proportional to the constant pass energy. However, the sensitivity S then follows the transmission function of the analyzer, roughly a $1/E$ dependence.

$$\begin{aligned} \Delta E &= const \\ S &\approx 1/E_{\text{kin}} \qquad \text{(CPE)} \end{aligned} \tag{2.3}$$

In the retardation ratio mode the analyzer voltages are chosen to retard all the detected electrons by the same factor ($E_{\text{pass}}/E_{\text{kin}}=const.$). Combining the resolution and the transmission of the analyzer, the sensitivity is fairly constant in this mode.

$$\begin{aligned} \Delta E &\sim E_{\text{kin}} \\ S &\approx const \qquad \text{(CRR)} \quad . \end{aligned} \tag{2.4}$$

Because of historical reasons, i.e. the possibility of simple comparison with older spectra, most XPS data were taken in CPE and most UPS spectra in CRR mode.

For the XPS photon excitation, a Mg K_α X-ray source at $h\nu = 1253.6$ eV was used. The width of the Mg K_α line is about 0.7 eV. In connection with the CPE 30 mode this results in an overall FWHM of the Ag $3d_{5/2}$ core line of 0.93 eV. For the XPS electron binding energy calibration we used the Au $4f_{7/2}$ core level at 83.8 eV. A vacuum ultraviolet gas discharge lamp was the source for the UV photon excitation at $h\nu=21.2$ eV (He I) and $h\nu=40.8$ eV (He II). Within the CRR 3 mode the resolution in the vicinity of the Fermi edge is 50 meV for He I.

Data evaluation

Chemical compositions can be calculated from the XPS peak area information alone, if standard measurements for the pure elements taken under identical experimental conditions exist. This is rather seldom realizable[11] and one usually has to fall back upon tabulated values for the photoionization cross sections (e.g. [94]). If the spectra are taken in the CPE modus, the sensitivity of the analyzer is given by equation

[9] Leybold/SPECS EA10-MCD, SPECS GmbH, Berlin

[10] *SpecsLab* Data Acquisition and Processing Tool Version 1.7.12, SPECS GmbH, Berlin

[11] An exception is presented in appendix D

2.3. To calculate the concentration for homogeneous samples, the escape depth of the electrons has to be taken into account, which is fairly proportional to the square root of the kinetic energy. All in all, the intensity of a core level line for an element e is then approximately given by

$$I_e = \frac{N_e \cdot \sigma}{\sqrt{E_{\text{kin}}}} \qquad \text{(CPE)} \quad , \tag{2.5}$$

where N_e is proportional to the elemental concentration

$$c_e = \frac{N_e}{\sum\limits_e N_e} \quad . \tag{2.6}$$

As mentioned in the introduction to this section, one feature of PES is its surface sensitivity, limiting the sampling depth to a few monolayers of atoms. The sampling depth, however, strongly depends upon the kinetic energy of the electrons. A *universal curve* describes this correlation quite well [95], irrespective of the material. Indeed, this fact can be utilized to get information on the depth dependence of chemical and electronic properties. For this purpose, several core levels of the same element with different binding energy have to be evaluated (see for example appendix C).

Neither the $\mathrm{Mg\,K_\alpha}$ nor the He I/II excitations are monochromatic. There exist excitation lines at different photon energy and with lower intensity. When necessary, the XPS spectra were corrected for this according to an algorithm presented in [96].

When evaluating the peak area and/or fitting the peak form the XPS background has to be described in a meaningful way. A reasonable approach is to let the background at a certain detection channel N be proportional to the total intensity $\sum_{N'>N} I(N')$ belonging to higher kinetic energies. The corrected intensity $I^{(1)}$ can then be written as

$$I^{(1)}(N) = I^{(0)}(N) - I_0 \frac{\sum\limits_{N'>N} I^{(0)}(N')}{\sum\limits_{N'>0} I^{(0)}(N')} \quad . \tag{2.7}$$

I_0 is a free parameter adjusted to the experimental data. This iteration ansatz has proven to converge sufficiently after a few steps. The form of the background was first proposed by Shirley [97] and corresponds to a constant electron energy loss function [91] and was used for the peak fitting in the present work. Peak fitting was necessary because the oxidic and metallic parts of a core line belonging to a partly oxidized metal significantly overlap. Therefore, they had to be decomposed in order to get the relative peak areas. This was done by multiple Doniach-Šunjić [98] line peak fitting[12].

At the end of this section, a few words about the Doniach-Šunjić lineshape will be given. The asymmetric form is a result of inelastic conduction electron scattering at the core hole which produces energy losses for the excited electron. As a result,

[12] *Guifit* by C. Ellenberger (1999), software developed in our group

a tail occurs at the high binding energy side of the core line. The lineshape has the analytical form [98]

$$I(E) = \frac{\Gamma(1-\alpha)\cos[\pi\alpha/2 + (1-\alpha)\arctan(E/\gamma)]}{(E^2+\gamma^2)^{(1-\alpha)/2}} \quad , \tag{2.8}$$

which reduces to the Lorentzian $\gamma/(E^2+\gamma^2)$ for a vanishing asymmetry parameter α. Furthermore, equation 2.8 has to be convoluted with a Gaussian because of the excitation width and the instrumental resolution. The Doniach-Šunjić lineshape has proven to describe the core level of simple metals very well and is therefore applicable to aluminium. In this work it was also used to describe the Al 2s line in Al_2O_3. Strictly speaking, for $\alpha \neq 0$ the lineshape is in principle not applicable to insulators. However, it will be shown that the oxidic part of the Al 2s core level can almost perfectly be described with $\alpha \approx 0$.

One major drawback of the lineshape from equation 2.8 is that it is not integrable, i.e. it has a diverging area. The reason for this is that an infinite conduction band width was taken in account, so that the high binding energy tail extends to infinity. Mahan [99] solved this problem by adding an exponential *cut off* in the order of the band width. In the present work, the peak areas were calculated in a finite interval of ± 10 eV around the peak maximum (the Fermi energy of Al is approximately 10 eV [91]). Indeed, for the small α values occurring for aluminium the influence of this somewhat arbitrary choice is only minor. For instance, the oxidic to metallic Al 2s ratio decreases typically by 5 % when the interval is set to ± 20 eV instead of ± 10 eV.

2.2.3 Real-time specular reflectance measurement

In the course of the development of optical thin films it is of the utmost importance to follow the optics - or at least some optical features - of the film during its growth. A rigorous approach would be to observe the spectral development of both specular and diffuse reflectance. However, this objective is not that easily fulfilled, mainly because the intense plasma glow adds a high level of background noise to the signal.

Due to this difficulty, we decided to simplify the problem and detect the specular reflectance at a single wavelength[13] only, which lead us to a standard problem for a *Lock-In* detection. Details on the set-up can be found in [38] or in the diploma thesis of Ellenberger [39]. The main components are a green diode laser, a chopper, a beam splitter to detect a reference signal, a polarizer and two photo cells with *Lock-In* detection. The incident angle was 50° and the polarization angle 45° with respect to the plane of incidence (see also figure 2.1).

2.2.4 Hemispherical, diffuse and direct reflectance

For the investigations on the optical properties a dual beam optical spectrophotometer was at our disposal[14]. The spectrophotometer can be equipped with several

[13] $\lambda = 532$ nm
[14] VARIAN Cary 05

different plug-ins, an *Ulbricht* integrating sphere being the one mainly used in this work. Though the Cary 05 is in principle capable of measuring wavelengths in the range of [175 nm, 3300 nm], the PTFE coverage of the sphere restricts the application to about [300 nm, 2500 nm] [100]. Several different lamps, detectors and grids make the comparatively high wavelength range possible. A PTFE sample also served as a reference standard for the integrating sphere measurements. For the near normal hemispherical reflectance, i.e. the total reflectance in all directions, the reflected beam spots on the inner walls of the sphere. On the contrary, for determining the diffuse reflectance solely, the reflected beam was blinded out by sending it back to the entrance slit. The direct reflectance can be calculated from the difference of the hemispherical and the diffuse reflectance. Additionally, the direct reflectance was also determined separately with a direct reflectance measurement plug-in (7° incidence).

The Cary 05 integrating sphere can only detect wavelengths up to 2500 nm. The thermal emittance of several samples was therefore determined with the help of the SPF Rapperswil[15] using a rapid scan FTIR spectrophotometer[16]. The integrating sphere used in the IR range was covered by a gold film.

2.2.5 Determination of the surface morphology

The optical properties and the morphology of the AlO_x films presented in this work are inseparably correlated. A knowledge of the surface structure is therefore desirable. Two approaches were pursued, high resolution scanning electron microscopy (SEM) and atomic force microscopy (AFM).

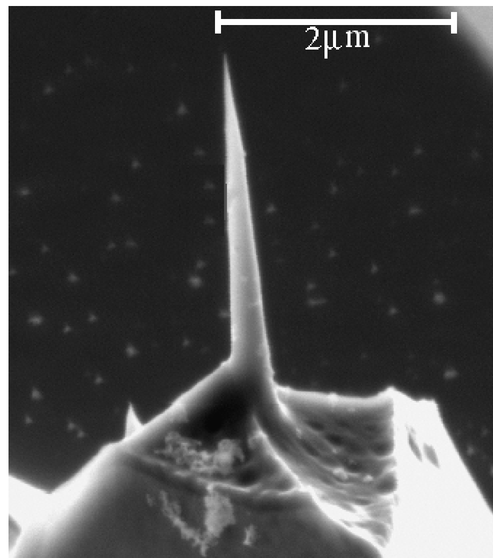

Figure 2.4: SEM picture of a high aspect ratio tip for the AFM topography measurements

[15] Special acknowledgment to the work of S. Brunold, Solarenergie Prüf- und Forschungsstelle, SPF-ITR, Rapperswil

[16] Bruker IFS66

For SEM a JEOL 6300 F at 5-10 keV was employed[17]. Because of the metallic nature of most of the films under investigation, no preliminary treatment of the samples had to be carried out. Side view SEM pictures were prepared by simply breaking previously scratched silicon wafers. For one investigation of water condensing on a surface, a Philips XL 30 ESEM (Environmental SEM) was used.

If one deals with surface microstructures, AFM is obviously a method of choice. The AFM measurements were done in non-contact mode on a commercially available apparatus[18] and special high aspect ratio tips[19] were put in use for the investigation of the rough samples[20]. The tips had a length of typically 2 μm, an aspect ratio of minimum 7:1 and a tip radius better than 10 nm. Figure 2.4 shows an SEM picture of such a tip.

2.2.6 Accelerated aging tests

For the application in solar energy harvesting devices, e.g. solar collectors, it is important not only to achieve optical performance but also to guarantee long term stability. Unfortunately, it is not possible to test it under real conditions, because one would have to wait for several decades to get reliable information. A reasonable approach to this problem is therefore *accelerated aging*, i.e. following the performance of the device under aggravated conditions and shorter time periods. For this purpose, standard test procedures were evaluated under the leadership of the International Energy Agency (IEA). These tests include high temperature and high humidity aging. Details can be found in [31, 101] and references therein. A few selected samples were subjected to these procedures at the SPF Rapperswil, which is involved in the IEA programme. In addition, separate accelerated aging tests at temperatures up to 450°C in air were undertaken[21]. Furthermore, the applicability of the premises made in [101] to the AlO_x samples is critically examined (see section 3.2.1).

[17] In exceptional coworking with M. Düggelin, D. Mathys and R. Guggenheim, SEM laboratory, Basel

[18] Topometrix TMX 1010, SPMLAB-4.0 data acquisition software

[19] High Aspect Ratio Sensors, AR5-NCH, NANOSENSORS, Wetzlar, Germany

[20] Acknowledgment to the grand work of V. Thommen and P. Reimann, AFM laboratory, IfP, Basel

[21] NABERTHERM oven, type N9/C9

Chapter 3

Results

The best results concerning solar absorbance, selectivity and wear resistance were obtained with samples consisting of two layers, a rough AlO_x film and a cover layer. The former was responsible for the high solar absorbance, whereby the latter was added for antireflection and protection. The first section of this chapter is dedicated to the properties of the AlO_x films. Section 3.2 deals with the characterization of different cover layers. At the end of this chapter a few remarks on a related absorber material (TiO_x) will be given.

3.1 The absorber layer

The AlO_x films were produced by reactive magnetron sputtering of an aluminium target in a mixed Ar/O_2 atmosphere. In the course of this chapter, the influence of various process parameters will be worked out. Indeed, the corresponding parameter space is multidimensional:

- target power P_{T}
- power type (DC, ABP at frequency f, or RF)
- target bias U_{T}
- target condition, e.g. groove depth
- target - substrate distance d_{TS}
- mass deposition rate $\dot{m}$
- deposition rate $\dot{d}$
- substrate material
- substrate bias U_{s}
- plasma bias U_{p}
- substrate temperature T_{s}
- total flow Φ
- process pressure p
- oxygen flow $\Phi_{\mathrm{O_2}}$
- oxygen content c_{O} in the coating
- film thickness d
- surface roughness, e.g. $w(d)$, $\xi(d)$, ...

- ....

Obviously, not each of these parameters is independently adjustable and there exist interdependencies.

3.1.1 Deposition rate

As already mentioned, the deposition rate of reactively sputtered oxidic materials undergoes an abrupt change at a critical value of oxygen flow. Figure 3.1 illustrates this effect for two different power levels. The QMB data were acquired in steps of 0.05 sccm and at ambient temperature. The conditioning time between each step was 5 min, after which a steady state built up for both target voltage and deposition rate. Nevertheless, a hysteresis behaviour occurred. This means that the measured deposition rate at a certain flow depended on the history of the process. The same holds for the target voltage at constant power. This memory effect can be attributed to the target and chamber wall conditions. Such a hysteresis behaviour is typical for reactive sputter deposition [84, 102]. Nevertheless, it had no major influence on this work, because most of the AlO_x films were deposited at about half of the critical flow or less, i.e. in the metallic regime of the target.

The mass deposition rate $\dot{m}(\Phi_{O_2})$ showed a typical increase for low oxygen flows. A very simple explanation can account for this behaviour. Under the assumption that a fairly constant amount of aluminium arrives at the substrate and that the oxygen uptake depends linearly on the oxygen flow (slope K), the mass deposition rate can be calculated:

$$\dot{m}(\Phi_{O_2}) = \dot{m}(0)\left(1 + \frac{m_O}{m_{Al}}\frac{c_O}{(1-c_O)}\right) \ , \ c_O = K \cdot \Phi_{O_2} \quad . \tag{3.1}$$

m_O and m_{Al} are the atomic mass of oxygen and aluminium, respectively. The dotted lines in figure 3.1 correspond to $K(80\,W) = 0.5\,sccm^{-1}$ and $K(30\,W) = 1.3\,sccm^{-1}$. From the XPS results presented in the next section and appendix A, a value of $K(80\,W) = (0.57 \pm 0.08)\,sccm^{-1}$ was obtained, which is in a fairly good agreement with this simple model. Indeed, such an effect is expected to be pronounced especially for light metal atoms like Al.

Furthermore, the amount of aluminium atoms per unit time was proportional to the target power (see figure 3.2). It is therefore understandable that the ratio $K(80\,W)/K(30\,W) \approx 0.4$ is roughly the reciprocal of the power ratio, i.e. that the oxygen uptake decreases with increasing power.

In fact, a QMB is only capable of providing the mass deposition rate $\dot{m}$. To determine the thickness increase $\dot{d}$, a step profilometer measurement was performed for two different values of Φ_{O_2}. The substrate was at ambient temperature and electrically grounded[1]. The results are $\dot{d}(0.3\,sccm) = (3.0 \pm 0.1)\,Å s^{-1}$ and $\dot{d}(0.4\,sccm) = (3.2 \pm 0.1)\,Å s^{-1}$ whereby the QMB showed up 5.6 and $5.9 \pm 0.2\,\mu g\,cm^{-2}\,min^{-1}$, respectively. The density of both ambient temperature films was therefore about $3.1 \pm 0.2\,g\,cm^{-3}$, between the values for aluminium ($2.70\,g\,cm^{-3}$) and alumina ($3.96\,g\,cm^{-3}$) [103].

[1] For these conditions the films appeared glossy and flat, not dull and rough (see section 3.1.4), so that a profilometer measurement made sense

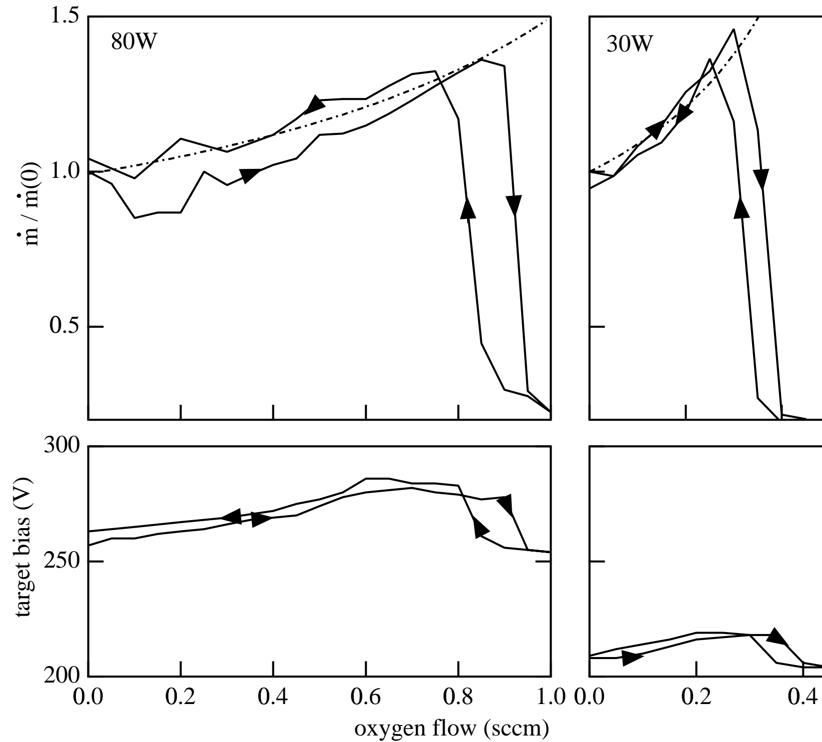

Figure 3.1: Mass deposition rate and target bias at 80 W (left) and 30 W (right) ABP power (50 kHz). The mass deposition is normalized to one at $\Phi_{O_2} = 0$. The other process parameters were: $\Phi = 40$ sccm, $T_s = 20°$C, $U_s = 0$ V, $p = 1.7 \cdot 10^{-2}$ mbar. The dotted lines represent a simple model with a linear increase in c_O (see equation 3.1).

At a critical oxygen flow the deposition rate abruptly fell to about 20 % of the value adopted for pure Al. This can be attributed to a change of the target condition from the metallic to the oxidic regime. The oxidic regime is generally characterized by a completely poisoned target, covered by an oxidic layer for which the sputtering yield is usually considerably lower than for the metallic target [84, 16]. This critical flow was roughly proportional to the target power. An analogous result was found for a pulse frequency of $f = 250$ kHz.

A comparison of the mass deposition rate for the different power supplies is given in figure 3.2. As already pointed out in section 2.1.1, the deposition rate for ABP was close to the DC value. The duty cycle at 50 kHz was 1056 ns (5.3 % of a period), whereby it was 496 ns (11.4 %) at 250 kHz. It is therefore not surprising that the deposition rate in the latter case was slightly lower. RF sputtering lead to about half the DC or ABP(50 kHz) deposition rate at the same power level. Most of the selective coatings presented throughout this work were deposited at 80 W ABP(50kHz) power, for which the deposition rate is indicated as a vertical line. In fact, we propose that the stoichiometry of the films depends mainly on the values for the deposition rate and oxygen flow. The PES measurements presented in section 3.1.2 gave additional evidence for this suggestion. It was therefore more reasonable to compare the different power supplies at equal rate rather than at equal power. Results of PES measurements on samples of equal rate follow in section 3.1.2. In figure 3.3 the $\dot{m}$ *vs.* Φ_{O_2} curves for fairly equal rates are compared. As expected,

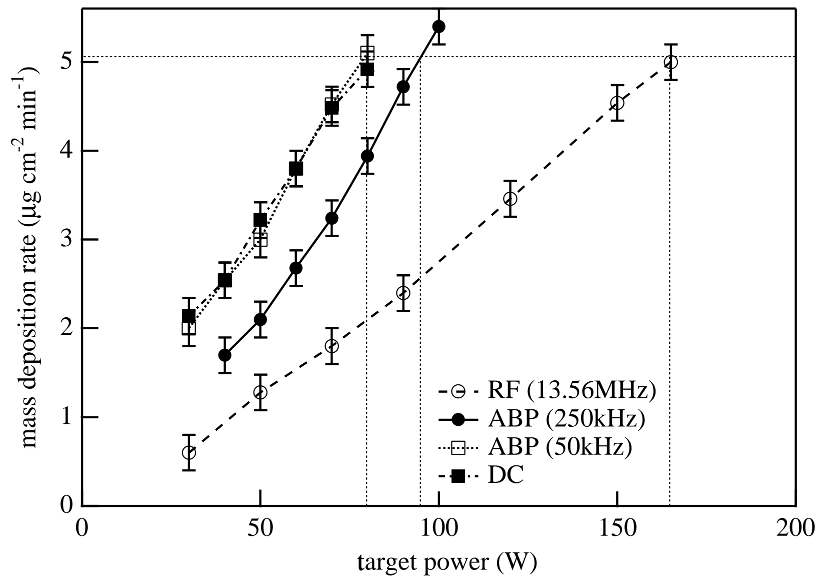

Figure 3.2: Mass deposition rate as a function of target power for different power types. The other process parameters were: $\Phi = 40\,\mathrm{sccm}$, $\Phi_{\mathrm{O_2}} = 0.2\,\mathrm{sccm}$, $T_\mathrm{s} = 20°\mathrm{C}$, $U_\mathrm{s} = 0\,\mathrm{V}$, $p = 1.7 \cdot 10^{-2}\,\mathrm{mbar}$. The vertical dotted lines indicate the power necessary to keep the deposition rate at a value similar to that of 80 W ABP(50 kHz).

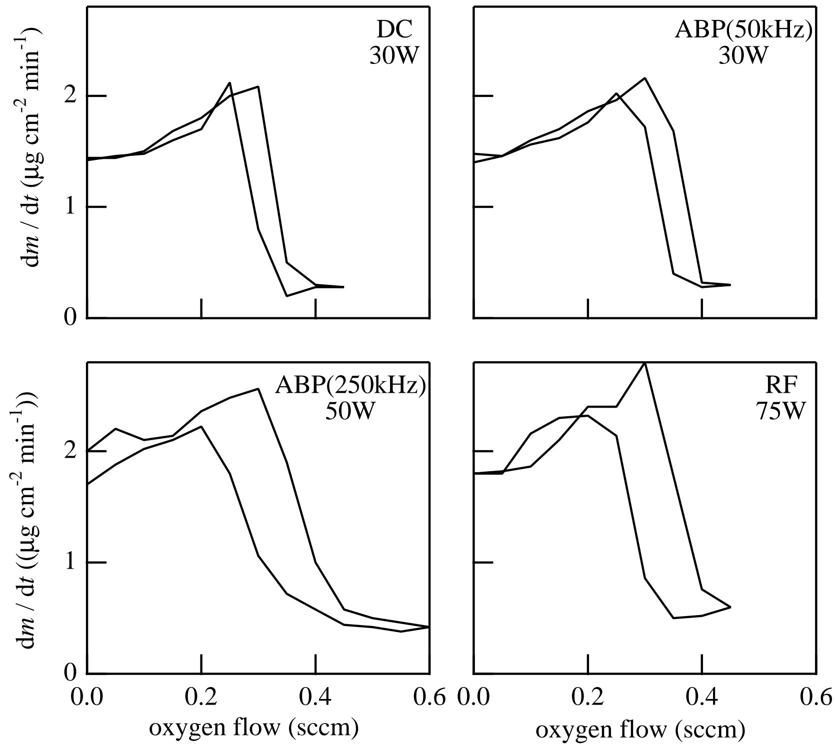

Figure 3.3: Mass deposition rate as a function of oxygen flow for different power sources. The other process parameters were: $\Phi = 40\,\mathrm{sccm}$, $T_\mathrm{s} = 20°$, $U_\mathrm{s} = 0\,\mathrm{V}$, $p = 1.7 \cdot 10^{-2}\,\mathrm{mbar}$.

the crossover took place at about the same oxygen flow. However, the hysteresis characteristics were different. For RF and ABP(250 kHz) power, the width of the hysteresis loop was broader than for DC and ABP(50 kHz). The reason for this behaviour is not clear and a variation in conditioning time should be undertaken for a more detailed investigation.

In section 3.1.5 it is shown that the substrate bias had a marked influence on the surface topography, particularly at elevated substrate temperature. Therefore, it was of interest to know if the deposition rate depends on the substrate bias U_s. For technical reasons, however, it was not possible to bias the QMB during deposition. Moreover, profilometer measurements on heated samples were not accurate – because of the pronounced micro-roughness (see section 3.1.5)! Therefore, it was not possible to determine directly the deposition rate for different substrate bias on heated samples. Nevertheless, the influence of a bias of -150 V was tested for an ambient temperature smooth sample. Indeed, the step profilometer revealed no significant influence within the error bar of about 3 %.

In contrast, the application of a plasma bias had a significant influence on the mass deposition rate, i.e. an enhancement of about 19 % from floating potential to +100 V. Simultaneously, the total power put into the process increased by fairly the same amount. The reason for this is, that an additional DC current had to be supplied to the plasma electrode to maintain the plasma bias voltage.

3.1.2 Electron spectroscopy

The electronic configuration of aluminium contains 12 atomic levels: $1s^2\,2s^2 2p^6\,3s^2 3p^1$. In the metallic phase, the 3s and 3p electrons build up a conduction band of roughly 10 eV width [91]. The 1s core level has a binding energy of 1559 eV and is therefore not accessible by a conventional X-ray source. Therefore, the only electrons available for an XPS core level analysis originate from 2s and 2p states.

Figure 3.4 shows three spectra of pure Al. The topmost was taken from a sample which was transferred *in situ* from the HV deposition chamber to the UHV analyzer. To achieve a base pressure of less than $5 \cdot 10^{-7}$ mbar the HV chamber was additionally pumped by the liquid nitrogen trap. The oxygen contamination determined from the O 1s level was about 4 at%, which is not too surprising because of the high reactivity of aluminium. As a peculiarity of aluminium there is a number of distinct intrinsic and extrinsic plasmon excitations associated with the core levels. A detailed discussion is given in [91]. In addition, satellite peaks contribute to the spectrum, easily visible at the lower binding energy end of the topmost spectrum[2]. To avoid fallacies, a satellite correction was undertaken, for which the result is shown in the middle of figure 3.4. To give evidence that this procedure was exact, an MXPS Al K_α spectrum from a clean sample prepared under UHV conditions (see appendix C) is added for comparison. Apart from the differences in relative core level intensities caused by the distinct excitation energy, the spectra are almost identical. For example, the satellite correction perfectly recreated the second plasmon feature at the low binding energy side of the Al 2p doublet, which was previously mixed up with satellites from the Al 2s core level.

[2] The binding energy representation is usually from high to low values

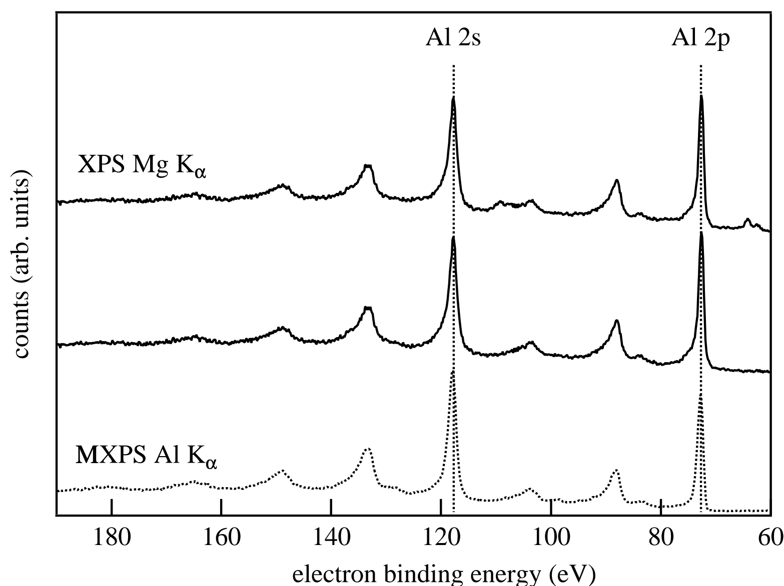

Figure 3.4: XPS spectra of pure aluminium, produced by magnetron sputtering in the HV deposition chamber. The vertical dotted lines indicate the position of the Al 2s line at 117.8 eV and the Al 2p doublet at about 72.7 eV. The topmost spectrum is without any correction, whereby the middle underwent a satellite subtraction. The spectrum of a UHV deposited pure Al film is added for comparison (monochromized Al K_α excitation, see appendix C for details).

The Al 2p excitation, though appearing as a single sharp core level peak, is actually a superposition of the two spin-orbit splitted lines, separated by 0.4 eV. Therefore, two Doniach-Šunjić lines would have been necessary for a rigorous Al 2p peak fitting and additional two for every oxidation state. For this reason, only Al 2s peak fitting was undertaken in this work. Figure 3.5 shows Al 2s peak fits for the satellite corrected XPS and the MXPS spectra from figure 3.4. Both were best fitted with an asymmetry parameter of $\alpha = 0.14 \pm 0.02$ which is compatible with literature values of about 0.12 ([91] and references therein). To reduce the number of fit parameters it was therefore reasonable to fix the asymmetry at 0.14 for all metallic Al 2s peaks.

Influence of the oxygen flow - a model experiment

A model experiment was performed to see how the oxygen flow influences the composition and chemical state of the aluminium and oxygen atoms. For this purpose XPS and UPS spectra were recorded for different oxygen flows in the process gas. To avoid contamination of the surface with residual water or carbon during deposition, the liquid nitrogen trap was used. The base pressure was about $5 \cdot 10^{-7}$ mbar.

The thickness of the layers was in the order of 40 nm. They were grown at a deposition rate of roughly 3 Ås^{-1} while the samples were electrically grounded and neither heated nor cooled during the experiment. Indeed, no significant temperature increase was measured at the thermocouple at the backside of the sample holder during the experiment. Before each of the depositions, the target was conditioned for 10 min to ensure a stable process.

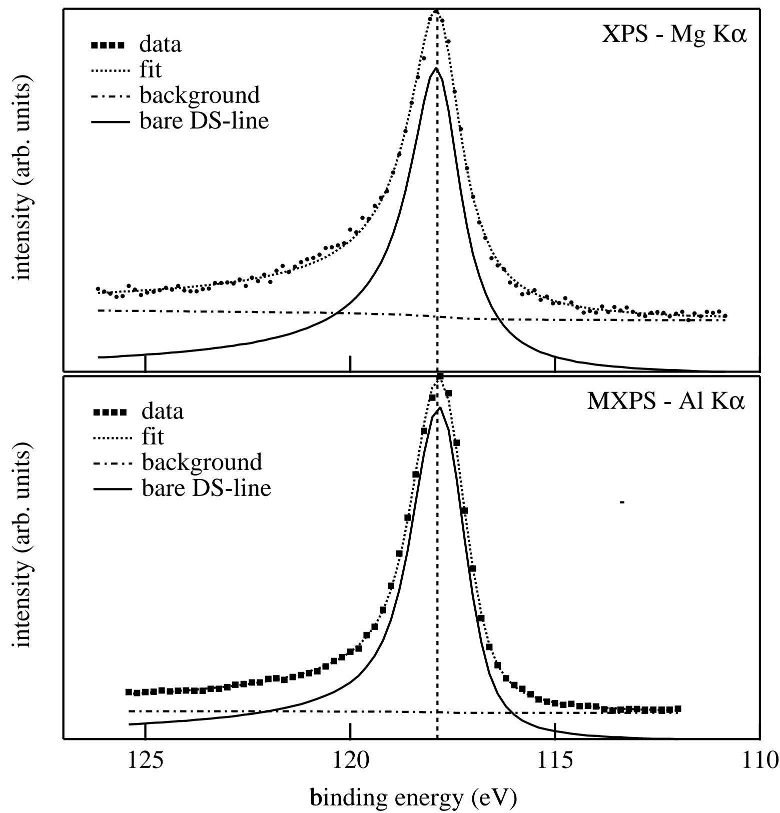

Figure 3.5: Al2s line fitting for pure aluminium. Top: XPS Mg K_α spectrum after satellite correction. The small shoulder at about 120.5 eV can be attributed to oxygen contamination. Bottom: MXPS Al K_α spectrum (taken from appendix C).

Figure 3.6 shows the evolution of the relevant core levels, i.e. Al 2s and O1s. The spectra are labelled with both the oxygen content and the oxygen flow. From bottom to top, the oxygen content determined by the core level areas increases. Thereby, the O 1s intensity is enhanced and the oxidic component of the Al 2s line gets more and more pronounced. Simultaneously, the metallic component decreases. Up to this point, there is no peculiarity associated with this behaviour. However, three effects are worth to be mentioned:

- The dotted spectrum with an oxygen flow of 0.7 sccm originates from a sample which was deposited after the target had been exposed to 1.5 sccm of oxygen flow and no target precleaning had been undertaken. The oxygen content was higher than for a corresponding sample with preliminary target cleaning. This is a clear indication for the hysteresis behaviour which was already observed in section 3.1.1.

- For a sample prepared without using the liquid nitrogen trap, the O 1s peak and the oxidic Al 2s component turned out to be more pronounced (dashed spectrum with an oxygen flow of 0.2 sccm). This was presumably due to the additional pumping of oxygen process gas by the trap. In fact, impurity effects could alternatively be minimized by prolonged pumping and aluminium

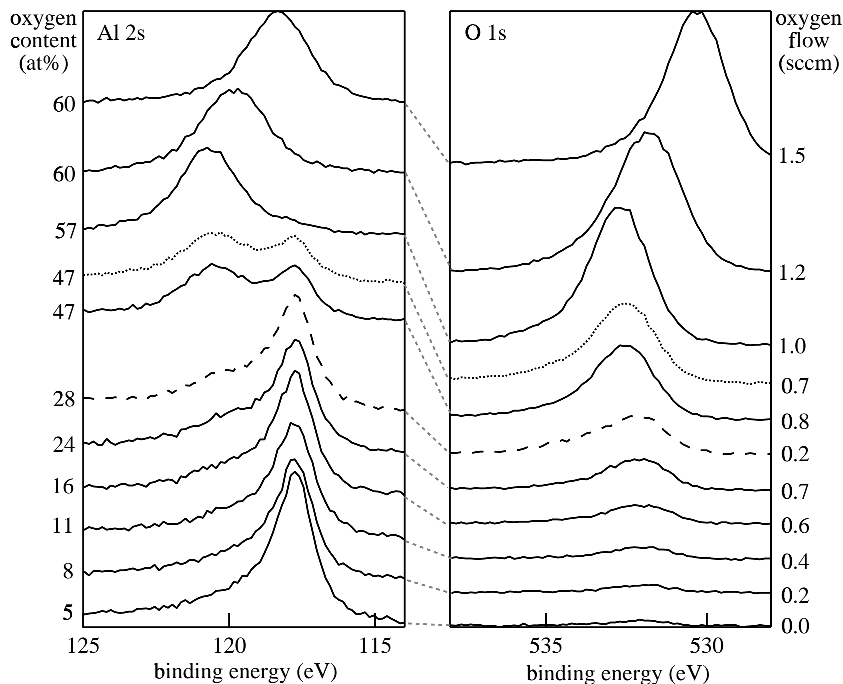

Figure 3.6: XPS Mg K_α spectra of AlO_x samples prepared with different oxygen flow. The spectra underwent a satellite correction. On the left hand side they are labelled by their oxygen content, whereby on the right the oxygen flow is given. The total flow was always 40 sccm at a process pressure of $1.0 \cdot 10^{-2}$ mbar. The dashed spectrum is taken from a sample for which the nitrogen trap was not used during deposition. The dotted spectrum represents a sample prepared without target precleaning.

target erosion. Due to the reactivity of aluminium, the Al deposition on inner chamber parts acted as a pump for oxygen, nitrogen, water, carbon etc., very similar to the functioning of Ti sublimation pumps. In this way, the base pressure for the experiments presented in the next sections was forced to be below $7 \cdot 10^{-7}$ mbar, without using the nitrogen trap.

- For high oxygen contents, i.e. with no metallic Al 2s component detectable, peak shifts occurred. This cannot be attributed to charging effects, because the shifting went to lower binding energy. Moreover, exactly the same shift was observed for all PES features, so that chemical shifts can be excluded. The only reasonable explanation is a band bending at the Schottky-barrier between Cu substrate and the insulating alumina layer. This effect was not further investigated here, because all of the selective layers were produced at distinctly lower oxygen content (< 0.5 sccm). Nevertheless, it gives a strong additional hint that pure stoichiometric alumina was formed beyond 1 sccm oxygen flow.

With the aid of the core level areas, equation 2.5 and the cross sections from [94] the chemical composition of the samples was determined (dotted line in figure 3.7). The oxygen concentration obtained in this way ends up at about 50 at% for the highest oxygen flows. However, from the peak shift and the fact that no metallic

component was detected, it is most presumable that at 1.5 sccm pure alumina was formed, i.e. 60 at% oxygen. This fact can be employed to recalculate the chemical composition of all two-component AlO_x samples in a more direct way (solid circles). The difference can be put down to errors for the calculated cross sections and the assumption of a universal escape depth function. In the following, all concentrations for AlO_x were calculated using this more direct method.

The behaviour of the oxygen content with increasing flow is different to what was found in appendix A (open triangles in figure 3.7[3]) and by Stauder *et al.* [18]. They found that the oxygen content increased almost linearly for low values of oxygen flow. We believe that this difference is due to the use of the cooling trap, which pumps not only impurity gases but also process oxygen. The solid triangle which represents a preparation without cooling trap (but with comparably low base pressure) gives additional evidence for this suggestion. When the target was covered by pure alumina, the film composition was determined by the target composition rather than the oxygen amount in the process gas. The more step-like behaviour for the present experiment can be qualitatively explained in this way.

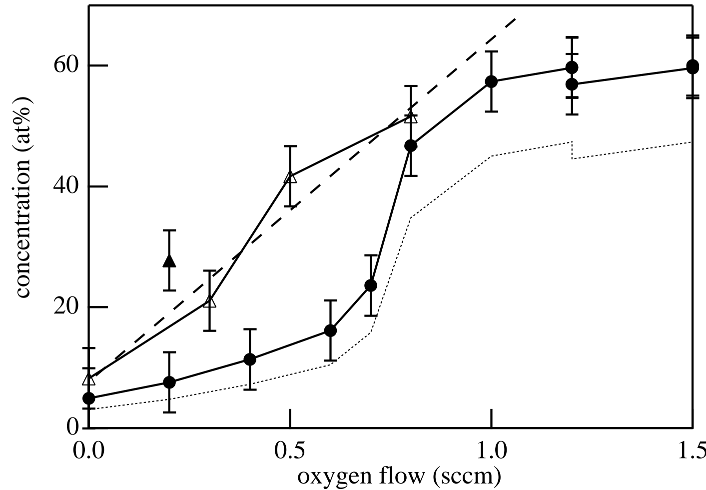

Figure 3.7: Concentrations from the XPS core level areas. Dotted line: Oxygen content determined from equation 2.5 with the tabulated cross sections from [94]. Solid circles: Oxygen content under the assumption that at 1.5 sccm O_2 pure alumina was formed. Solid triangle: Sample prepared without cooling trap. Open triangles: Comparison to the recalculated results from appendix A. Dashed line: Linear regression with $K = 0.57 \pm 0.08\,\mathrm{sccm}^{-1}$ (compare to section 3.1.1)

The oxidic component of the Al 2s serves as an additional oxygen monitor. The areas of the oxidic and metallic components were determined by multiple peak fitting as described in section 2.2.2. For two different oxygen contents, the results of such fitting procedures are shown in figure 3.8. As already mentioned, the asymmetry was fixed at $\gamma = 0.14$ for the metallic component and $\gamma = 0$ for the oxidic one. Other values for γ did not give significant better fitting curves. Moreover, fits with more than two components did not lead to better results. So one can conclude

[3] The concentrations were recalculated using the more direct evaluation. This method was only applicable for the AlO_x system and not for the $AlCu_xO_y$ system

from the XPS spectra that these films were built up of phase separated oxidic and metallic material. However, the position of the oxidic component changed gradually from about 120.0 eV at 0.2 sccm to 120.7 eV at 1.0 sccm (see e.g. figure 3.8). This was accompanied by a comparable shift of the O 1s level. An analogous behaviour was observed for the ambient temperature data in appendix A. Even though it seems that the material consisted of two distinct phases, it is therefore evident that the chemical surrounding of the atoms belonging to oxidic domains changed with increasing oxygen content. The most probable explanation is a decrease of Al-Al bonds in the oxidic domains and/or an increase in size of these domains.

The FWHM of the oxidic portion of the Al 2s line is typically about 1 eV broader than the metallic one. This effect can be attributed to different bonding types in the disordered oxide [104].

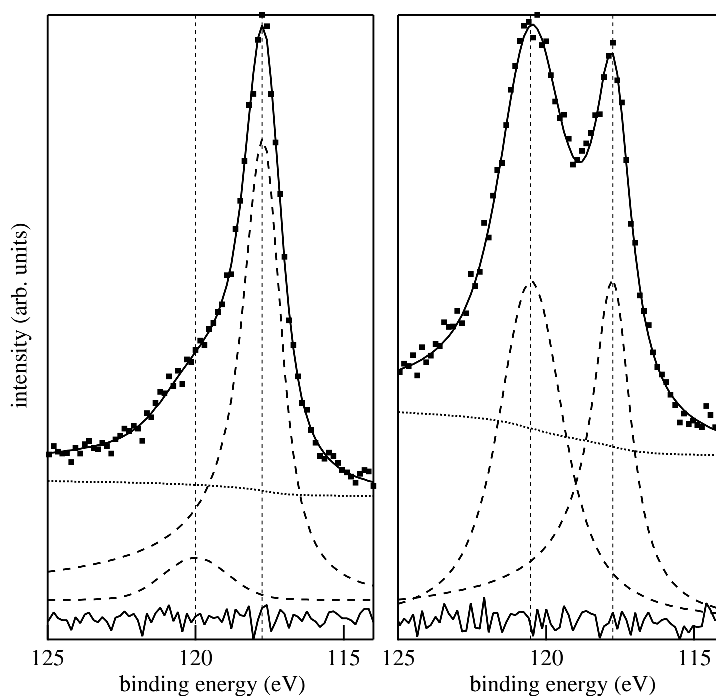

Figure 3.8: XPS peak fitting for two selected spectra from figure 3.6. The dotted line corresponds to the background according to equation 2.7 and the dashed spectra represent the two bare core lines. The difference between original data and the fit is depicted as a solid line in the lower part of the graph.

The peak fitting results in oxygen contents compatible with the values obtained from the total peak areas (figure 3.9). Indeed, using solely the components of the Al 2s line has the advantage that surface effects are less important because the influence from electrons with different kinetic energy is negligible.

The UPS spectra in figure 3.10 clearly show a Fermi edge up to about 0.8 sccm oxygen flow, which is additional evidence for the metallic nature of the samples or at least parts of them. The relative height of the Fermi edge decreases and the valence band maximum shifts to slightly higher binding energy values, indicating a gradual change of the interatomic bonding.

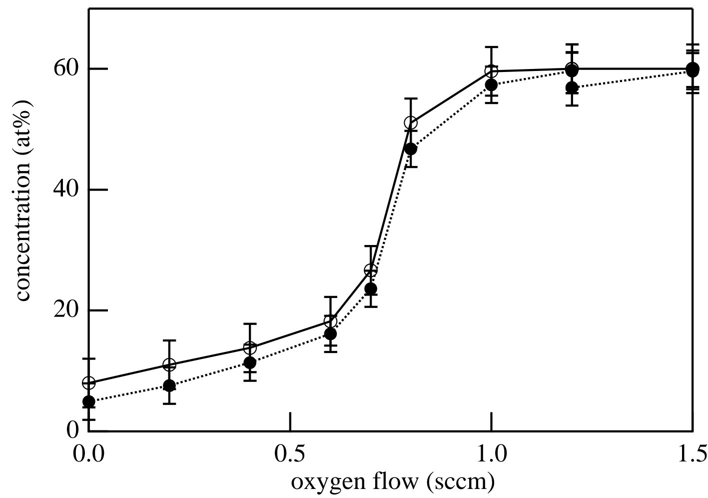

Figure 3.9: Oxygen content determined from the O 1s and Al 2s total core level areas (solid circles) and from the Al 2s peak fitting (open circles). Both evaluations rely on the assumption that at 1.5 sccm O_2 pure alumina was formed.

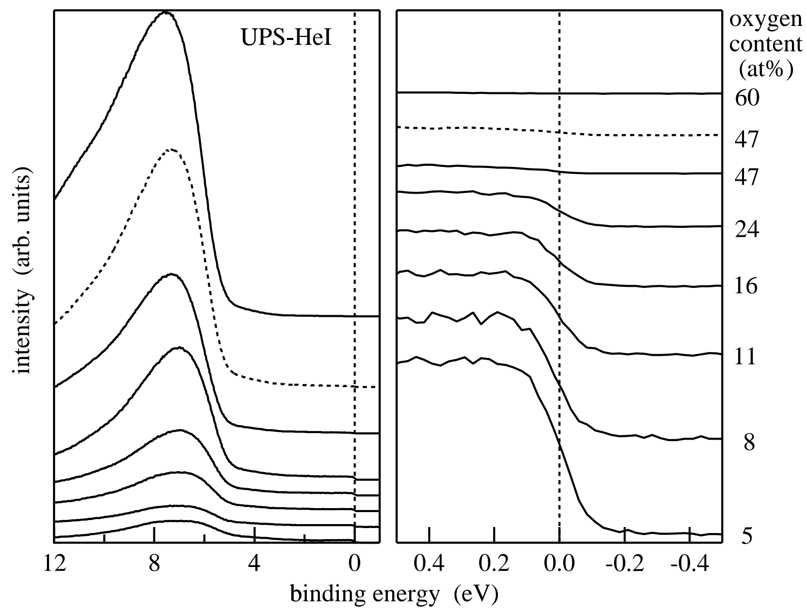

Figure 3.10: UPS HeI spectra for different oxygen content. They are labelled by the oxygen concentration. On the left hand side the spectra are shown as they were measured. On the right only a 1 eV range around the Fermi edge is depicted, whereby the spectra were normalized to one at maximum intensity. The dashed spectrum corresponds to the sample for which no target precleaning was undertaken.

Besides the differences with experiments using no cooling trap (e.g. appendix A), this model experiment clearly showed the interdependencies between oxygen content, metallic peak contributions and UPS spectra. The same evaluation methods can

therefore be used in the next paragraphs, where the influence of selected process parameters is investigated.

Power level and power source type

In this paragraph it is outlined how the power level influences the stoichiometry of the films. Furthermore, the effect of different excitation sources is examined.

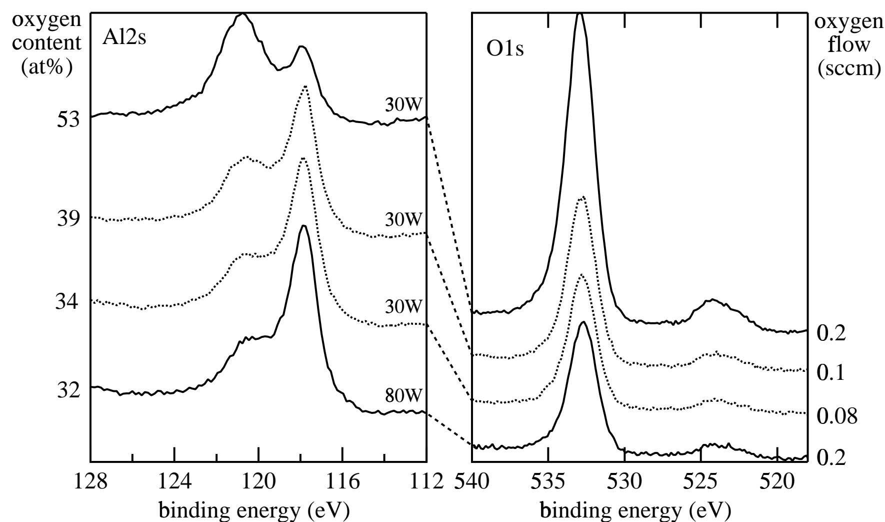

Figure 3.11: XPS spectra for 30 W and 80 W ABP power. The top and bottom spectra represent samples deposited at the same oxygen flow. The dotted spectra belong to 30 W samples for which the oxygen flow was corrected to achieve the same stoichiometry as for the 80 W sample. The other process parameters were: $\Phi = 40$ sccm, $T_s = 290°$C, $U_s = -150$ V, $p = 1.7 \cdot 10^{-2}$ mbar.

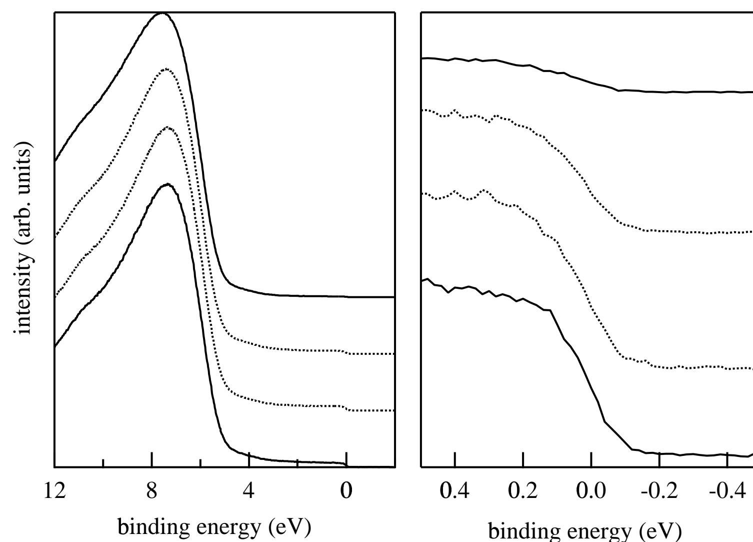

Figure 3.12: UPS HeI spectra corresponding to the XPS spectra of figure 3.11.

To test the influence of the power level at otherwise same process conditions, XPS (figure 3.11) and UPS (figure 3.12) investigations were undertaken. It turned out that the oxygen content at a power of 30 W was considerably higher than the one at 80 W. This is clearly visible from the top and bottom spectra. It was therefore interesting to test how the oxygen flow had to be changed to achieve equivalent stoichiometry. For 30 W it was necessary to reduce the flow to about 2/5 of the value for 80 W. This is similar to the power ratio of 3/8. It means that the same stoichiometry was obtained at the same fraction of the deposition rate crossover (section 3.1.1, figure 3.1). This is further evidence for the suggestion that the main parameters determining the oxygen content in the films are the deposition rate and the oxygen flow.

From a practical point of view the influence of the power supply type is a valuable information. To examine this, it is reasonable to compare XPS and UPS spectra from samples at the same deposition rate and flow rather than the same power and flow. The necessary power levels were deduced from figure 3.2: 165 W RF, 95 W ABP(250 kHz) and 80 W DC correspond to fairly the same deposition rate as 80 W ABP(50 kHz). Indeed, the oxygen content determined for films prepared at 0.2 sccm O_2 was 34, 34, 31 and 32 at% respectively, identical within the error range. Moreover, both the XPS and the UPS spectra coincide almost perfectly. As an example, the UPS HeII spectra are depicted in figure 3.13. In fact, the results obtained from either HeI or HeII spectra were identical throughout this work.

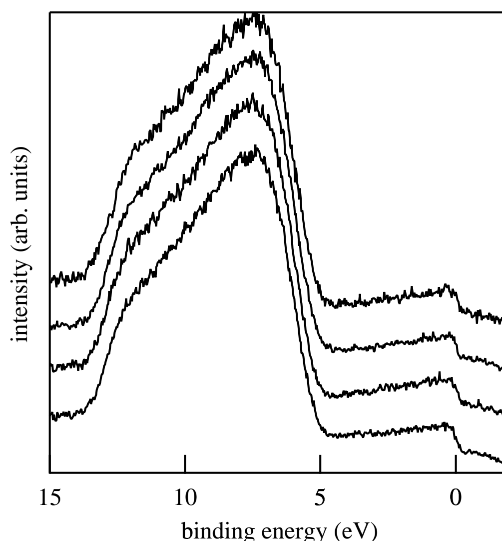

Figure 3.13: UPS HeII results for samples prepared with various power supply type. From top to bottom 165 W RF, 95 W ABP(250 kHz), 80 W ABP(50 kHz) and 80 W DC. The deposition rate was fairly identical at $5.1\pm0.2\,\mu g\,cm^{-2}\,min^{-1}$

Process pressure

The effect of a process pressure change was best studied with RF power because the accessible pressure range within stable process conditions was higher. To take the results of the last paragraph in account, the mass deposition rate was kept constant

during this investigation. Because the deposition rate increased with decreasing process pressure, the power level had to be readjusted. Table 3.1 summarizes the results.

p (mbar)	P (W)	Φ_{O_2} (sccm)	c_O (at%)	$\dot{m}$ (μg cm^{-2} min^{-1})
$1.7 \cdot 10^{-2}$	165	0.3	34	5.6
$2.3 \cdot 10^{-3}$	135	0.3	29	5.6
$2.3 \cdot 10^{-3}$	120	0.4	34	5.6

Table 3.1: Process parameters of samples prepared at different process pressure but constant mass deposition rate. The other process parameters were: $\Phi = 40\,\text{sccm}$, $T_s = 290°\text{C}$, $U_s = -150\,\text{V}$.

It turned out that the oxygen flow had to be slightly increased to obtain the same stoichiometry at lower pressure. However, the significance of this fact is not clear. Nevertheless, such a behaviour would not be too surprising because the mean collision rate in the gas phase and on the surface of the growing film increases with pressure.

Substrate temperature and bias, plasma bias

T_s (°C)	Φ_{O_2} (sccm)	U_s (V)	c_O (at%)
20	0.2	0	26
290	0.2	0	27
20	0.3	0	34
290	0.3	0	36
20	0.3	-150	31
150	0.3	-150	36
290	0.3	-150	32
290	0.3	-100	28
290	0.3	-50	34
290	0.3	0	32

Table 3.2: Process parameters of samples prepared at different substrate temperature and bias. The other process parameters were: $P = 80\,\text{W}$ ABP(50 kHz), $\Phi = 40\,\text{sccm}$, $p = 1.7 \cdot 10^{-2}$mbar.

As will be shown in section 3.1.5 the substrate temperature as well as the substrate bias are parameters which determined the growth properties of the films considerably. It is therefore worth to identify if there is a major influence of these parameter on the stoichiometry. In table 3.2 the data for several samples are cumulated. Though significant scattering of the oxygen content data occurred, there is no systematic dependence discernible. This result is in agreement with the observations in appendix A. It has to be noted that those data were collected in the course of an independent experimental series.

Concerning the use of the plasma bias set-up instead of substrate biasing, no *in situ*

XPS measurements were undertaken, due to technical problems. Nevertheless, *ex situ* comparative depth profiling revealed no significant difference between a sample prepared with +100 V and one with floating plasma potential at 0.3 sccm O_2. The sensitivity of this *ex situ* method was tested by a comparison with a sample prepared at 0.2 sccm O_2 and floating plasma bias. The difference was significant, so that the sensitivity of the *ex situ* ESCA method can be assumed to be not far below the one of *in situ* measurements. However, a quantitative determination of stoichiometries was obviously not possible in this way, because the depth profiling induces structural and chemical changes due to ion bombardment.

Sputtering gas

Gas	c_O (at%)	$\dot{m}$ (μg cm^{-2} min^{-1})
Ar	47	3.1
Ne	37	5.4

Table 3.3: Process parameters of samples prepared with either Ar or Ne inert sputtering gas. The other process parameters were: $P = 80$ W ABP(50 kHz), $\Phi = 40$ sccm, $\Phi_{O_2} = 0.2$ sccm, $T_s = 20°$C, $U_s = 0$ V.

The use of different inert process gases is again interesting from a practical point of view, i.e. a high deposition rate at a low power level is aspired. As one can see from table 3.3 the deposition rate was considerably enhanced when Neon was used instead of Argon. This is reasonable, because the relative atomic mass difference between the sputtering ions and the sputtered metal atoms is lower. Simultaneously, the oxygen content decreased which can again be attributed to the higher deposition rate.

Target-substrate distance and target condition

d_{TS} (cm)	Φ_{O_2} (sccm)	P (W)	c_O (at%)	$\dot{m}$ (μg cm^{-2} min^{-1})	target groove depth
6	0.3	80	–	3.3	low
4.5	0.3	80	45	6.5	medium
6	0.3	80	48	4.5	medium
7.5	0.3	80	52	3.8	medium
4.5	0.4	65	44	5.2	high
6	0.4	80	44	5.2	high

Table 3.4: Process parameters of samples prepared with various target-substrate distances. The different sections of the table belong to three distinct target conditions. The other process parameters were: ABP(50 kHz), $\Phi = 40$ sccm, $T_s = 290°$C, $U_s = -150$ V.

From the results of the last few sections one can conclude that the most important parameters determining the stoichiometry are the oxygen partial pressure and the

deposition rate. Another test for checking this suggestion is a variation in the target-substrate distance. Table 3.4 contains XPS concentrations from two independent experimental series. Within the first, the distance was varied and the power was held constant. As expected, the deposition rate decreased with enhanced distance and simultaneously the oxygen concentration increased. The second experiment showed that it was possible to correct the stoichiometry by lowering the target power when decreasing the distance, i.e. equalizing the deposition rate.

In the course of this work the deposition rate underwent long-term changes. In the beginning, these changes were not understood and seemed to be somehow mysterious. In fact, they are correlated to the target condition, i.e. the depth of the grooved ring. For example, a fresh-installed Al target of 1 cm thickness showed a sputtering rate of about $3\,\mu g\,cm^{-2}\,min^{-1}$ pure aluminium, whereas this value altered to $5\,\mu g\,cm^{-2}\,min^{-1}$ as the groove depth came up to 7 mm. During a single experimental series this effect had no major influence. Nevertheless, it made a direct comparison of different series more puzzling.

3.1.3 Real time process control

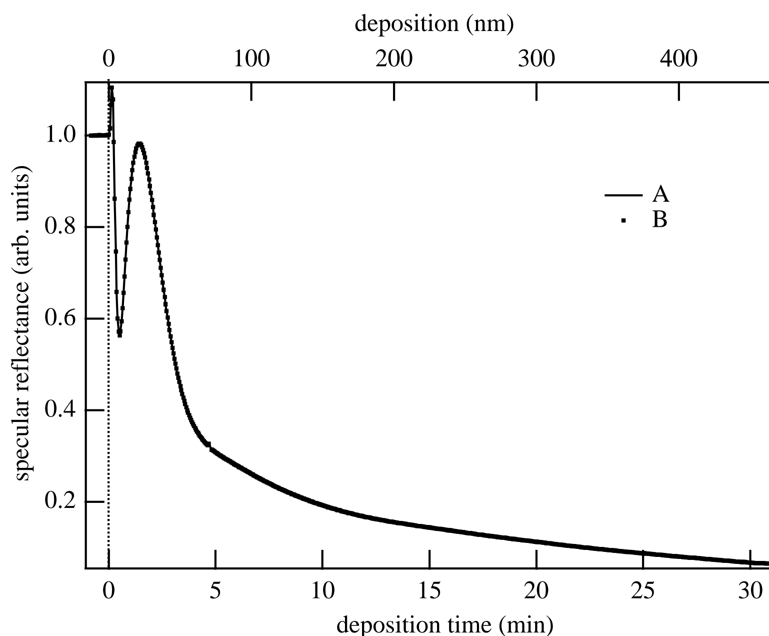

Figure 3.14: Specular reflectance at 532 nm during the growth of AlO_x on Cu. The samples A and B were deposited under identical process conditions.

Appendix A demonstrates the practical feasibility of the *real time* reflectometry for process control. This section shall enlighten particularly some of the more fundamental questions.

Figure 3.14 shows the specular reflectance during the growth of two rough AlO_x samples on mechanically polished Cu. The two samples were prepared under identical conditions and the reflectance curves perfectly overlap. Apart from the small peak at the very beginning of the deposition, the behaviour is understood at least in a qualitative way: The minimum-maximum feature in the first four minutes corre-

sponds to an interference of the beams reflected from the front and backside of the layer. Such a smooth-layer interpretation must fail for incessant deposition because considerable roughness occurred (see section 3.1.5). More and more of the incident light was therefore diffusely reflected and absorbed, which lead to the pronounced decrease of the specular reflected beam intensity for higher thickness. The small peak in the very beginning of deposition is not understood yet and may be attributed to some interface reaction (see appendices A and C) and/or surface oxidation.

The initial reflectance obviously depends on the substrate material and its roughness. For example, reflectance curves for identically prepared samples on non-polished aluminium showed significant variations. This is attributed to the distinct roughness of the Al sheets. Step-profilometer scans revealed that the roughness of the Al substrates was in the order of a few hundreds of nanometres and therefore about five times higher than for the Cu substrates. Moreover, due to the rolling during sheet production, the roughness showed also a preferential orientation. As a consequence, already the uncovered Al substrates reflected in a diffuse way, so that it was impossible to set up a reproducible starting point. Nevertheless, these reflectance curves bear valuable qualitative information. On the other hand, the bare Cu, Si and AF45[4] substrates produced a specular reflected laser spot. For these substrate materials the reflectance curves were reproducible (figure 3.14).

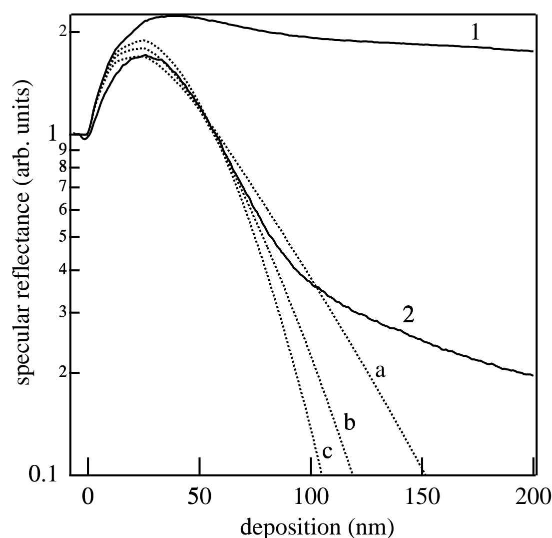

Figure 3.15: Specular reflectance during the growth of AlO_x on Si. **1**: Sample prepared at 20°C and 0V bias, serving as R_0. **2**: Sample prepared at 290°C and -150 V substrate bias. **a**: Model calculation with $\beta = 0.7, b = 1.3$. **b**: $\beta = 0.9, b = 0.6$. **c**: $\beta = 1.1, b = 0.3$.

To investigate the specular reflectance more quantitatively, polished Si substrates were used (figure 3.15). The reflectance showed a pronounced increase, a maximum and finally the typical decrease observed for any substrate material. For comparison, the reflectance of a similar sample, but deposited on a room temperature substrate and without any bias, was added. This sample had a glossy shallow brown metallic appearance. Nevertheless, according to the ESCA results of section 3.1.2, the chemistry was equivalent to that of the rough sample. It is therefore reasonable to

[4] Alkali free borosilicate glass

assume that the refractive index was similar.

According to Bennett and Porteus [105] the specular reflectance of a rough surface consisting of a medium with refractive index $\tilde{n}$ is given by:

$$R = R_0 \, e^{-\left(\frac{4\pi \, \cos\theta \, w(t)}{\lambda}\right)^2} \;, \; w(t) \ll \lambda \quad , \tag{3.2}$$

where R_0 is the Fresnel reflection coefficient and $w(t)$ the RMS deviation from a flat surface, i.e. the interface width. For higher values of $w(t)/\lambda$ further corrections have to be taken into account, the next order proportional to $w(t)^4 \sim t^{4\beta}$.

A similar first order perturbation *Debye-Waller* factor ($e^{-const \cdot w^2}$) was also found to describe the specular part of a diffraction pattern from a rough interface in the *continuous-surface* limit[5] $k_\perp c \ll \pi$ for any kind of light or particle scattering (see e.g. [54] and references therein):

$$S(\vec{k}_\parallel, k_\perp, t) \sim (2\pi)^2 \, e^{-[k_\perp c \, w(t)]^2} \, \delta(\vec{k}_{||}) + S_{diff}(\vec{k}_\parallel, k_\perp, t), \; k_\perp c \ll \pi \; , \tag{3.3}$$

where $\vec{k}_\parallel$ and $k_\perp$ are the in-plane and perpendicular components of the scattering vector. Here, the RMS roughness $w(t)$ is measured in units of the lattice constant c. In the case of light scattering the condition $k_\perp c \ll \pi$ is always met. If the diffuse part $S_{diff}(\vec{k}_\parallel, k_\perp, t)$ does not contribute significantly to the specular reflected beam (which is in fact valid in the *small-perturbation* or *smooth-surface* limit $w(t) \ll \lambda$) the reflectance is mainly determined by the exponential decrease.

All perturbation theories rely on the *smooth-surface* limit[6], which is in our case only applicable for short deposition times, because the lateral and vertical correlation lengths increase with nominal thickness (see section 3.1.5). Nevertheless, a still reasonable matching of equation 3.2 and the experimental curve was achieved for the first nominal 100 nm of deposition (figure 3.15). In these early stages the interface width was below 20 nm. This means $w(t)/\lambda < 0.04$, a typical limit for the smooth-surface model to be valid [106]. The Fresnel reflection coefficient R_0 was thereby taken from the room temperature sample without any bias. For the growth exponent, a value of 0.9 ± 0.2 fits best. Indeed, the theoretical reflectance evolution depends strongly on this parameter β. The number b is given by $w(t) = b \cdot d^\beta$ where $d \sim t$ is the nominal thickness of the film in nanometres, i.e. without roughness.

Obviously, it is also possible to model n and k of the material so to establish a better fitting to the experimental result, as shown in figure 3.16. The difference between the model (a) and the measurement (1) for the smooth film is presumably due to a non-zero roughness even for this sample. In fact, a very good fit (b) to the experimental values (2) for the rough film could be achieved with this model. The matching range was even increased by taking into account the next order correction (c). The roughness exponent is again $\beta = 0.9 \pm 0.2$ for this model. In addition, the values $n = 1.2$ and $k = 2.5$ are reasonable. For a comprehensive overview on the optical properties of Al and slightly oxidized Al the reader is referred to [12] and [13].

[5] In contrast to X-ray diffraction at Bragg planes, for instance - to be distinguished from the *smooth-surface* limit.

[6] In scattering theory, it is known as the *Born* approximation.

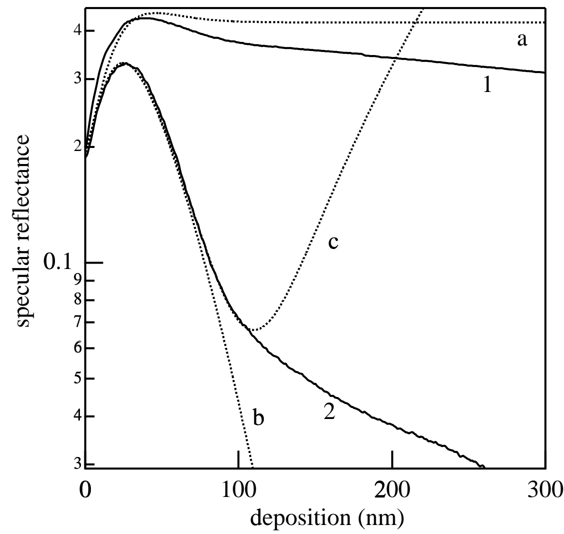

Figure 3.16: Specular reflectance during the growth of AlO_x on Si. The 'deposition time' can be either measured in minutes or nanometres, i.e. units of nominal thickness without roughness. **1**: Sample prepared at 20°C and 0V bias. **2**: Sample prepared at 290°C and -150 V substrate bias. **a**: Theoretical curve for a smooth layer of material with $\dot{d} = 2.5\text{Å}\text{s}^{-1}$, $n = 1.2$, $k = 2.5$. **b**: small perturbation limit. **c**: taking into account the second order correction.

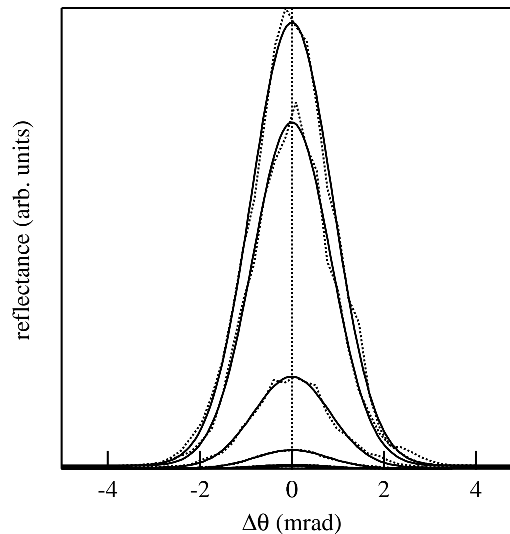

Figure 3.17: Angle dependence of the specular reflected peak for a polished Si wafer (topmost curve) and different sample thickness of AlO_x on glass (*ex situ*, from top to bottom: 5 min, 10 min, 20 min and 30 min deposition). Gaussians fit very well to the data, whereby the FWHM is constant within the error bars: 2.3±0.1 mrad.

To get information on the angular dependence of the specular reflected beam, a 10 micron slit was mounted in front of the photo diode and the position of the whole detection unit was tangentially moved in steps of 0.04 mm which corresponds to an angular resolution of 0.23 mrad (figure 3.17). These measurements were performed with samples of different thickness on AF45 and additionally with a clean polished Si

wafer. The chamber was vented to air for these investigations, i.e. *ex situ* conditions. The peak maximum followed a decrease with film thickness compatible to the *in situ* result from figure 3.15. Additionally, no significant peak broadening was observed, which is in agreement with the prediction of equation 3.3 that the specular reflected beam decreases in favour of the diffusely reflected light but does not change its form.

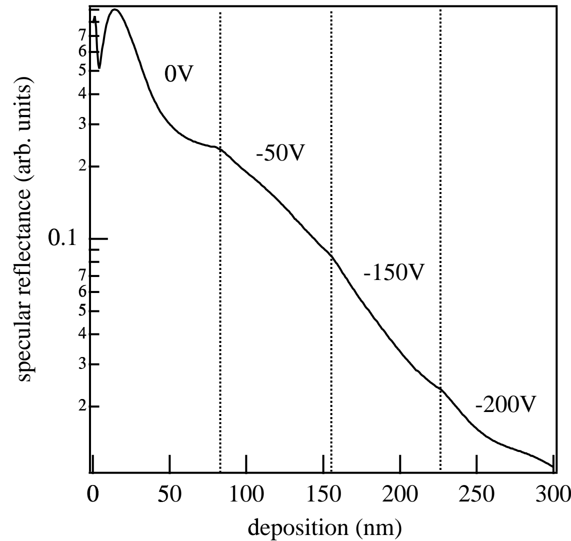

Figure 3.18: Variation in substrate bias during the growth of of AlO_x on Cu.

The *real-time* reflectometry was also very useful to study the influence of certain process parameters. As an example, figure 3.18 depicts an experiment, where the substrate bias was altered during the deposition. With every increase of substrate bias there was associated a pronounced downwards bending of the reflectance curve, which indicated a considerable enhancement of the roughening.

3.1.4 Optical properties

This section deals with the more principle questions concerning single rough AlO_x layers and the reflection properties of the substrate materials. A qualitative discussion of representative hemispherical reflectance spectra, which in fact determine the selective properties, is presented in appendix A.

In section 3.1.3 the distinct behaviour of the *real time* specular reflectance for Cu and Al substrates was discussed in terms of the different roughness of these substrates. This can be put on solid ground now, employing diffuse reflectance measurements (figure 3.19). The difference between hemispherical and diffuse reflectance was much more pronounced for the polished Cu substrates than for the non-polished Al. This is evidence for a distinct roughness. The Al substrates reflected diffusely over a wide range of wavelengths while the Cu substrates showed this behaviour only for small wavelengths.

Though it turned out that the roughness of the substrate material had no major influence on the growth properties of the rough AlO_x films, it was more rigorous to use flat substrates, e.g. glass or polished Si, for fundamental investigations on

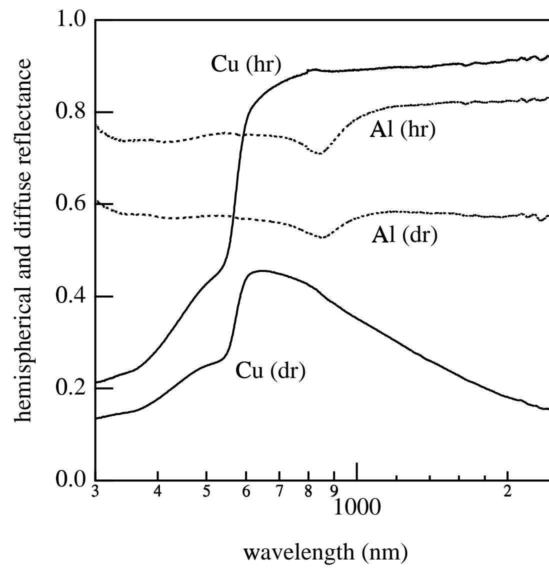

Figure 3.19: Hemispherical (hr) and diffuse (dr) reflectance for the metallic substrate sheets

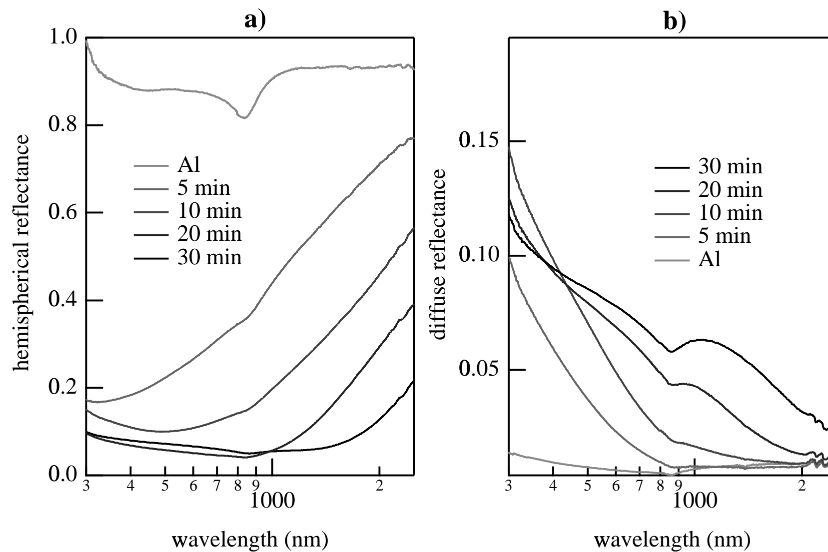

Figure 3.20: Hemispherical (a) and diffuse (b) reflectance of AlO_x samples on AF45 glass for different deposition times. The spectrum denoted 'Al' belongs to an aluminium mirror on AF45 prepared at room temperature without oxygen and bias. The process parameters: $P = 80$ W ABP(50 kHz), $\dot{d} = 3.6$ Ås^{-1}, $\Phi = 40$ sccm, $\Phi_{O_2} = 0.3$ sccm, $T_s = 290°$C, $U_s = -150$ V, $p = 1.7 \cdot 10^{-2}$ mbar.

the growth properties. Figure 3.20 depicts the hemispherical and diffuse reflectance of films with various deposition times on AF45 glass. The most striking feature is that the crossover from absorbing to reflecting behaviour occurred at a gradually higher wavelength the thicker the films were (figure 3.20 a). In section 3.1.5 it is shown that this fact is intimately connected to the roughness evolution of the films: The correlation lengths w and ξ of the surface topography increase with thickness. It is therefore also not surprising that the diffuse reflectance extended

to higher wavelengths as the deposition time increased (figure 3.20 b). Intriguingly, the reflectance minimum at about 900 nm, typical for pure Al, was maintained. This minimum originates from a singularity in the JDOS of aluminium at about 1.6 eV [107], attributed to the so called *parallel band effect*. Similar results were found for samples on polished silicon wafers.

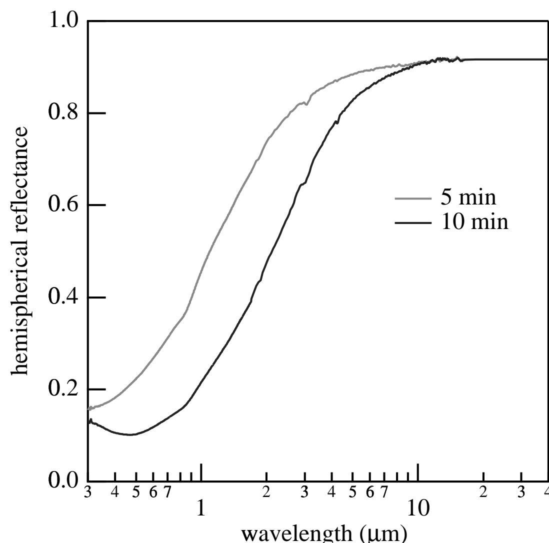

Figure 3.21: VIS-IR hemispherical reflectance for two AlO_x/AF45 samples.

For two of these samples broadband hemispherical reflectance data are at our disposal (figure 3.21). In the far infrared region, even the sample with the lowest nominal thickness of 75 nm showed hemispherical reflectance values near to that of the pure Al mirror. This fact is important, because no IR mirror substrate material was used, i.e. the IR reflecting property originates from the film itself and not from any IR mirror substrate.

The specular reflectance at near normal (n.n.) incidence is simply the difference between the hemispherical and the diffuse reflectance. The result is drawn in figure 3.22 a). A comparison to a simple independent specular reflectance measurement at 7° incidence shows an almost perfect matching (figure 3.22 b).

At a fixed wavelength the specular reflectance decreased more or less exponentially as a function of thickness (not shown here), compatible to the *in situ* reflectometry results. However, the Δd steps are too wide for a rigorous evaluation using equations (3.2) or (3.3). A theoretical description of the hemispherical reflectance using a standard perturbation technique was not further pursued here, because they hold only for a too low $w(t)/\lambda$ ratio (see section 3.1.3). Especially, they are not applicable to the crossover region – on fundamental grounds. Moreover, a rigorous theoretical description would require the knowledge of the refractive index $\tilde{n}(\lambda)$.

Several series of deposition and measurement were undertaken to tune the growth behaviour within the multi-dimensional parameter space. A few examples are shown in figure 3.23 a)-c), varying substrate temperature and bias. The oxygen content was also altered within the error bars of the ESCA results to ensure that the oxygen concentration was not uniquely responsible for the changes in optical properties.

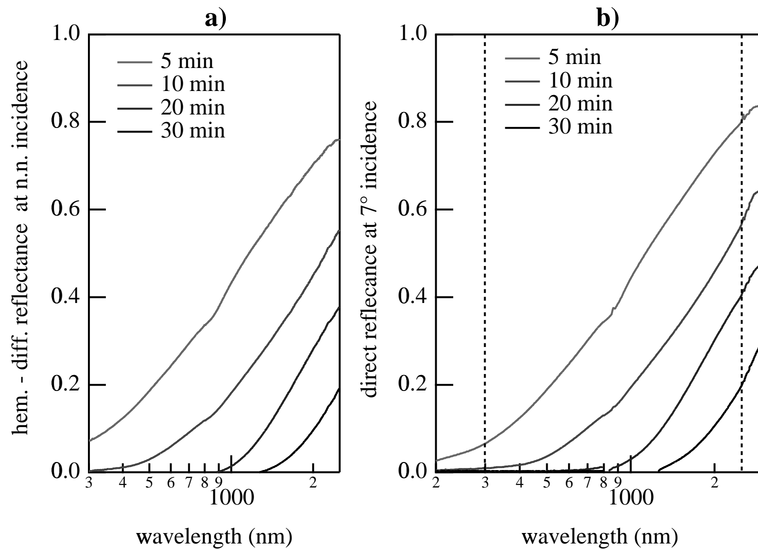

Figure 3.22: Specular reflectance for the AlO_x/AF45 samples of different thickness. a) Calculated as hemispherical minus diffuse reflectance (from figure 3.20). b) Simple 7° specular reflectance measurement for comparison.

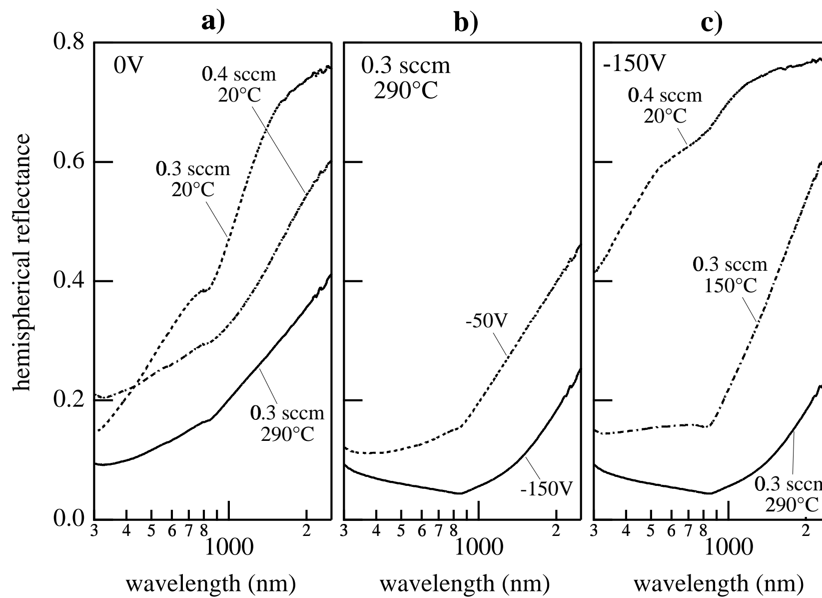

Figure 3.23: Hemispherical reflectance of AlO_x samples on Al prepared under variation in substrate temperature (a,c) and bias (b). The numbers are: the substrate bias in V, the oxygen flow in sccm and the substrate temperature in °C.

From figure 3.23 it is evident, that both an increase in substrate temperature and negative bias enhanced the absorbance in the visible and also the selectivity. In addition, variations in hemispherical reflectance were induced by changes in process pressure or target-substrate distance (not shown here). However, these effects could be compensated by a proper choice of the target power which resulted in the original deposition rate and therefore in the same stoichiometry (see section 2.2.2). Intriguing

is also the fact that the ambient temperature samples without substrate bias (left graph) showed a selective behaviour even though they appeared glossy and metallic on smooth substrates. This means that the selectivity of these glossy samples was not due to their roughness but to an intrinsic property of the cermet material itself.

In section 3.1.2 it was shown that the stoichiometry of the AlO_x films did not depend on the power type. Indeed, the hemispherical reflectance did also not significantly depend on the power supply (DC, ABP at 50/250 kHz, RF) when the samples were deposited at the same oxygen flow and fairly similar deposition rate. The same holds, if either Ar or Ne was used as the inert sputtering gas.

Analogous to the results of appendix B a positive plasma bias or a negative substrate bias had a comparable influence on the sample properties. Figure 3.24 contains hemispherical reflectance spectra from single layer samples, which demonstrate this effect. Furthermore, a double layer $Al_2O_3/AlO_x/Al$ was prepared with +120 V plasma bias for which a solar absorbance of 97.3 % was achieved. This high value is similar to the ones reported for the double layers with substrate bias in appendix A.

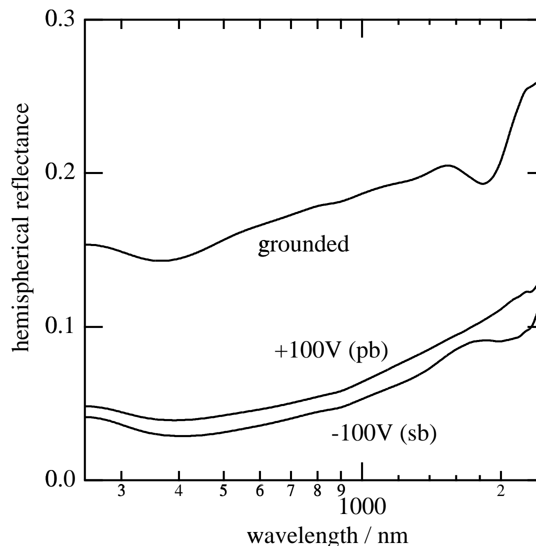

Figure 3.24: Comparison of the effects of positive plasma bias (pb) and negative substrate bias (sb) on the hemispherical reflectance for otherwise identical conditions. The process parameters: $P = 80\,\mathrm{W}$ ABP(50 kHz), $\Phi = 40\,\mathrm{sccm}$, $\Phi_{O_2} = 0.35\,\mathrm{sccm}$, $T_s = 290°\mathrm{C}$, $p = 1.7 \cdot 10^{-2}\,\mathrm{mbar}$.

One may wonder about the minimum-maximum features at the high wavelength end of figure 3.25. These are due to a comparably high oxygen content. In fact, the deposition rate for these samples was rather low (≈ 1.7 Å/s), so that a higher oxygen concentration is expected at the same oxygen flow. The occurrence of interference features for enhanced oxygen content is evident from figure 3.25, where several reflectance curves for different oxygen flow are depicted. For low values the absorbance increased with oxygen flow, whereby the typical reflectance minimum of metallic aluminium at about 850 nm was still pronounced. Beyond a certain value of oxygen content (> 0.5 sccm), this minimum vanished, the reflectance flattened and the pronounced selectivity got lost. Finally, interference features occurred at 0.8 sccm oxygen flow.

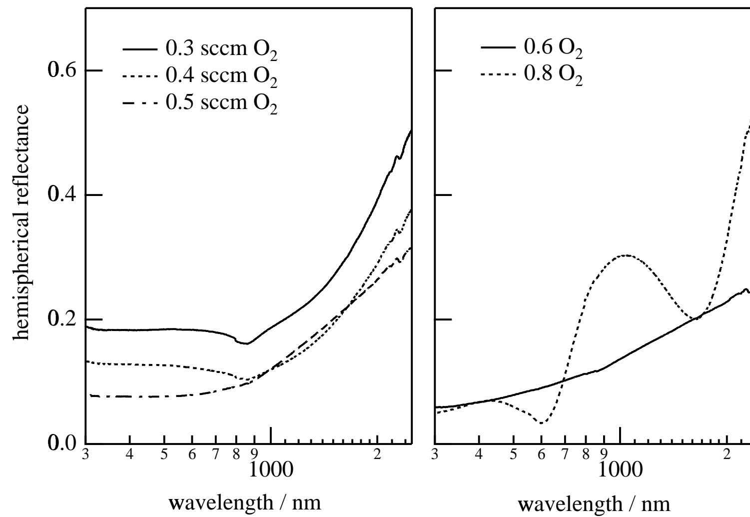

Figure 3.25: Hemispherical reflectance of AlO_x samples prepared with increasing oxygen flow. The other process parameters: $P = 100\,\mathrm{W}$ ABP(50 kHz), $\Phi = 40\,\mathrm{sccm}$, $T_s = 290°\mathrm{C}$, $U_s = -150\,\mathrm{V}$, $p = 1.7 \cdot 10^{-2}\,\mathrm{mbar}$.

3.1.5 Structure and morphology

In this section, the morphology of the random surface will be examined using AFM, SEM and the characterization methods presented in section 1.2. Moreover, evidence will be given that the hemispherical reflectance of an absorber layer is related to its surface structure in a defined way.

AFM topography

The surface morphology of the black AlO_x coatings is dominated by high aspect ratio protuberances, building up a coniferous forest type of morphology as demonstrated in appendix A. For a detailed evaluation of the statistical properties of the surface, AFM investigations are well suited, because they give - in contrast to the SEM pictures - direct information on the surface topography. Figure 3.26 shows the results of the AFM topography measurements on samples with increasing deposition time. No zooming factor was used in z-direction referred to the xy-scales. The lateral scan range was about 20 times the correlation length determined from SEM data (see below) and a 300x300 pixel data array was acquired, which results in different horizontal resolutions. The vertical resolution is about 0.2 nm. The samples look very similar concerning the lateral correlation when properly scaled in this way. As expected, the coniferous forest morphology is clearly visible and a close correlation to the SEM pictures in appendix A is evident.

In addition, three pure aluminium samples were sputter deposited on grounded Si wafers at 290°C. The results for the corresponding AFM measurements are depicted in figure 3.27. The surface corrugations are distinct from the AlO_x samples, i.e. the surface looks smoother and consists of broad interconnected islands with deep grooves in between.

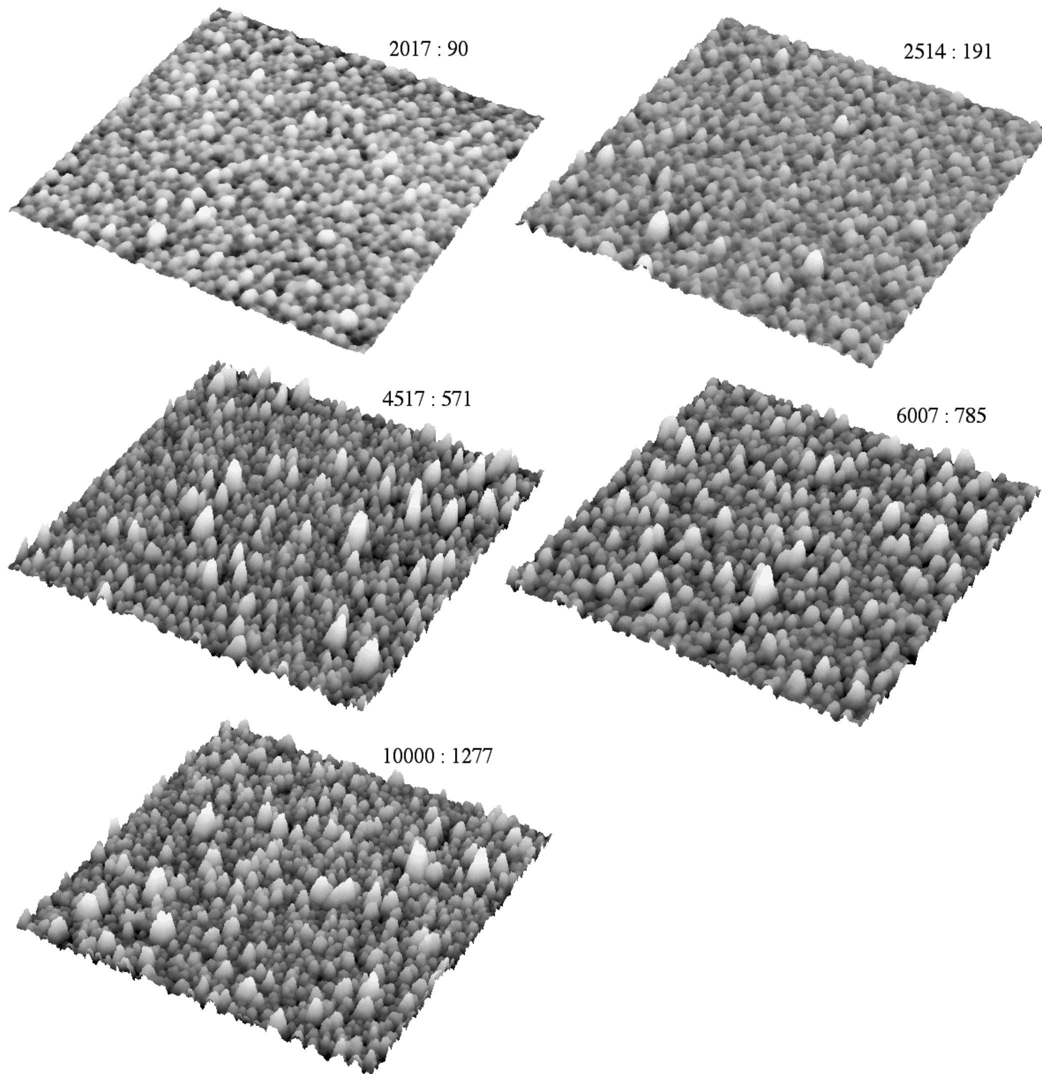

Figure 3.26: AFM topography data (non-contact mode). The numbers denote (full scale lateral) : (full scale vertical) in nanometres. From upper left to lower right: 5, 10, 20, 30 and 40 min deposition time. The lateral scan range was increased for increasing thickness, so that the pictures look very similar. The process parameters: $P = 80\,\mathrm{W}$ ABP(50 kHz), $\dot{d} \approx 2\,\text{Å}\mathrm{s}^{-1}$, $\Phi = 40\,\mathrm{sccm}$, $\Phi_{\mathrm{O}_2} = 0.3\,\mathrm{sccm}$, $T_\mathrm{s} = 290°\mathrm{C}$, $U_\mathrm{s} = -150\,\mathrm{V}$, $p = 1.7 \cdot 10^{-2}\,\mathrm{mbar}$.

Solely from simple bare eye comparison of the topography for different thicknesses, one is lead to the suggestion that the growth can be described by the concepts of dynamical growth and self-similarity.

It was then straightforward to use the statistical concepts presented in section 1.2. However, to avoid misleading results from apparatus drifts, only the *fast* scanning direction was used for a quantitative line analysis. Indeed, an evaluation of the *slow* scanning direction lead to distinct and irreproducible results. Furthermore, the scans had to be slightly levelled by subtracting a line from the original topography data. Figure 3.28 shows the local width $\omega(r,t)$ *vs.* length scale r for both the AlO_x and the pure Al samples. 40 line scans were used, whereby the data of each line scan were again ensemble averaged. In principle, all the curves show a similar behaviour,

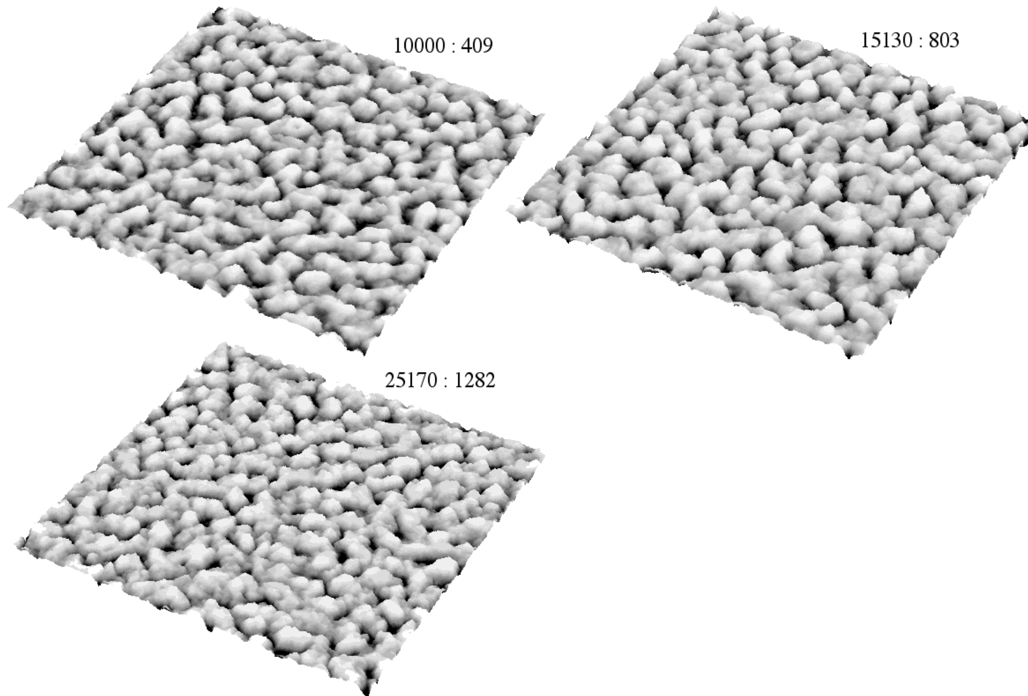

Figure 3.27: AFM topography data (non-contact mode) for Al samples prepared at 290°C without bias. The numbers denote (full scale lateral) : (full scale vertical) in nanometres. From upper left to lower right: 10, 20, and 40 min deposition time. The deposition rate was roughly the same as for the AlO_x samples in figure 3.26. Again, the scan range was adjusted to the lateral correlation.

i.e. a power law increase for low r and a crossover to a constant value. According to equations (1.13) and (1.14), the roughness exponent α can be determined from the behaviour for $r \to 0$. However, as demonstrated in figure 3.29 one has to be careful with the interpretation because of resolution effects. The result for α is significantly higher for a lower scanning range - and therefore also a lower absolute scanning speed. The effect is more pronounced for the AlO_x deposition. A similar dependence of the results on measuring conditions was observed by Zahn and Zösch [108]. For both the Al and the AlO_x deposition, a roughness exponent of 0.7 to 0.8 was therefore found, which at least serves as a lower limit. Surprisingly, the result for the roughness exponent is similar for both deposition conditions, though the appearance in figures 3.26 and 3.27 is considerably distinct.

Indeed, it is the lateral correlation length that makes them look so different. The values for the vertical and lateral correlation lengths are depicted in figure 3.31. The former is simply equal to the interface width $w(t) = \lim_{r\to\infty} \omega(r,t)$. The intersection of two tangents for $r \to 0$ and $r \to \infty$ in a log-log plot served as a measure for the latter, the lateral correlation length $\xi(t)$. Thereby, the $\omega(r,t)$ curves from figure 3.28 were used. For the AlO_x samples, the interface width $w(t)$ increases with a growth exponent near to or greater than one, whereby the straight line in figure 3.30 is an example with $\beta = 1.2$. Because of the limited number of data points, however, the error is in the range of $\Delta\beta = 0.2$. The lateral correlation length $\xi(t)$ is subjected to even higher errors, because no analytical form was found to describe the scaling function and the determination of $\xi(t)$ by the tangent method is somewhat

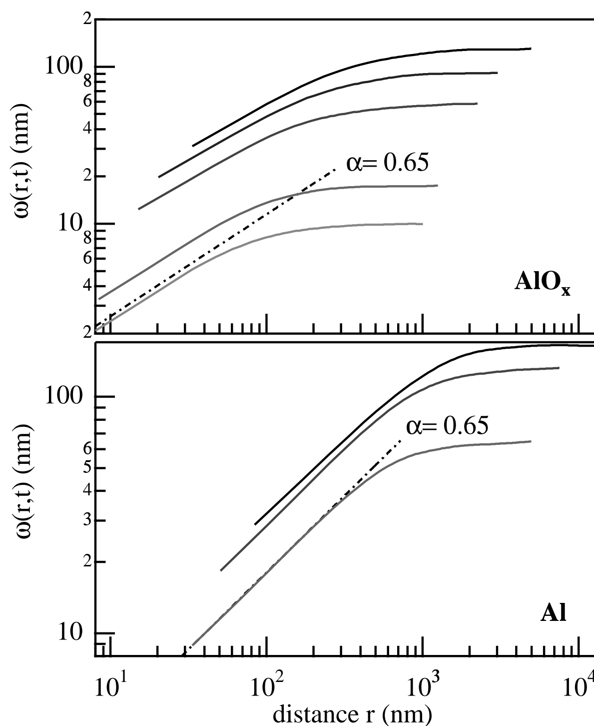

Figure 3.28: Local width $\omega(r,t)$ from AFM x-scans (the *fast* scanning direction). Top: AlO_x with 5, 10, 20, 30 and 40 min deposition (from bottom to top respectively). Bottom: Al with 10, 20 and 40 min deposition . For both deposition conditions, a roughness exponent of $\alpha \approx 0.6 \pm 0.1$ fits best to the data. However, resolution and scanning speed effects play a role as is evident from the next figure.

arbitrary. Only a very rough estimation for the dynamical exponent z is therefore possible: $z \approx 1.1 \pm 0.3$. The solid line is a fit with $1/z = 1.1$. Nevertheless, it can be clearly seen that, in comparison to the pure Al deposition, α and $1/z$ have higher values for the AlO_x deposition. This means that while the roughness of the Al films seemed to saturate, this was not observed for the oxidic films with substrate bias.

If the scaling hypothesis (1.13) holds, an appropriate vertical and horizontal rescaling should lead to a a unique scaling function. For this purpose $\omega(r,t)$ was divided by $w(t)$ and simultaneously r rescaled by $\xi(t)$. The results are depicted in figure 3.31. For the pure Al samples the rescaling is satisfying, i.e. the curves match each other very well, which supports the determination of ξ by the tangent method. In contrast, the rescaling of the local width for the AlO_x samples is not that perfect, which may be attributed to the scanning speed effects mentioned above. Another possibility is that there is indeed a change in scaling behaviour, i.e. the scaling function $g(\varrho)$ may depend on t. However, the scaling relation $z = \alpha/\beta$ is within the error bars of this analysis for the whole range of deposition times and a time dependent $g(\varrho)$ is therefore speculation.

Apart from the evaluations above, one can relate the lateral correlation length to the crossover of the hemispherical reflectance curves. Thereby, the reflectance crossover was taken at 10 % above the minimum reflectance from figure 3.20. Though this

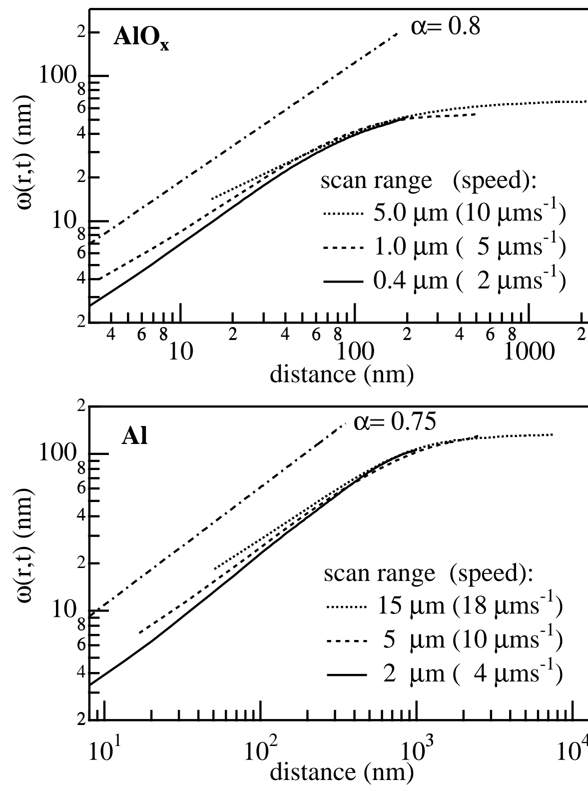

Figure 3.29: Local width $\omega(r,t)$ from AFM x-scans for 20 min deposition and different scan ranges.

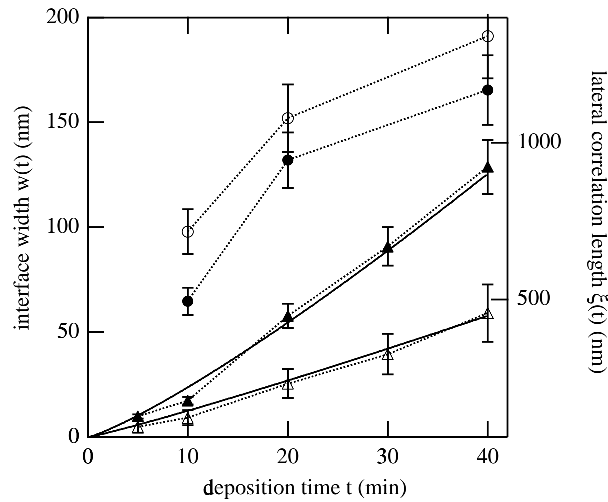

Figure 3.30: Interface width $w(t)$ (solid symbols) and lateral correlation length (open symbols) for the AlO_x (triangles) and Al samples (circles) from figure 3.26. The solid curve is a fit with $\beta=1.2$.

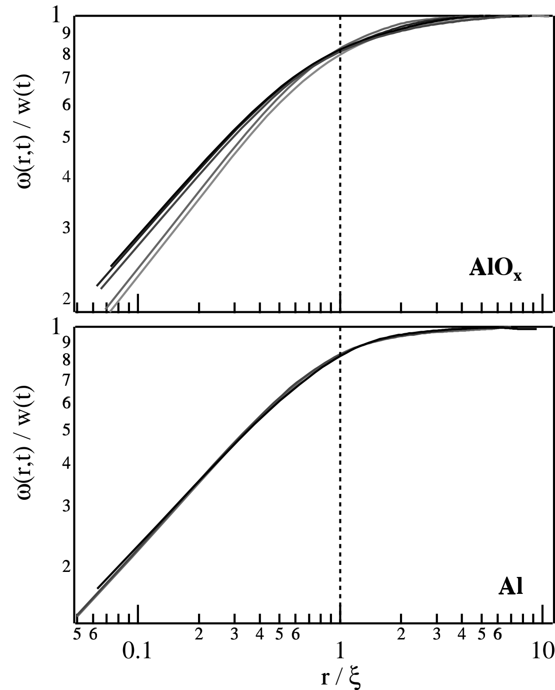

Figure 3.31: Rescaled $w(r,t)$ curves in a log-log plot. The data and grayscales from figure 3.31 were used. For the Al deposition the rescaling works better than for the AlO_x deposition.

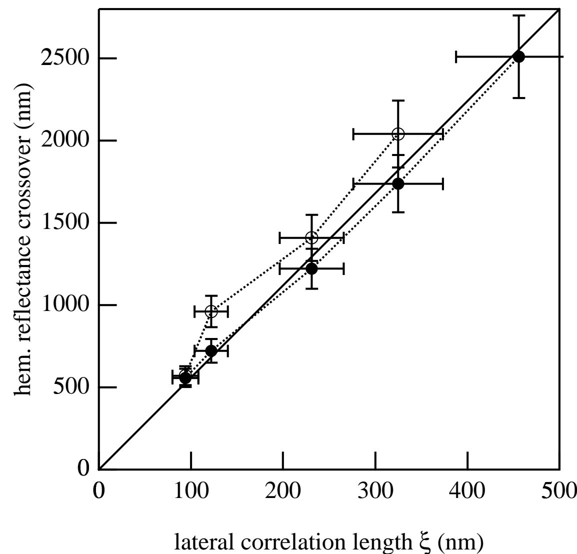

Figure 3.32: Relation between ξ and the reflectance crossover (see figure 3.20). The latter was taken at 10% above the minimum reflectance. Two distinct experimental series were evaluated, one employing Si (solid circles) and the other AF45 (open circles) substrates.

choice is somewhat arbitrary, a direct interrelation is clearly visible in figure 3.32. This fact underlines the suggestion that the optical properties are intimately involved with the morphological. In fact, the data points suggest a more or less linear interdependence, which may serve as an empirical rule.

SEM micrographs

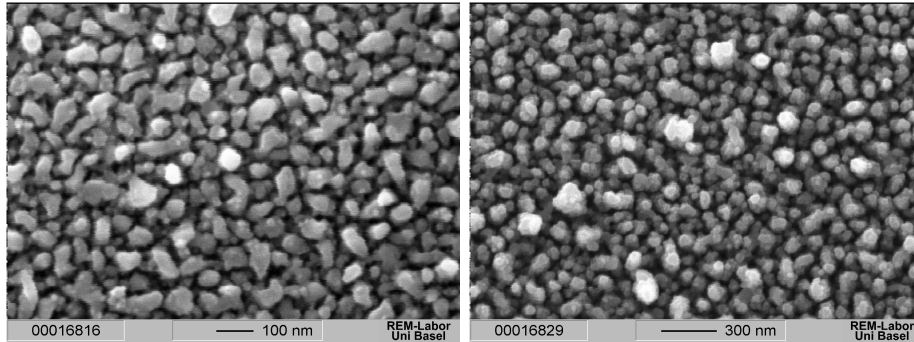

Figure 3.33: SEM topview picture of AlO_x samples prepared with 5 min (left) and 20 min (right) deposition time.

Appendix A already contains representative SEM side and obliqueview pictures of rough AlO_x. Topview micrographs of samples with 5 and 20 min deposition time are given in figure 3.33. In fact, the samples are identical to the ones depicted in figure 3.26. Two different magnifications were chosen so that the pictures appear fairly rescaled.

In principle, it should be possible to relate the SEM micrograph density (brightness) to the surface profile and evaluate the results in an analogous way to the processing of the AFM data. The problem arose of how to interpret the grayscale data. Rasigni *et al.* [109,110] gave a reconstruction scheme for the surface profile from the micrograph density. They assumed that the brightness of the micrograph is proportional to the slope of the profile height. This method was not applicable in our case, because of the high aspect ratio of the surface features and hence extreme shadowing effects, i.e. low lying points in fact appear dark. Therefore, it is rather the brightness itself that is proportional to the height. The comparison in figure 3.34 shows the close correlation between grayscale brightness and sideview height. However, besides a rough comparison to the sideview pictures there was no possibility to determine the absolute height from the SEM topview profiles alone.

Under the assumption that the grayscale plots in fact represent the surface profile data, an evaluation analogous as for the AFM data was undertaken. Figure 3.35 shows the local width *vs.* length scale r. The data are ensemble averages for 20 line scans taken from SEM pictures of different magnification. The results are not dependent on the line direction, i.e. the roughness is isotropic as expected from the deposition geometry. In principle, all of the curves show a similar behaviour compared to the ones in figure 3.28. However, one has again to be careful because of resolution effects. The horizontal resolution is given by the pixel size, i.e. about 10 nm for x10000, 2 nm for x50000 and 1 nm for x100000. Because the data were evaluated from TIFF images, the vertical resolution is roughly given by the height of the highest feature divided by 256, the number of grayscales. This vertical resolution is hard to determine exactly, because the height of the highest feature is not known. Nevertheless, it is in a significant range. Resolution effects are clearly visible for $r \to 0$, where the $w(r,t)$ curves bend up. It is presumably this fact, that leads to distinct values for α when determined from different magnifications and/or

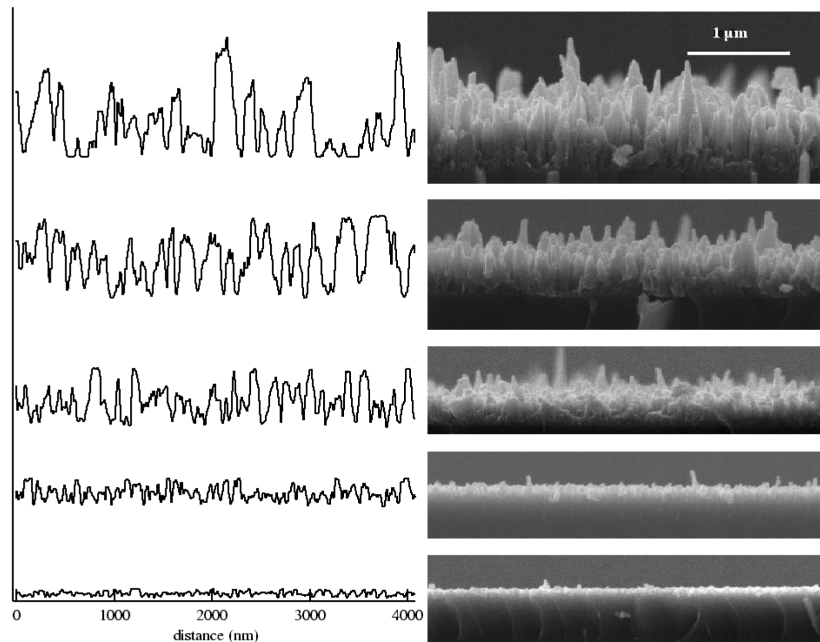

Figure 3.34: Comparison of grayscale brightness data from SEM topview to the sideview pictures with 5, 10, 20, 30 and 40 min deposition time. The brightness data on the left hand side are roughly scaled to enable a better comparison to the side view pictures on the right. However, a rigorous height scale can not be given.

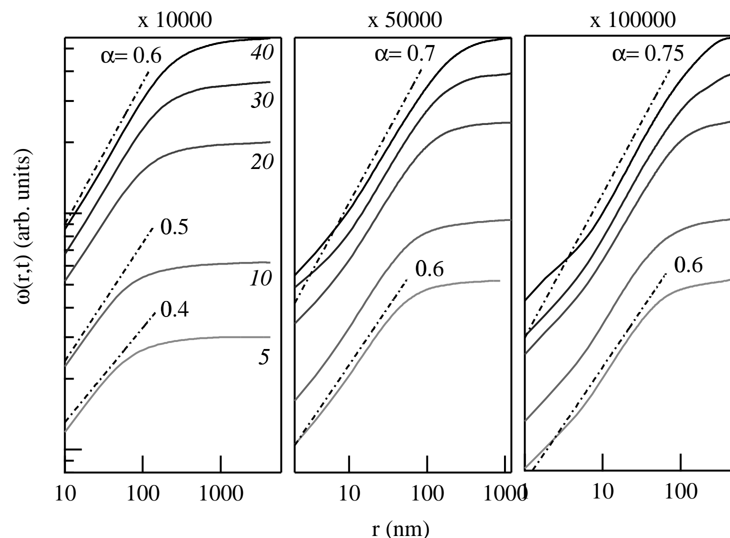

Figure 3.35: Evaluation of the roughness exponent α from SEM brightness data. Three different magnifications are depicted. The italic numbers denote the deposition time in minutes, the numbers $\alpha = 0.4 \ldots 0.75$ correspond to a scaling behaviour $\omega \sim r^{\alpha}$ $(r \to 0)$.

thicknesses. Therefore, only a rough value of $\alpha \approx 0.6 \ldots 0.8$ can be determined from the present data.

The lateral correlation length from the SEM density in comparison to the AFM results are depicted in figure 3.36. Apart from the difference in absolute values, the behaviour of $\xi(t)$ is similar.

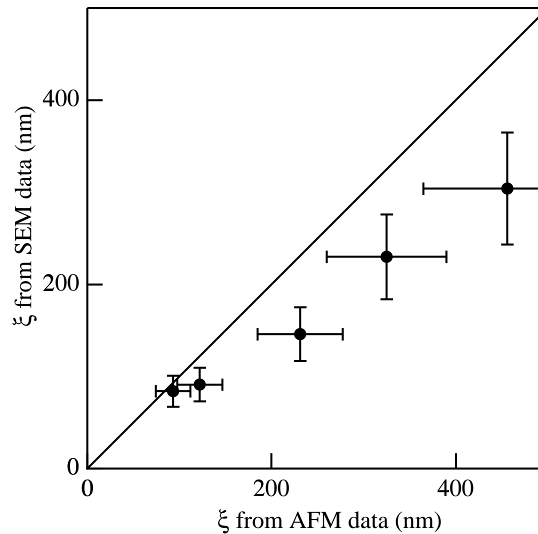

Figure 3.36: Comparison of the results for ξ for the AFM and the SEM measurements.

Though large question marks are associated with this evaluation of the SEM micrographs, the results concerning α and ξ are in reasonable agreement to the ones obtained from the direct topography data of the AFM investigations.

The SEM pictures were also very useful for an optimization of the process parameters. Two examples shall be given here: the influence of the oxygen amount (figure 3.37) and the substrate bias (figure 3.38).

Concerning the oxygen influence, it turned out that there was only a restricted range with considerable roughness of the desired form. Although the surface showed a high roughness for pure Al films deposited at 290°C, too, these films had a high colour white and diffusely reflecting appearance. On the other hand, the films were flat and transparent for oxygen flows beyond 0.8 sccm, which was apparent through the occurrence of interference patterns. In between, the typical structure size decreased with increasing oxygen flow.

With the application of substrate biasing, the small protuberances vanished in favour of the bigger ones (figure 3.38). As already evident from figure 3.23, this had an advantageous influence on the spectral selectivity.

Believing that shadowing effects play a major role in the growth of the films, one would expect an influence of the substrate tilt on the growth direction of the protuberances. Therefore, a film was deposited on a silicon wafer, which was tilted by 26° with a specially designed sample holder. The previously scratched silicon wafer was broken afterwards and viewed from the side. As can be seen from figure 3.39, the effect was surprisingly small and only very high protuberances could be used for an evaluation of the growth angle with respect to the sample normal. The result is $4 \pm 1°$.

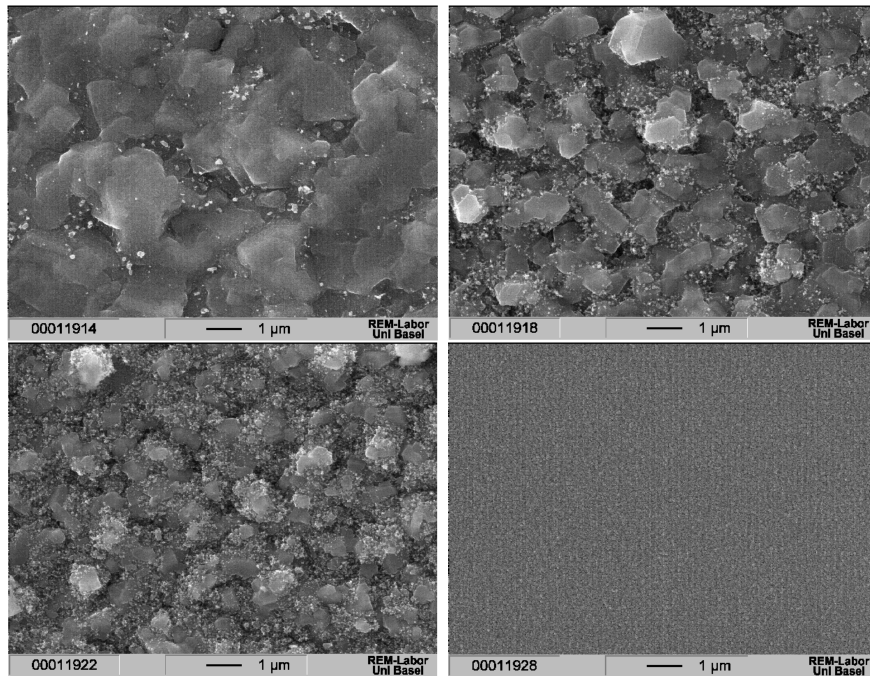

Figure 3.37: SEM topview pictures of AlO_x/AF45 samples prepared with increasing oxygen flow. From upper left to lower right: 0, 0.2, 0.4, and 0.6 sccm. The process parameters: $\dot{d} \approx 2\,\text{Å}\text{s}^{-1}$, $\Phi = 40\,\text{sccm}$, $T_\text{s} = 290°\text{C}$, $U_\text{s} = 0\,\text{V}$, $p = 2 \cdot 10^{-2}\,\text{mbar}$.

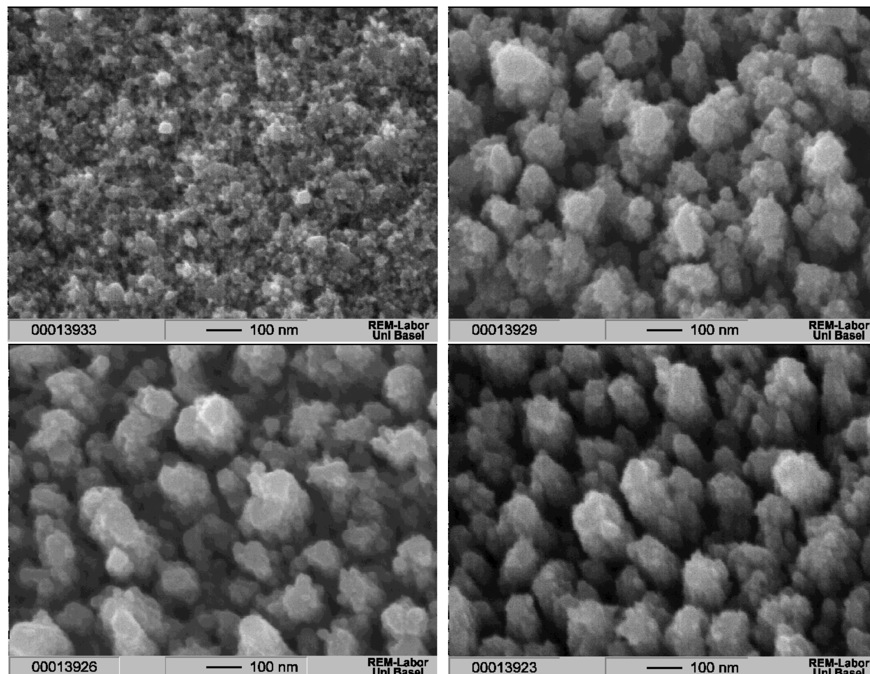

Figure 3.38: SEM topview pictures of AlO_x/Cu samples prepared with increasing substrate bias. From upper left to lower right: 0, -100, -150, and -200 V. The process parameters: $\dot{d} = 2.2\,\text{Å}\text{s}^{-1}$, $\Phi = 40\,\text{sccm}$, $\Phi_{O_2} = 0.3\,\text{sccm}$, $T_\text{s} = 290°\text{C}$, $p = 1.7 \cdot 10^{-2}\,\text{mbar}$.

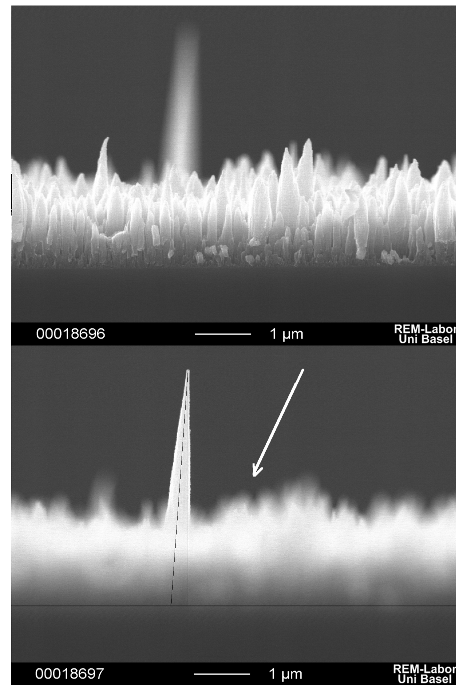

Figure 3.39: Sideview of a deposit, for which the Si substrate was tilted by 26°. Top: horizontal alignment of the substrate. Bottom: Focus on a high protuberance to determine the angle to the sample normal. The white arrow indicates the the target normal.

XRD

The thickest sample from figure 3.26 underwent a glancing angle X-ray diffraction analysis (1.5° incidence, rotating detector)[7]. The result is depicted in figure 3.40.

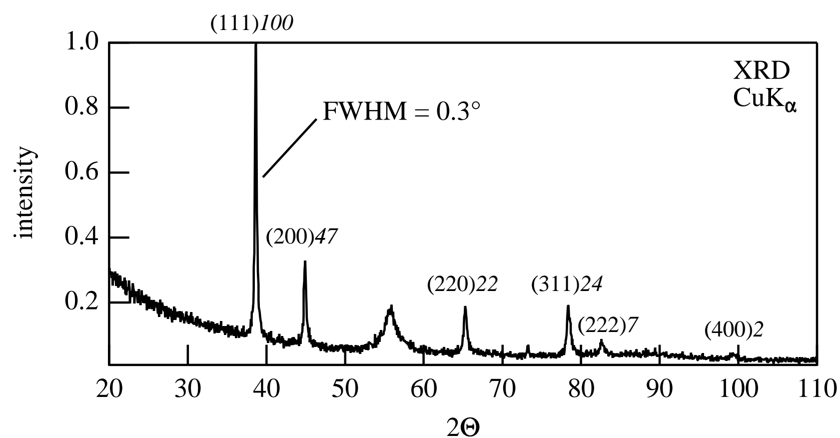

Figure 3.40: XRD spectrum of a black AlO_x absorber coating on Si. The Al peaks are marked by the *Miller*-indices (in brackets) and the powder diffraction intensities (italic numbers) (JCPDS-ICDD card No. 4-787 [111]).

Almost all of the XRD lines can be attributed to peaks from powder diffraction analysis on pure Al. Moreover, *all* of the Al lines occur and their intensity ratio is

[7]The support of G. Francz, EMPA Dübendorf, is gratefully acknowledged.

in the order of the results for the powder diffraction measurements. This is evidence for no or at least only a small texture of the films.

The broad peak at about 57° can not be addressed unequivocally but is presumably due to the distorted interface region between the Si and the AlO_x. The pronounced background can be traced back to an amorphous alumina phase. All these are further hints for a mixed Al-Al_2O_3 cermet.

With the aid of *Scherrer's* formula (see e.g. [112]), the size of the aluminium crystallites from the FWHM of the (111) line was estimated to about 30 nm.

3.2 The cover layer

Three different cover layers were employed in the course of this work: alumina, amorphous hydrogenated carbon and amorphous fluorinated carbon.

3.2.1 Al_2O_3

The sealing alumina layers were produced in the same manner as the rough deposits of AlO_x but with oxygen flows beyond 0.8 sccm. The optical thickness was chosen as $\lambda/4$ with the aid of the *real-time* reflectance as demonstrated in appendix A. The temperature stability of such a film was considerable in air. In addition, it was shown that the aging induced changes slowed down during heat treatment at 450°C. This effect was attributed to a self-sealing by an increase in alumina thickness at the surface, which acted as a diffusion barrier for oxygen. The thickness of the alumina layer is thereby expected to follow roughly a $\sqrt{t}$ - dependence [103]. Figure 3.41 shows the corresponding hemispherical reflectance spectra. As the sample underwent incessant heat treatment, the reflectance in the visible range increased while the reflectance minimum at about 900 nm got more pronounced. Such a behaviour is astonishing, because this minimum is clearly attributed to the metallic state and one would have expected an oxidation rather than a reduction of the Al atoms. The most probable explanation is that a temperature driven phase separation occurred which forced the oxygen from the bulk to the surface, leaving back more metallic aluminium.

Nevertheless, this heat treatment had no significant influence on the surface structure. Evidence for that is given by the SEM pictures in figure 3.42.

In addition, such double layered absorber coatings both on Cu and on Al passed the standard IEA temperature test [31, 101], because they showed no significant alteration of α_S and $\varepsilon_{100°C}$ even after 200 h at 250°. One of the premises in the IEA test programme is that the aging follows roughly a thermally activated behaviour. However, if self-passivation plays a major role, a thermally activated behaviour is not able to describe the aging process of the Al_2O_3/AlO_x double layers anyway. Fortunately, a self-passivative mechanism should improve the temperature resistance and the stability is expected to overcome the one of a solely thermally activated process by far.

The temperature stability was therefore promising. However, the humidity aging of the alumina sealed coatings was rather disappointing. After 60 h at 95 % humidity

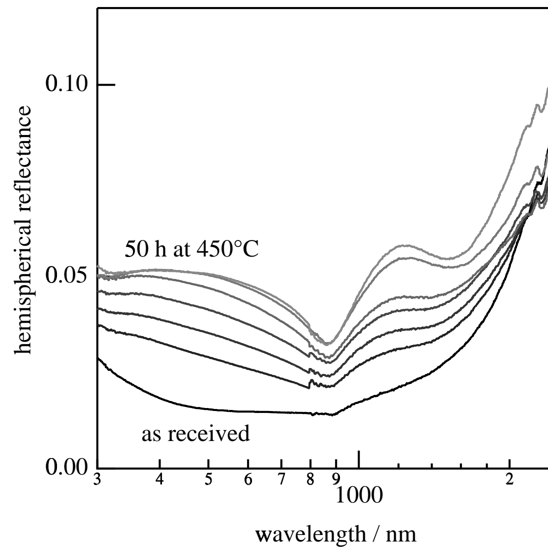

Figure 3.41: Alteration of the hemispherical reflectance during the aging at 450°C in air. Aging time from bottom to top: 0, 1, 3, 6, 10, 28, 50 h.

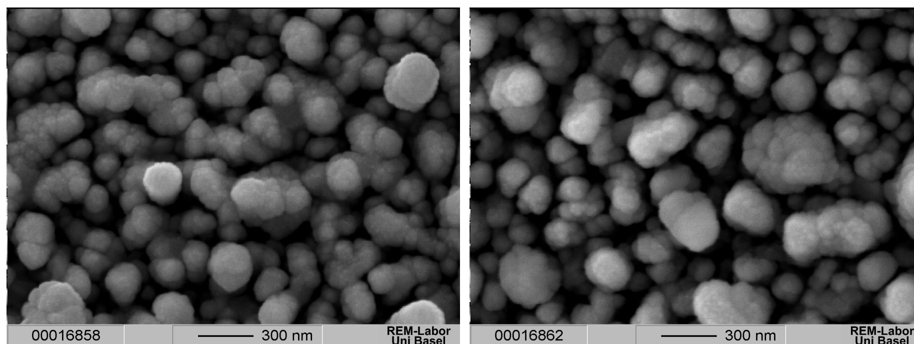

Figure 3.42: SEM topview pictures of a $Al_2O_3/AlO_x/Al$ sample as received (left) and after 50 h at 450°C in air (right).

and 45°C the films degraded extremely, so that we did not expect to improve the stability against humidity significantly with a pure aluminium-oxygen based absorber coating. Therefore, an alternative approach for the cover layer was pursued.

3.2.2 a-C:H

Very promising is the addition of a top layer of amorphous hydrogenated carbon, because it has proven to be IR transparent and very stable against humidity aging [31]. The best results concerning the absorbance were again achieved by stopping the a-C:H deposition at an optical thickness of $\lambda/4$. Figure 3.43 shows the influence of the a-C:H layer on the hemispherical reflectance. The solar absorbance is considerably improved by a $\lambda/4$ antireflection coating, whereas a thick film of a-C:H destroyed the high absorbance by interference effects.

The question arose why the adherence of the a-C:H to the AlO_x layers was observed

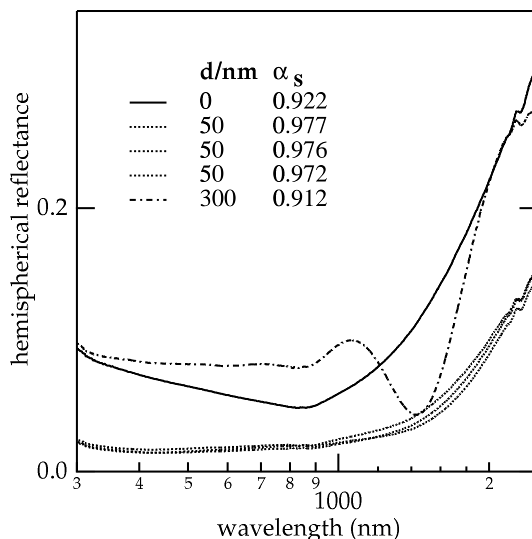

Figure 3.43: Hemispherical reflectance of a-C:H/AlO_x/Al samples. The legend contains an estimation of the a-C:H thickness d from the QMB and the solar absorbance α_s. The three layers with $d = 50\,$nm were prepared under exactly the same process conditions.

to be very good, i.e. no detachment occurred in contrast to similar a-C:H films on Cu [31]. The mechanical adhesion of thin films is believed to be mainly controlled by the chemical properties of the film-substrate interface (see e.g. [113] and references therein). Therefore, an XPS interface experiment was undertaken for both the a-C:H/Al and the a-C:H/AlO_x interface. First, Al and AlO_x layers were deposited with typical process parameters (see section 2.1.1). The next steps were depositions of a few nanometres of a-C:H (80 W ABP(250 kHz)[8], $\Phi_{\mathrm{Ar}} = 0\,$sccm, $\Phi_{\mathrm{CH_4}} = 25\,$sccm, $T_s = 290°$C, $U_s = -150\,$V, $p = 1.2 \cdot 10^{-3}\,$mbar). Due to the absence of Ar in the plasma, the target was intentionally poisoned to avoid metal contamination of the a-C:H film. After each deposition step, *in situ* UPS and XPS measurements were performed to identify the chemical state.

Representatively, the Al 2p and C 1s core line evolutions are shown in figure 3.44. The dashed spectra belong to the a-C:H/Al interface and an a-C:H deposition of about 2 nm. Additionally, a-C:H/Al cermet films were prepared for comparison. These films were produced in an analogous manner as the a-C:H/Cr [31] or a-C:H/Ti [32] previously investigated in our group. The process parameters for the 150 nm thick films were: 5 min at 80 W ABP(250 KHz), $\Phi = 25\,$sccm, $T_s = 290°$C, $U_s = -150\,$V, $p = 1.2 \cdot 10^{-2}\,$mbar. The XPS composition of these films is given in the figure, the oxygen contamination was less than 2 at%. Irrespective if the a-C:H was deposited on Al or AlO_x or even if cermets of a-C:H/Al were prepared, the Al 2p core level adopted a common binding energy value of 73.5 eV, which is believed to correspond to stoichiometric Al_4C_3 [113, 114]. Therefore, it is evident that a stable carbide formed at the interface. The C 1s level maximum had the typical binding energy of pure a-C:H [31]. Only a small carbidic shoulder is visible for an a-C:H

[8] The higher ABP frequency of 250 kHz instead of 50 kHz for the AlO_x deposition was necessary because of 'poisoning' of the target by a black carbon layer

thickness of 2 and 4 nm. However, a pronounced splitting in an a-C:H and a carbidic peak is visible for the cermet layer with the higher Al content, which justifies the nomenclature *cermet* for these films.

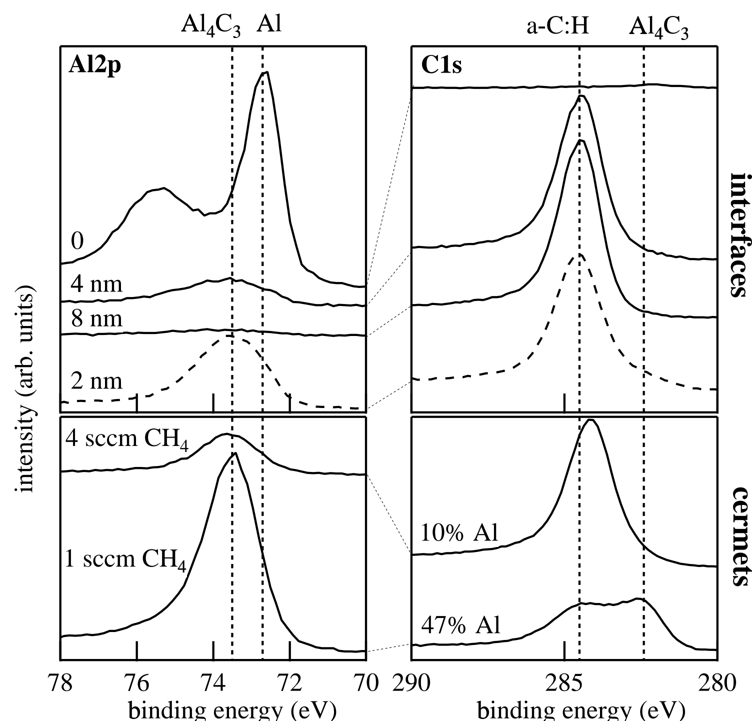

Figure 3.44: Upper part: XPS-Mg K_α spectra of the a-C:H on AlO_x interface (solid curves). From top to bottom: 0, 10 and 20 s deposition. The dashed curves belong to a 5 s deposition of a-C:H on pure Al. Lower part: Spectra of a-C:H/Al cermet layers, labelled by the methane flow and the Al concentration. The process parameters are given in the text.

The a-C:H/Al and the a-C:H/AlO_x results are in excellent agreement with earlier measurements reported by Hauert *et al.* [113] and Ernst *et al.* [114]. They deposited a-C:H on Al and Al_2O_3 respectively, whereby the substrate was at ambient temperature. The ion impact was distinctly higher than in the present work due to a higher substrate bias of -400 V to -700 V. They found that in both cases a thin film of Al_4C_3 mediates film adhesion of ultra-hard a-C:H coatings. Nevertheless, it was not *a priori* clear that the same effect would occur at the present process conditions.

Concerning temperature aging in air, it was found that the UV-VIS-NIR hemispherical reflectance of an a-C:H/AlO_x/Cu film did not change significantly during a heat treatment of 200 h at 250°C in air. If this result also holds in the infrared region, the films passed the IEA temperature aging test analogous to the Al_2O_3/AlO_x/Cu and Al_2O_3/AlO_x/Al films.

To investigate the wetting behaviour of the surfaces, the samples were exposed to droplets of deionized water. Typical photographs of these droplets on Al_2O_3 and a-C:H sealed absorbers are given in figure 3.45. The alumina samples soaked up the water like a sponge, whereas the water built up droplets on surfaces covered by 300 nm of a-C:H. However, after the sample had been tilted, residual water still covered the surface. Indeed, the humidity aging properties were not significantly

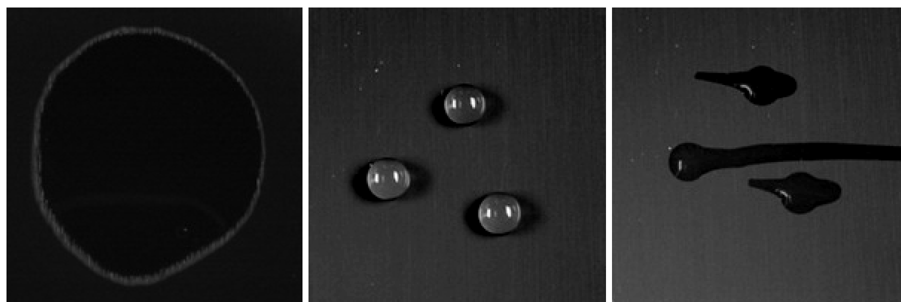

Figure 3.45: Photographs after water droplets were attached to the absorber coatings. Left: $Al_2O_3/AlO_x/Al$. Middle: a-C:H/AlO_x/Al. Right: a-C:H/AlO_x/Al after tilting the sample 90°.

better than for the alumina covered samples. The reason is not totally clear. The hydrophobicity may be improved by more polymer-like a-C:H films, not subjected to a high ion bombardment during deposition. This way was not further pursued. In fact, another class of material was employed, famous for its water repelling behaviour, namely fluorocarbons.

3.2.3 a-C:F

To improve the stability against water and humidity, it was straightforward to use a more hydrophobic surface coating. In general, fluorocarbon compounds have proven to provide high hydrophobicity [115], the most famous member of this family being teflon®[9]. Moreover, together with the structure of the AlO_x coatings it was expected to attain a highly water-repelling surface including a self-cleaning mechanism, the so called *Lotus-effect*. This effect is inherently connected with both the microroughness and the hydrophobicity of a surface. For a fundamental survey on this topic the reader is referred to literature [116–120].

As a starting point, it was tried to deposit a-C:F films in an analogous way to the a-C:H films presented in the former section, i.e. with a metal target mounted onto the magnetron drive and pure C_3F_8 precursor gas. However, the ESCA analysis always identified considerable amount of cathode metal (Al, Ta or stainless steel) at the surface. Indeed, none of the films prepared by this method on aluminium substrates showed a water repelling behaviour distinctly different from the aluminium surface itself. This effect is presumably due to the metal contamination.

To avoid metal contamination, the a-C:F films were therefore produced by conventional RF driven PACVD, i.e. without the use of a magnetron electrode. Thereby, the substrate was mounted on a grounded sample holder to avoid ion bombardment, which is known to be detrimental for the stability and hydrophobicity of fluorocarbon films produced by PACVD [121]. In fact, plasma activation by ion bombardment serves as a common tool to achieve wettability of fluorocarbons [122]. To further eliminate any metal contamination, a graphite sheet of about 5 cm diameter was used as the RF driven electrode. Carbon is a native component of the fluorocarbon films anyway.

[9] Registered trademark by DuPont

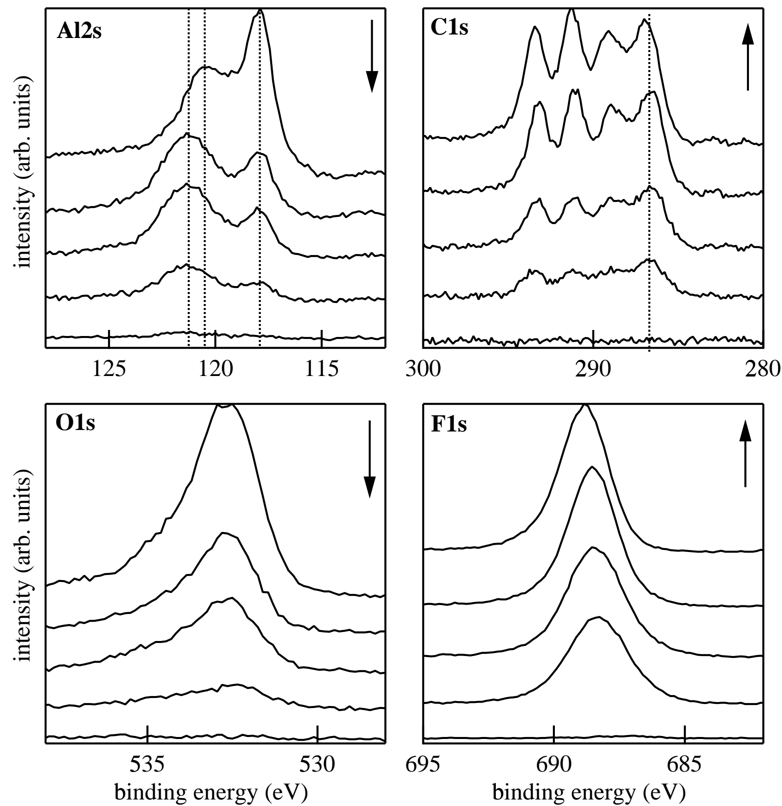

Figure 3.46: XPS-Mg K_α spectra of the a-C:F on AlO_x interface at room temperature. The arrows indicate the direction of growing a-C:F thickness, i.e.: 0, 1, 2, 5 and 11 min deposition. The process parameters are given in the text.

Again, in order to identify the chemical nature of the a-C:F films and their interface with the rough absorber coating, PES measurements were performed for two distinct substrate temperatures. The AlO_x deposits were similar to the ones used for the investigations on the a-C:H/AlO_x interface. The a-C:F deposition rate was about $1\,\mathrm{nm\,min^{-1}}$ as determined by the QMB and confirmed by the step profilometer. The other process parameters were: 10 W RF, $\Phi_{\mathrm{Ar}} = 0\,\mathrm{sccm}$, $\Phi_{\mathrm{C_3F_8}} = 4\,\mathrm{sccm}$, $p = 3 \cdot 10^{-3}\,\mathrm{mbar}$. The results are cumulated in figures 3.46 (room temperature) and 3.47 (120°C).

In both cases, the Al 2s core level changed considerably after the deposition of 1 nm of a-C:F. The oxidic part disappeared in favour of a new chemical state at 121.2 eV binding energy, presumably corresponding to Al-F or Al-O-F compounds. That the binding energy of this state is higher than for Al_2O_3 is not surprising, because the electronegativity of fluorin is higher in comparison with oxygen. Simultaneously, a pronounced C 1s signal consisting of several carbon states occurred – typical for PACVD fluorocarbon compounds. The order of the peaks in terms of decreasing binding energy matches very well the values found by other authors ([121, 123] and references therein). The peaks belong to CF_3 (293.4 eV), CF_2 (291.0 eV), CF (288.8 eV), CF_x ($x < 1$) (286.7 eV). For the thickest films small peak shifts were observed which are presumably due to a charging effect of the insulating fluorocarbon.

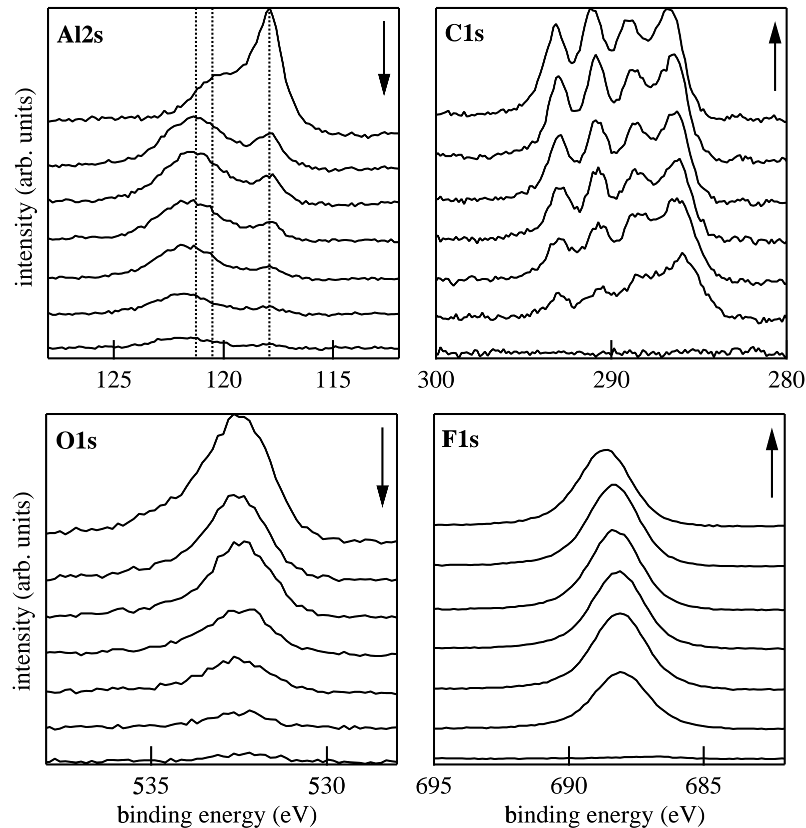

Figure 3.47: XPS-Mg K_α spectra of the a-C:F on AlO_x interface at 120°C. The arrows indicate growing a-C:F thickness, i.e.: 0, 1, 2, 5, 11, 32 and 73 min deposition. The process parameters are given in the text.

A remarkable difference between the two substrate temperatures was that the interface reaction was considerably enhanced for the higher substrate temperature. In fact, a still significant Al 2s signal was found after about 73 min of deposition at 120°C, whereas none was detectable after 11 min of deposition on a room temperature substrate. Again, this metal contamination may be responsible for the fact that the wetting angle for water on a 90 nm thick sample prepared at 120°C on Al was less than 90°. In contrast, it was larger than 90° for a comparable sample prepared at ambient temperature.

For the thickest film produced at ambient temperature the major C 1s contribution is attributed to CF_2. This result is very similar to what Horie [121] found for plasma polymerized films prepared at moderate RF power. They concluded that their films prepared from a C_3F_6 precursor exhibited higher stability and lower density of residual radicals at the surface the lower the power was, linked to an increase in the CF_2 signal. The wetting behaviour for the films prepared in the present experiment is therefore qualitatively understood. Water droplets on a-C:F films prepared at 30 W had a wetting angle $\theta < 90°$, whereas films prepared at 10 W showed up $\theta \approx 105°$.

The recipe to deposit hydrophobic a-C:F films is therefore: avoid any metal con-

tamination, reduce ion bombardment and deposit at a moderate plasma power.

Figure 3.48 shows a few sideview photographs of water drops on uncoated and a-C:F coated Si and Al substrates. It is evident that the coating reduced the wetting significantly.

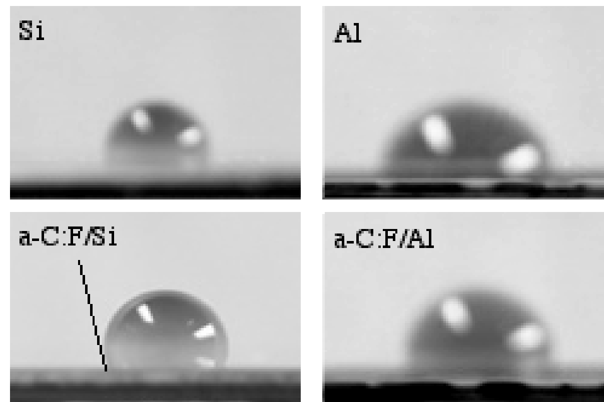

Figure 3.48: Photographs of water droplets on different flat surfaces. Though the focus was not perfectly adjusted for every picture, the influence of the hydrophobic fluorocarbon film on top of the Si and Al substrate is clearly visible. The wetting angle in the case of a-C:F/Si was estimated to 105±5°.

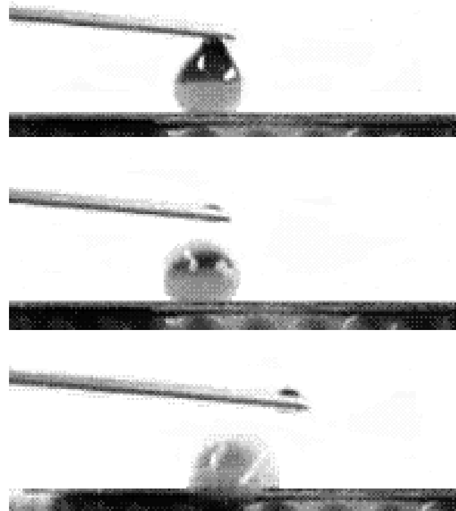

Figure 3.49: From top to bottom: Sequence from a little movie showing how the water drop 'flew' from the rough a-C:F/AlO_x/Al sample surface when released from the syringe tip.

It was straightforward to apply this knowledge to the deposition of hydrophobic a-C:F on the rough AlO_x films. Samples covered with a 90 nm thick hydrophobic coating showed up such a high water repulsion that it was virtually impossible to attach a water droplet to its surface. Photographs like the ones in figure 3.48 can therefore not be presented. However, a small sequence from a little movie[10]

[10] The support from Stephan Messmer is gratefully acknowledged

documenting a trial to attach a water droplet from a syringe to the surface is depicted in figure 3.49.

The left part of figure 3.50 shows how the surface structure of a rough AlO_x coating altered after the deposition of about 90 nm of a-C:F coating. Due to the overcoating, the surface got considerably smoother compared to figure 3.42, for instance. Nevertheless, the principle structure of the rough layer was conserved, which is certainly important for both the optical and the wettability behaviour of the films.

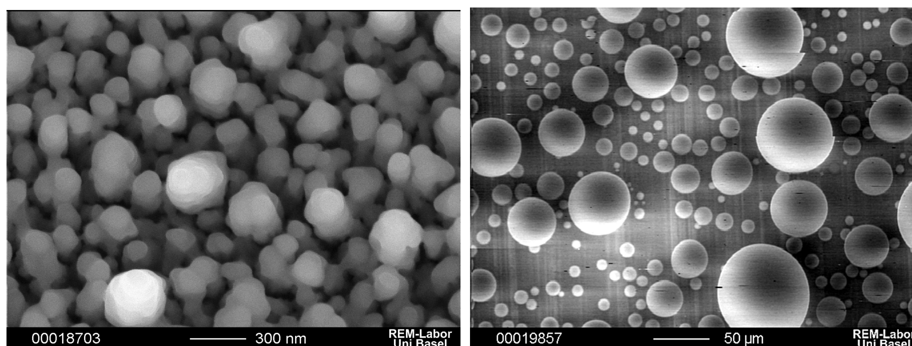

Figure 3.50: Left: SEM picture of a rough a-C:F/AlO_x/Al sample. The a-C:F thickness is about 90 nm. Right: ESEM picture of water droplets condensed on such a surface.

Microstructure and surface hydrophobicity are the two prerequisites for the *Lotus-effect* to occur. The present a-C:F coated films did show this behaviour very impressively as is demonstrated by the right hand side of figure 3.50. Thereby, water was condensed onto a sample at 3.7°C and a water vapour pressure of 8.3 mbar, which corresponds to 100 % relative humidity. The SEM picture was taken using an environmental SEM (ESEM). Spherical water droplets built up which is typical for surfaces showing the *Lotus-effect*.

The cleaning of such a surface by water drops was followed by a few short movies. Unfortunately, it is not possible to present these videos on a printed version, so only a sequence is shown in figure 3.51. Two dusty absorber coatings were exposed to water drops, one of them with (left) and the other without an a-C:F sealing (right). The dust was fine silicon carbide powder[11]. While the right sample was totally wetted, the left one was cleaned at any point where the water droplet had been guided over by the syringe tip. Very impressive was, how the uncoated sample finally soaked up the water droplet totally (bottom picture).

In addition to the sealing behaviour of the a-C:F coating, it is important how the optical properties alter with its application. Therefore, the hemispherical reflectance of a-C:F coated and uncoated substrates and absorber layers was compared (figure 3.52). For coatings on Si and Al substrates the reflectance decreased in the visible and was not altered in the NIR range. This result is promising, because the infrared mirror behaviour should not be affected by a large amount. The influence on the absorbance of a black aluminium oxide coating was also only minor and - because of the very low reflectance - within the error of the measurement.

These results on the optical influence of the a-C:F overcoatings were not surprising.

[11] SiC F 800 dark, ESK Kempten (D)

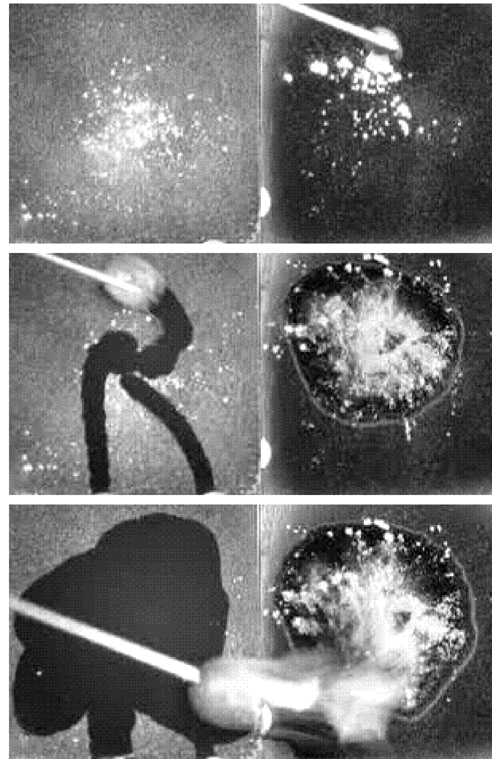

Figure 3.51: From top to bottom: Snapshots from a short movie. Two dusty absorber coatings, one of them covered by a-C:F (left) and the other by Al_2O_3, were exposed to drops of deionized water.

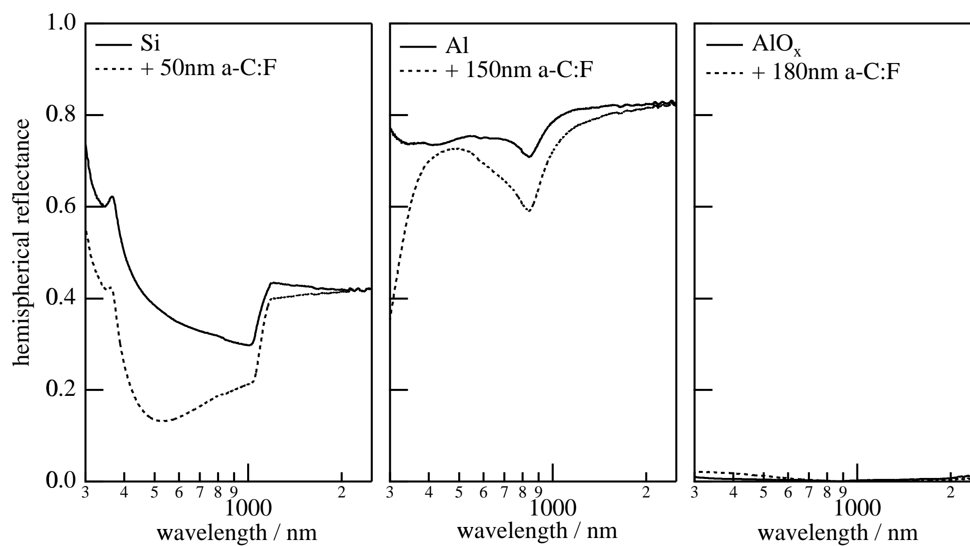

Figure 3.52: Hemispherical reflectance of a-C:F coatings in comparison to the uncoated samples. From the left to the right: polished Si wafer, Al sheet and a high absorbance $AlOx$ coating.

In the visible range, a-C:F is suitable because of its low refractive index of 1.3-1.4 [121], i.e. the reflectance should be reduced. In addition, a-C:F:H coatings have a low absorption coefficient in the infrared, which is even tunable by the hydrogen content [124]. The influence of thin films on the infrared mirror properties is therefore expected to be only minor.

Again, the temperature stability was tested whilst the samples were heated at 250°C in air. The hemispherical reflectance of a black absorber coating had not changed within the error of the measurement after 200 h at 250°C. However, this is at least partly due to the restricted sensitivity at very low reflectance values. Indeed, during the aging of an a-C:F coating on an aluminium sheet, the hemispherical reflectance approached more and more the spectrum of the underlying substrate, demonstrated in figure 3.53. Presumably, the a-C:F film was destroyed by thinning and/or aluminium diffusion. In fact, an *ex situ* XPS analysis after 200 h aging identified about 4 at% aluminium at the surface.

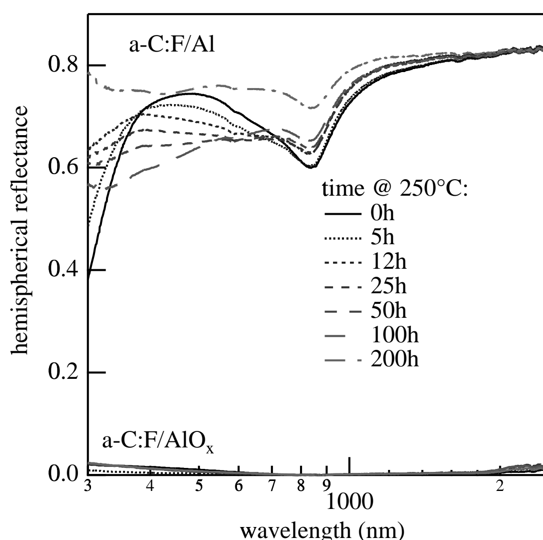

Figure 3.53: Hemispherical reflectance of a-C:F coatings during aging at 250°C in air: a-C:F on Al and a high absorbance AlO_x coating.

The aging also had an influence on the wetting behaviour of the surface. Whereas the enormous water repulsion was still observed after 50 h at 250°C, the surface was wetted after 100 h. Obviously, the metal content at the surface weakened the hydrophobicity and therefore destroyed the *Lotus-effect*. Nevertheless, a thicker a-C:F film should prolong the water repulsion during heat treatment.

Moreover, a first experiment was undertaken to compare the humidity stability of an a-C:F and an alumina coated film. For this purpose, the two samples were heated to 60° in a humid environment of nearly 100% relative humidity. As the aluminium oxide sample had already been totally degraded after 2 h at these aggressive conditions, the hydrophobically finished one was visibly unchanged after this period. However, after 5 h this sample had also been partly destroyed. It is interesting, that the degradation began at the outer edges of the sample, where the substrate was not totally covered.

3.3 TiO_x: An alternative material?

One may think of rough deposits from other metal oxides prepared with similar process conditions. A promising material is TiO_x. From the following results, only hints are deducible that it could be possible to achieve solar selectivity with this system and no rigorous evidence can be given.

Similar to AlO_x, TiO_x films showed a phase separation into oxide and metallic Ti. This is evident from the PES spectra in figure 3.54, showing XPS and UPS results on reactively sputtered films with increasing oxygen content. Similar to [125] the Ti 2p spectrum for the intermediate oxygen content is a superposition of different oxidation states, presumably consisting of Ti and TiO_2 only. For low and intermediate oxygen content the UPS spectra showed a pronounced Fermi edge.

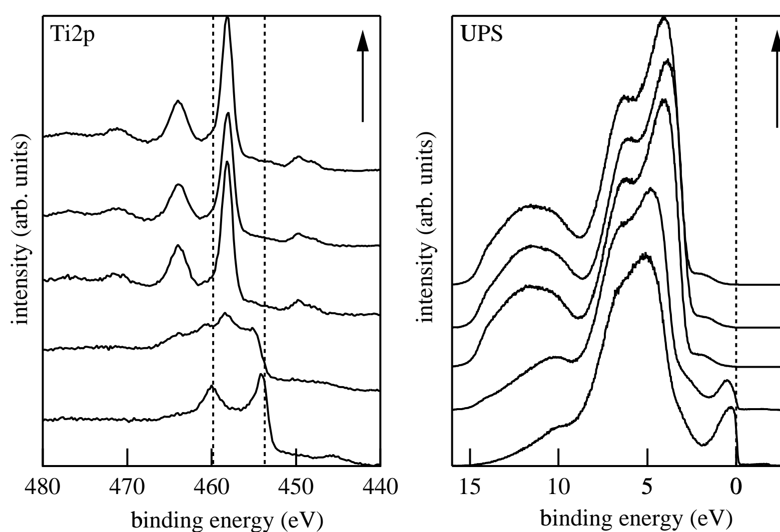

Figure 3.54: Photoelectron spectra of TiO_x films prepared by reactive sputtering of a pure metal target in an Ar/O_2 process gas mixture. The arrows indicate the direction of increasing oxygen content, i.e. from bottom to top: 30/0.9, 30/1.1, 30/1.3, 30/1.5, 30/2.0 Ar/O_2 flow.

The adhesion to the widely used Cu substrates is also expected to be high, because a strong interface reaction between the Cu and Ti was found at elevated temperature (see appendix D), analogous to the results for Al on Cu (appendix C).

Though a selective black coating similar to the AlO_x films has not been produced up to now, the first results are promising. Figure 3.55 shows an SEM picture of a TiO_x film with 0.3 sccm oxygen prepared at 385°C, the maximum substrate temperature available with the current setup. The surface shows a rugged structure with deep grooves. However, the roughness is far lower than for the AlO_x presented in section 3.1.5. Indeed, the optimum temperature for the pronounced roughening is expected to be considerably higher than for the AlO_x coatings, because it is presumably related to the melting temperature [67], which is at least for the pure Ti higher than for the pure Al.

The hemispherical reflectance of the same TiO_x sample is depicted in figure 3.56. It shows a broad minimum in the visible range, which is responsible for the dull gray

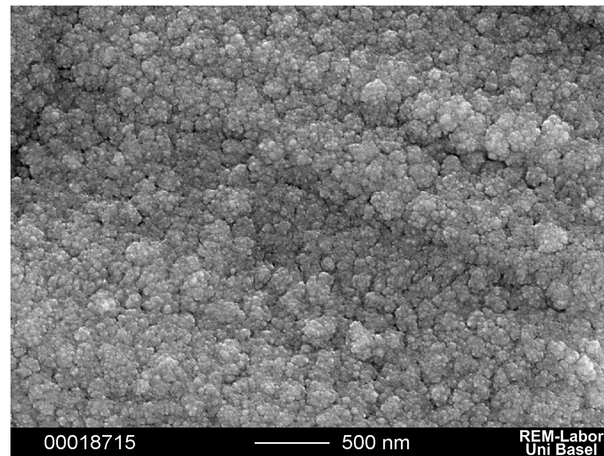

Figure 3.55: SEM topview of a TiO_x coating with 0.3 sccm oxygen flow prepared at 385°C without substrate bias.

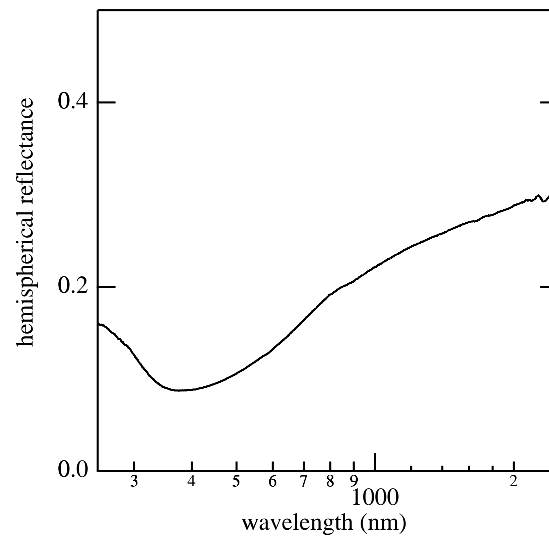

Figure 3.56: Hemispherical reflectance of a TiO_x coating with 0.3 sccm oxygen flow prepared at 385°C without substrate bias.

optical appearance. However, it is questionable, if reasonable selectivity can ever be achieved in this way. To clarify this, the parameter space has to be roved through more thoroughly.

Chapter 4

Discussion

The aim of this chapter is to put the experimental results in a more general framework by comparing them with literature. Section 4.1 is rather concise, because most of the details on deposition and chemistry have already been discussed in the last chapter. In contrast, the properties of the random surface are a less palpable topic and a more comprehensive discussion is advisable, which is presented in section 4.2. The last section of this chapter is dedicated to the feasibility of producing coatings for solar thermal or other applications with the present coating technique.

4.1 Deposition and chemistry

The rough AlO_x deposits consisted of a mixture of metallic and oxidic material as demonstrated by the PES results in section 3.1.2. Kelly and Arnell [17] deposited aluminium-oxygen coatings on ambient temperature substrates by ABP magnetron sputtering, very similar to the present deposition technique. They found a metallic behaviour of their sputter deposited coatings up to about 40 at% oxygen, in fairly good agreement with the present UPS results. Furthermore, their XRD analysis for samples with increasing oxygen content revealed a transformation from a distorted fcc aluminium (<36 at% O) to a two-phase mixed structure of crystalline aluminium and amorphous alumina, which finally ended up in a single phase amorphous alumina structure. TEM analysis showed that the grain size at 36 at% O was only in the order of 10 nm. This is in the same order of magnitude as the value drawn from the XRD measurements in section 3.1.5, though the substrate temperature was different in our case. A quite similar behaviour was observed by Stauder *et al.* [18]. In addition, they found an almost linear increase of oxygen content with oxygen flow compatible with the results of sections 3.1.1, 3.1.2 and appendix A.

The XRD analysis of both Stauder *et al.* as well as Kelly and Arnell showed that up to about 36 at% oxygen no detectable alumina domains built up, i.e. they were not visible to X-rays. They concluded that up to about 40 at% oxygen the material consisted of single phase lattice distorted fcc aluminium and that the alumina precipitates abruptly from this oxygen content on. Our XPS and UPS results indicate that the Al atoms are bonded in two distinct types for all oxygen concentrations, a metallic and an oxidic one and that the crossover to the alumina phase is rather gradual than abrupt (see also appendix A).

The effects of different process parameters on the stoichiometry have already been discussed in section 3.1.2. Within the present parameter range the results shall be shortly summarized. The major influence on the stoichiometry is originating from the oxygen process gas content and the deposition rate. No significant influence from substrate temperature and bias, power type, target-substrate distance or inert gas was identified, as long as the deposition rate was held constant by readjustment of the target power. The most probable explanation for this behaviour is, that the chemical reactions take place mainly on the sample surface and not in the gas phase of the plasma.

The results on the deposition rate as a function of power level, power source and oxygen flow can be interpreted in a similar way (section 3.1.1). The higher the erosion rate was the higher was the critical oxygen flow beyond which complete *poisoning* occurred. Moreover, the relative position of the actual oxygen flow with respect to the critical value is a measure for the oxygen content in the deposited films. For example, to adjust the oxygen content at 30 W to that at 80 W, the oxygen flow had to be reduced from 0.2 to 0.08 sccm (figure 3.11). The actual oxygen flow was indeed about 20 % of the critical value for both power levels (figure 3.1). This observation is certainly of relevance for deposition set-ups, which are not equipped with a chemical analysis method but have a simple QMB.

4.2 Dynamical growth and the random surface

4.2.1 Comparison with theoretical and numerical models

As already outlined in section 1.2 there exist a lot of models which intend to describe the formation of rough surfaces. Because one deals with statistical properties of the surface and the proposals for roughening mechanisms are numerous, it is not that easy to identify the underlying principles. Furthermore, it is obvious that several growth and relaxation mechanisms interplay during the growth of the films: sticking probability, reemission, resputtering, rearrangement, adatom mobility, surface tension and self-shadowing. Another important fact is that the films are partially oxidized, which certainly introduces random noise and has an influence on all the mechanisms above. Because of the complex nature of the growth, it is virtually impossible to ascribe a certain model unequivocally. Nevertheless, heuristic arguments will come into play, whereby the scaling analysis allows at least to rule out certain models.

The results for the scaling exponents deduced from the surface topography data of partially oxidized aluminium films in section 3.1.5 are: $\alpha \approx 0.8 \pm 0.2$ and $\beta \approx 1.2 \pm 0.2$, i.e. the scaling exponents lie in the vicinity of 1 for the AlO_x deposition. Furthermore, the *real time* reflectometry results in section 3.1.3 are compatible with a growth exponent of $\beta \approx 0.9 \pm 0.2$, which is in fairly good agreement with the topography result. The results for the Al growth are: $\alpha \approx 0.75 \pm 0.2$ and β not known exactly but presumably smaller than 1. The next step is to look for a theory which can describe this scaling behaviour in terms of reasonable mechanisms governing the growth process. In other words: One has to find a reasonable model belonging to the same universality class.

The simplest non-trivial linear continuous growth equation is the EW-equation [61], which includes only random deposition and a surface tension term. It is in principle

not able to describe macroscopic[1] roughening because the roughness and growth exponents are zero in two dimensions. Therefore, further mechanisms have to be taken into account.

The KPZ-equation [62], which is a non-linear extension of the EW-equation, introduces growth or erosion at positions of strong local slopes. This model is able to describe macroscopic roughening. However, the roughness and growth exponents from theoretical scaling analysis and numerical simulations are too low to describe the evolution of both the AlO_x and Al growth fronts observed in this work (compare to [1] and references therein). In one dimension α and β can be analytically calculated to 0.5 and 0.33, respectively. In two dimensions, only numerical results are available, e.g. $\alpha = 0.38$ and $\beta = 0.25$ [63].

In fact, to the best of our knowledge, almost none of the local continuum models is able to predict the results observed for the AlO_x growth. The only local model which may be able to describe the present AlO_x growth was presented by Golubović and Bruinsma [126]. In fact, this model was specially designed to predict the peculiarities of sputter deposition under the assumption of mass conservation, which is violated by the KPZ description. They proposed that the SOS description is only applicable in $d = 1, 2$ and breaks down for $d > 2$. In addition, they stated that the roughness exponent is underestimated by the KPZ model and presume a destabilization of the surface morphology at certain length scales. Unfortunately, a detailed scaling analysis was not undertaken in their work.

Nevertheless, we believe that non-local effects have to be taken into account to describe the growth, in particular because one deals with a sputtering process. One of the most intuitive models was proposed by Karunasiri *et al.* in 1989 [3] and shall shortly be outlined. The basic idea is illustrated in figure 4.1. On a rough surface, the deposition rate at a position x depends on $\theta(x, \{h\})$, the range of incident angles the point x is exposed to. Because of its similarity to the growth of grass, for which the growth velocity of a grass blade depends on the amount of light impinging on the blade, this model is sometimes called *grass model*. However, the difference with the growth of grass is, that surface diffusion and surface tension play a major role on a condensed matter surface. The basic equation introduced by Karunasiri *et al.* is

$$\frac{\partial h(x,t)}{\partial t} = -D\frac{\partial^4 h(x,t)}{\partial^4 x} + R\,\theta(x, \{h(x',t)\}) + \eta(x,t) \quad , \tag{4.1}$$

where D is proportional to the surface diffusion constant and $\{h(x',t)\}$ is the whole set of height values. Equation (4.1) is therefore a differential - functional equation, *non-local* and consequently *non-linear*, too. The surface tension term $(\partial h/\partial x)^2$ was neglected for the first investigations by Karunasiri, i.e. no *local* non-linearities were added. The major results drawn from numerical simulations were: a self-similar mountain landscape very similar to the one observed for the AlO_x deposition in hand, a roughness exponent ≥ 0.5 and a transition to columnar structure for higher D, if a non-linear term $(\partial h/\partial x)^2$ was included. In addition, it was predicted that initially a flat film grows up to a critical height, which is given by $h_{crit} \sim (D/R)^{1/3}$. This means that the roughening occurs at a lower nominal thickness for low surface diffusion. The grass-model exhibits an intrinsic growth instability, which is *not* noise driven.

[1] In this context, macroscopic means far from the atomistic scale

In contrast, the Eden and other local models predict roughening instabilities only in the presence of noise. Karunasiri *et al.* expected growth exponents of 0.7 ... 0.8 if noise was present in their *grass model* [3].

A comparison between figures 4.1 and 4.2 clearly reveals the close kinship between the model and our results, even for the pure aluminium films. It is intriguing that - under proper rescaling - the *equal-time* height profiles for the AlO_x and the Al samples look very similar. Indeed, they have a comparable roughness exponent α, which is a measure of the *equal-time* roughness properties. In fact, even the untrained eye can distinguish between profiles with distinct α (see e.g. [1,58]).

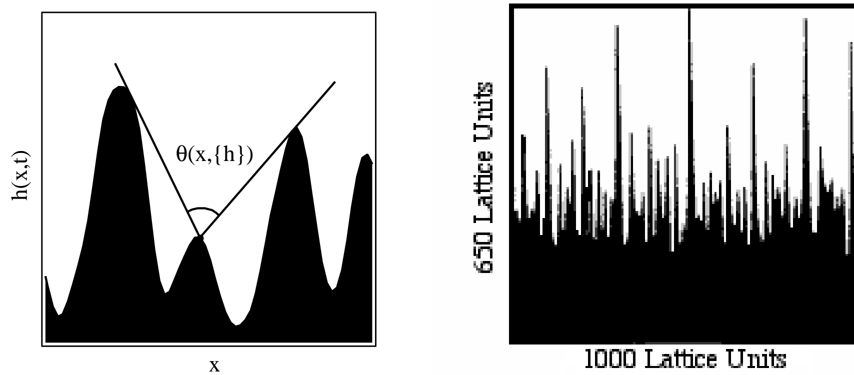

Figure 4.1: *Non-local* shadowing effect proposed by Karunasiri *et al.*. Left: The growth velocity at a point x depends on the range of incoming angles, denoted by $\theta(x, \{h\})$. Right: Surface profile data for $D/R = 0.1$ (from [3]).

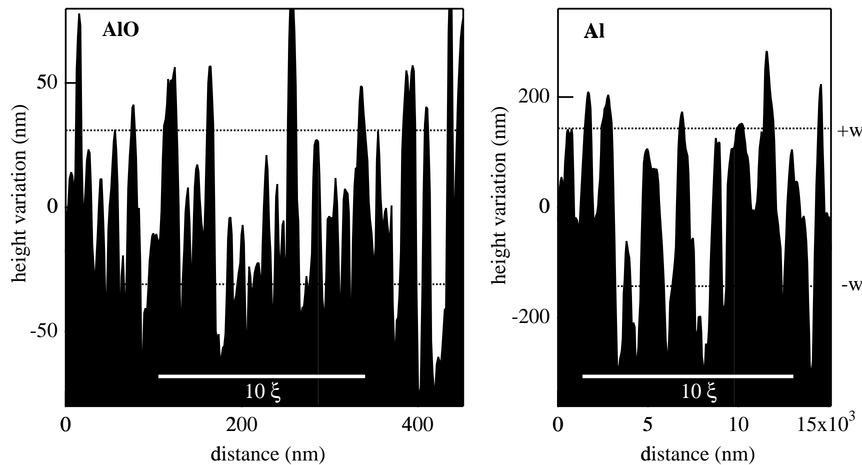

Figure 4.2: Representative profile line scans from AFM measurements on samples with 20 min deposition time. The dotted lines are located at plus and minus the interface width. The white bars indicate ten times the lateral correlation length. In fact, the width of the graphs was chosen to enable a direct comparison.

Bales and Zangwill [5,6] and Tang *et al.* [4] extended this model. The basic idea was to split the surface in broad column tops obeying a *Huygens-Principle* type of growth and deep, cusp - like narrow grooves. These models were able to explain the growth phenomena observed by Messier and Yehoda [66] for pyrolytic graphite. Particularly, the effect that only the strongest columns survived during growth, could excellently be modelled by numerical simulations.

Srolovitz *et al.* modelled the occurrence of the different growth zones observed by Thornton [67]. The distinct structure and morphology of these growth zones were found to depend mainly on the ratio between substrate temperature T_S and melting temperature T_M. In the model of Srolovitz *et al.* T_S/T_M tailored the fastest growth mode. In addition, they predicted that the typical length of this growth mode lies in the range of the wavelength of visible light for $0.3T_M < T_S < 0.5T_M$. For our pure Al deposition there is in fact $T_S \approx 0.44T_M$. Obviously, a single melting temperature does not describe the AlO_x films and a comparison to this model is difficult. The linear form of the Srolovitz-model describes a decay of surface modes smaller than a typical diffusion length λ_0, which depends on the surface diffusion constant D, the atom size and the deposition rate J: $\lambda_0 \sim (D/\delta J)^{1/2}$. A higher diffusion constant D therefore implies bigger columnar structures, in qualitative agreement with our observation, that the lateral correlation length decreased with increasing oxygen flow.

Indeed, the oxygen gas adsorption certainly causes not only a decrease in surface diffusion but also local adatom mobility variations, resulting in a considerable amount of noise. However, random noise was not included in the model of Srolovitz *et al.* and might change the growth properties.

A pair of coupled differential equations was the starting point for more recent numerical simulations by Keblinski *et al.* [7]. In contrast to the SOS-models they allowed for overhangs, voids and holes. In the case of pure *vertical rain*, i.e. only transverse deposition of particles, and $d=1$ the simulations revealed roughness exponents close to the KPZ-values. However, in $d=2$ only the value of $\beta \approx 0.2$ could be estimated and no result for α was given. An intriguing point is that they observed a transition from self-similar to non self-similar behaviour for non-vertical rain, which they simulated by a symmetric off-vertical rain model[2]. For medium values of the incident angle the interface was characterized by a well defined length scale and columns with deep grooves grew along the vertical symmetry direction. Incident angles $\geq 80°$ brought the film to a fractal shape with a temporal growth exponent $\beta \approx 1$. Though symmetric off-vertical rain is certainly a simplification of the actual wide range of incident angles, the model provides a feeling for the significance of this effect.

A numerical comparison of continuous and pulsed deposition for both thermal and energetic particle deposition was recently undertaken by Mayr *et al.* [8]. They concluded that the roughness is smaller for energetic particles than for thermal deposition, which is also evident from their calculated height-height correlation functions. Moreover, the difference decreases with increasing substrate temperature. In the high temperature regime they found a roughness exponent $\alpha \approx 0.95 \pm 0.1$, near to the value for the AlO_x deposition observed in this work.

[2] This break-down of the SOS behaviour in $d=1$ is in contrast to the local theory of Golubović and Bruinsma [126].

In section 3.1.5 it was shown that the growth angle was about 4° if the substrate was tilted by 26°. Hodgekinson *et al.* [127] proposed an empirical model for spatially modulated thin film nanostructures which widely occur as the deposition angle is altered ([66] and references therein). A tangent rule connecting the deposition angle θ_v to the column angle ψ was proposed:

$$\tan\psi = e_1 \tan\theta_v \ , \quad e_1 < 0.5 \quad . \tag{4.2}$$

The value e_1 is in the range of 0.14 for the AlO_x deposition, which is rather low compared with the values presented by Hodgekinson *et al*. Therefore, it is suggested that a considerable surface tension is present, which forces the protuberances to grow perpendicular to the substrate. Furthermore, gas phase collisions certainly spread out the range of incident angles and the effect due to the tilting is reduced.

As already pointed out, random impurities may influence the surface evolution. Kardar [129] suggested a universal behaviour for the roughening by impurities at finite temperature, inspired by an analogous result for the roughening of magnetic domain walls [130]. A roughness exponent $\alpha = 2/3$ was proposed, within the error range of our present investigations.

By a comparison of our results to all these models and numerical results, one is able to draw some plausible conclusions on the mechanisms leading to the rough films:

- Linear growth equations are not able to describe the macroscopic roughening.
- At least for the AlO_x films local non-linear and noise driven models are not sufficient to describe the growth properties, though they describe macroscopic roughening.
- Non-local models like the ones proposed by Karunasiri *et al.* or Bales and Zangwill are able to describe surface morphologies like self-similar mountain-shaped structures or broad columns with deep grooves. Which topology is adopted depends on the counteracting of surface diffusion, shadowing and surface tension. In the presence of oxygen the adatom mobility is presumably reduced and a roughening instability is observed at shorter time and length scales. This roughening instability is assumed to be driven by the counteracting of shadowing and surface diffusion.
- The application of a substrate bias causes considerable ion bombardment which supports the formation of protuberances with lateral correlation lengths well suited for spectral selectivity (see section 3.1.5). This observation may be included in the 'survival of the strongest columns' - effect described by the non-local models above.
- The random deposition process, the resputtering and the partial oxidation introduce a considerable amount of noise to the process, which may be advantageous for the formation of a random rough surface.

The roughening mechanism is attributed to a non-local and non-linear behaviour. Therefore, it is *not* clear at all that an upscaling process to industrial standards is possible. Parameter variations exceeding those examined in the present work may lead to a totally different growth regime.

4.2.2 Comparison to other experimental results

A bare eye comparison of SEM images from AlO_x films produced in this work with the pure Al films reported by Wan *et al.* [11] shows an astonishing similarity. Because they gave no details on base pressure and purity of their films, we suggest that maybe a considerable amount of contamination was present which lead to a surface topology similar to the one observed for the oxidic films in our work.

That magnetron sputtered pure Al films show a self-similar morphology was already shown in the work of Yan *et al.* [9] as well as Lita and Sanches [10]. In the former work, the influence of substrate temperature and deposition time was investigated. Their films had a surface morphology very similar to that of the pure Al films presented in section 3.1.5. The RMS roughness increased with increasing substrate temperature and deposition time, comparable to our results. A comprehensive ambient temperature study was presented by Lita and Sanches. Two self-similar roughness regimes were identified, whereby the roughening with a growth exponent of 0.55 was attributed to shadowing effects.

A variety of other elementary materials produced by either sputter or vapour deposition was investigated. You *et al.* [75] showed that for sputter deposited gold films at substrate temperatures below 350 K, the growth exponents determined from either specular X-ray reflectivity or STM data were in good agreement. The values they found were $\beta \approx 0.4$ and $\alpha \approx 0.4$, which are not compatible with a KPZ description. In contrast, Thompson *et al.* found other values for the growth kinetics of vapour-deposited silver films on ambient temperature silicon substrates: $\beta \approx 0.26$, $\alpha \approx 0.7$. Buzio *et al.* [131] studied the evolution of cluster assembled carbon thin films by AFM and found roughness exponents in the range of 0.6...0.7 and growth exponents near 0.5. Recently, Dharmadhikari *et al.* [76] measured similar exponents of $\alpha \approx 0.7$ and $\beta \approx 0.5$ for platinum deposition by electron beam evaporation. Both scanning probe techniques and X-ray scattering were employed.

Rasigni *et al.* evaluated shadowed SEM microdensitometer data for rough deposits of copper, silver and gold [109] for the application to solar energy conversion. They used a special method [110] to reconstruct the actual surface profile. A roughly linear relation between the RMS roughness (interface width) and the lateral correlation length was found. A scaling analysis according to equation 1.13 was not pursued by Rasigni *et al.* because the scaling hypothesis was in fact not stated at that time. Nevertheless, from their SEM micrographs one can conclude that the rough deposits of Au, Ag and Cu showed a surface morphology typical for conventional vapour deposition, i.e. without deep grooves.

All these experimental observations on elementary materials do not seem to match the universality class of the rough AlO_x deposition, especially concerning the value of β.

The impurity content certainly has a dramatic influence on the growth properties as demonstrated in several publications on Al and other coating materials. The work of Sproul *et al.* [16] is closely related to our work. They produced magnetron sputtered aluminium-oxygen coatings with a wide range of oxygen content on floating substrates, i.e. negatively self-biased, and obtained non-stoichiometric oxides with a gray appearance. This result is very similar to what we found. Kelly and Arnell [17] identified a significant variation in coating structure with oxygen content. They proposed a new structure zone model describing pulsed magnetron sputtered

aluminium oxide coatings on ambient temperature substrates: a *porous columnar* structure for metallic films, a *dense columnar* structure for substoichiometric oxides and a *fully dense* structure for stoichiometric alumina. This model may now be extended by a *coniferous forest* type of morphology for substoichiometric films deposited at elevated substrate temperature.

Ross and Messier [132, 133] investigated the growth of RF-sputtered amorphous silicon for various process gases (Ar+H_2, Ne, Ar and Kr) and different pressure regimes using SEM and TEM. With increasing pressure, the films exhibited an increasing amount of distinct vertical columns with deep grooves in between. In addition, a negative substrate bias caused a reduction of the columnar microstructure via rearrangement of the surface due to the Ar^+ ion bombardment. This seems somehow to contradict our results, whereas it is similar to the observations for TiN films in appendix B. Concerning the influence of different inert gases, the type of gas did not influence the growth significantly, analogous to our result when using Ne instead of Ar. On the contrary, the relative concentration of inert gas and hydrogen had a fairly strong influence, a hint on a significant effect of impurities.

A more recent SEM study of laser irradiated silicon surfaces in gaseous environment [134] - which is indeed not directly related to sputter deposition - revealed an anomalous microcolumn growth. The tips of the high aspect ratio silicon columns were terminated by spherical caps. As an explanation, the authors suggested that the laser ablated and redeposited material was responsible for this structure. The interesting fact is that the microcolumn formation only took place in an oxygen containing atmosphere – analogous to the observations in hand.

4.3 Optics and applications

4.3.1 Absorbance and reflectance

With the deposition method for the rough AlO_x coatings studied in this work it was possible to produce black films with a high solar absorbance up to 99 %. Moreover, the absorbance could be very easily tailored by the choice of thickness, which shifted the lateral correlation length and the reflectance crossover according to figure 3.32. In particular, the absorbance was extremely high and broadband for thick films (see e.g. figure 3.52). However, the thermal emittance of coatings with solar absorbance values beyond 90 % was never below 10 % up to now, which is - in comparison to some industry products - too high for the standard application in a flat panel solar collector, where the solar flux is not concentrated. The reason for this problem lies in the relatively flat crossover-regime (see e.g. appendix A). Nevertheless, as can be deduced from equation 1.1.2 the figure-of-merit of a solar system strongly depends on the solar concentration factor and the absorber temperature. Therefore, the AlO_x films may be useful for some special application, i.e. if a very high absorbance is desirable and the emittance of heat radiation is secondary. A comprehensive survey on the figure-of-merit for different scenarios is given by Seraphin and Meinel [24] and shall not be outlined here once more.

In fact, a comparably broad reflectance crossover may have an unexpected technical advantage: it prevents the absorber from overheating. The hotter the surface the higher is the amount of emitted power by heat radiation. The reason for this is

that the maximum of the thermal radiation shifts to lower wavelengths according to *Wien's* law and the radiation losses therefore increase according to equation (1.4).

An undoubtably advantageous property of the AlO_x coatings is that the selectivity does not rely on an infrared reflecting substrate material like copper or aluminium. In fact, the high IR reflectance is a property of the coating itself.

All in all, it would be very helpful to have an influence on the width of the crossover and not only on its position. A more detailed study on the growth properties of the AlO_x films in connection with a fundamental understanding of the interplay between surface structure and reflection properties may help. Indeed, the parameter space could not be totally scanned in the course of this work. For instance, even higher substrate bias or gradual changing parameters may help to sharpen the crossover.

4.3.2 Stability and wettability

As demonstrated in appendix A, the temperature stability of the Al_2O_3/AlO_x films is suitable for applications up to 350°C. However, the stability against humidity of such a film was found to be lousy, so that an application seems to be only useful in dry or vacuum environment. For the application in vacuum tube collectors, however, the optical properties, i.e. ε_T should be improved for a proper performance in weak-concentrating systems.

It was straightforward to cover the absorber coatings with a more stable material concerning humidity aging. Unfortunately, a-C:H sealings prepared by a method analogous to [31] and [32] were not sufficient.

Obviously, a fluorocarbon surface coating was a reasonable choice due to its hydrophobicity. The first results on the humidity aging stability were promising, though a further improvement seems to be advisable. Besides, the a-C:F sealed films showed an effect, which is intriguing from both a practical and a more fundamental point of view: The massive water repulsion from a microrough and hydrophobic surface, which lead to the famous *Lotus-effect*.

To the best of our knowledge, this work is the first to combine the optical properties of a rough surface with its water repulsion behaviour. The a-C:F/AlO_x system showed up the interplay between self-similar surface structure, optical selectivity and *Lotus-effect*. The strength of the water repulsion certainly depends on the amount of roughness. Up to now it was shown *that* a massive water repulsion can be achieved on comparably thick coatings (>400 nm nominal AlO_x thickness). An inalienable condition was that a proper deposition technique for the a-C:F was chosen (section 3.2.3). The AlO_x surfaces showed a self-similar shape with lateral and vertical correlation lengths depending on thickness (section 3.1.5). Therefore, a model system was found to study the counteracting of surface structure and water repulsion further.

Onda *et al.* [118] observed both *super water repellent* and *superwettable* behaviour for hydrophobic and hydrophilic fractal surfaces respectively. The superwettable behaviour of the bare AlO_x surface is evident from figures 3.45 and 3.51, i.e. the surface acts like a sponge for water. Moreover, super water repellence was produced by the hydrophobic finishing of the self-affine AlO_x surfaces by a-C:F.

Another advantageous property of the AlO_x coatings is that the adherence to many substrate materials is expected to be high, owing to the chemical reactivity of alu-

minium. The films did not peel off from none of the substrate materials used in this work, i.e. Cu, Al, glass, and silicon. Furthermore, hydrocarbons and fluorocarbons on top of the AlO_x formed chemical bonded interfaces, which was evident from the XPS analysis (sections 3.2.2, 3.2.3). It is therefore most probable that it also works the other way round, i.e. that the AlO_x adherence on hydrocarbons (e.g. polymers) and fluorocarbons (e.g. teflon®) is high. In combination with the inherent IR reflectance of the coatings, many different carrier materials are feasible.

Résumé

Summary

The most important conclusions drawn from the results and discussions within this report can concisely be summarized in figure 4.3.

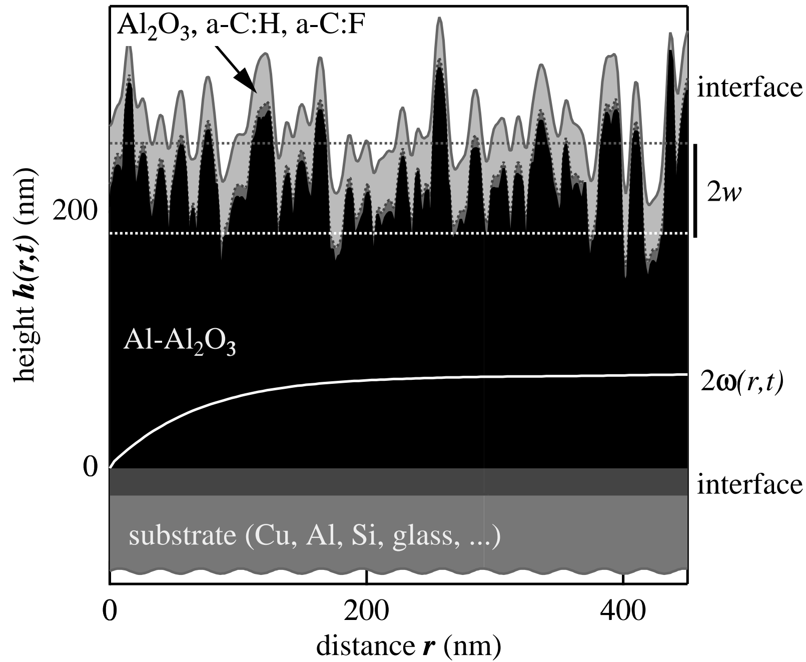

Figure 4.3: Scheme of an absorber coating discussed in this work.

The absorber coating is depicted in black. The top boundary of this AlO_x absorber coating is in fact a representative AFM scan. The mean height is chosen to be the nominal thickness estimated from the QMB data and the density taken from the profilometer measurements on flat samples. Furthermore, the scales for r and h are equal, so that there is no scale distortion. In addition, the ensemble averaged local width calculated from 20 such line scans is also depicted. It shows how the roughness first increases and eventually saturates with lengthscale. The value for which the local width saturates is a measure for the lateral correlation.

Owing to this scaling behaviour, such a surface reveals a dynamic self-similar structure, i.e. it shows the same statistical behaviour under a certain rescaling of length and time scales. The statistical properties, i.e. the scaling behaviour, are most probable due to shadowing effects, oxygen limited surface diffusion and random noise. The thickness of the layer determines the lateral and vertical correlation lengths, which are to a large extent responsible for the crossover from optical absorbing to reflecting behaviour as a function of wavelength. The position of this crossover can therefore be tuned in a simple way. An analogous tuning possibility for the width of the crossover regime is desirable for a better performance. Nevertheless, extremely black coatings can be produced for which the absorbance is broadband over a wide range of wavelengths. Applications other than in solar thermal systems are feasible, e.g. optical power measurement, back surface contacts for thin film solar cells, optoelectronics ...

The AlO_x consists of a mixture of aluminium and amorphous alumina as indicated by the label Al-Al_2O_3, whereby the bulk structure is not totally clear up to now. The XPS measurements identified a two-phase material and the UPS results gave evidence for the metallic nature. The best absorber properties were found at about $x \approx 0.4 \ldots 0.7$, i.e. oxygen contents of 30...40 at% as determined by XPS.

Between this absorber coating and the substrate usually a chemical interface builds up. For a Cu substrate, it consists of a Cu-Al-O alloy (appendices A and C), where the thickness of the interface decreases with increasing oxygen content. Indeed, it is the chemical bonding of the interfaces which presumably mediates the good adhesion to a lot of materials. Therefore, the feasibility of such coatings for different applications is imaginable.

Though a very high solar absorbance can be achieved by a pure rough AlO_x coating, it is reasonable to cover it with an additional layer. The motivation is both the enhanced absorbance by $\lambda/4$-interference and the improved aging stability. Three different top coatings were tested in the course of this work. Again, a chemically bonded interface forms in between the absorber and the cover layer. That interatomic bonds build up for an Al_2O_3 coating on top of the AlO_x is obvious. For hydrocarbon and fluorocarbon sealings the chemically bonded interface is evident from the photoelectron spectroscopy results.

The reflection properties of the AlO_x coatings rely on several effects. First, the material itself is slightly selective presumably because it is a cermet. Second, the very high solar absorbance is achieved by wavelength discrimination due to the roughness of the films. Third, the material itself acts as an infrared reflector, because it is metallic. Fourth, an antireflection coating was applied to improve the absorbance in the visible range. Therefore, most of the common methods to achieve spectral selectivity are incorporated.

The temperature resistance is promising for high temperature applications, with some differences for the three different top coatings. In contrast, the humidity aging properties for both Al_2O_3 and a-C:H coated samples are lousy. This is presumably the result of superwettable behaviour, i.e. a hydrophilic surface in connection with microroughness. However, super water repellence and *Lotus-effect* was found for a-C:F coated samples. The first results on the influence concerning the aging properties are promising.

Prospects

Even though a lot of answers have been given, many questions are open. For example, it is not clear if there is a chemical difference between mountains and valleys of the rough films. High resolution transmission electron microscopy and scanning Auger spectroscopy may give more insight.

An analysis of the surface structure over a wider range of parameters would certainly give us a better understanding of the interplay of surface diffusion and shadowing. In fact, at least five samples with distinct thickness have to be prepared for each parameter set to access information on the dynamical behaviour. A more detailed investigation on the growth angle for different substrate tilts would give additional hints on the growth mechanisms.

Angle dependent non-specular reflectance and *real-time* spectroscopic specular reflectance measurements may be additional optical probes for a better understanding of the interplay of roughness evolution and optical properties. Thereby, the experimental challenges should not be underestimated because some samples showed even an almost vanishing hemispherical reflectance over a wide spectral range.

Concerning optical applications, it would be very helpful to tailor the width of the crossover regime and to increase the humidity aging properties. Furthermore, because non-local properties have been proposed to guide the roughness properties, it is very important to check the upscaling possibility of this material. The reason lies in the sometimes unexpected abrupt changes in non-linear systems if one or several parameters are altered.

With the self-similar rough surface we were able to produce coatings with extreme wettability properties. Owing to the inherent dynamical scaling this surface may be a model system for a more fundamental research. Different correlation lengths are accessible and may be investigated for their influence on wetting of both hydrophilic and hydrophobic surfaces.

Bibliography

[1] A.-L. Barabási and H.E. Stanley: *Fractal Concepts of Surface Growth* (CAMBRIDGE University Press, 1995)

[2] D.J. Srolovitz, A. Mazor and B.G. Bukiet, *Analytical and numerical modeling of columnar evolution of thin films*, J. Vac. Sci. Technol A**6**, 2371 (1988)

[3] R.P.U. Karunasiri, R. Bruinsma and J. Rudnick, *Thin-film growth and the Shadow Instability*, Phys. Rev. Lett. **62**, 788 (1989)

[4] C. Tang, S. Alexander and R. Bruinsma, *Scaling Theory for the Growth of Amorphous Films*, Phys. Rev. Lett. **64**, 772 (1990)

[5] G.S. Bales and A. Zangwill, *Growth Dynamics of Sputter Deposition*, Phys. Rev. Lett. **63**, 692 (1989)

[6] G.S. Bales and A. Zangwill, *Macroscopic model for columnar growth of amorphous films by sputter deposition*, J. Vac. Sci. Technol A**9**, 145 (1991)

[7] P. Keblinski, A. Maritan, F. Toigo and J.R. Banavar, *Morphology and Scaling in Continuum Ballistic Deposition*, Phys. Rev. Lett. **74**, 1783 (1995)

[8] S.G. Mayr, M. Moske, M.E. Taylor, H.A. Atwater and K. Samwer, *The role of particle energy and pulsed particle flux in physical vapor deposition and pulsed-laser deposition*, Appl. Phys. Lett. **75**, 4091 (1999)

[9] S. Yan, Y. De-Quan and C. Jing-Zhong, *A morphology study of magnetron-sputtered Al films by atomic force microscopy*, Journal of Materials Science Letters **18**, 407 (1999)

[10] A.E. Lita and J.E. Sanches, *Characterization of surface structure in sputtered Al films: Correlation to microstructure evolution*, J. Appl. Phys. **85**, 876 (1999)

[11] L.J. Wan, B.Q. Chen, K.H. Kuo, *Morphology and microstructure of magnetron sputtering ion-plating Al films as a function of deposition time*, J. Vac. Sci. Technol. **A16**, 3160 (1988)

[12] R.W. Fane and W.E.J. Neal, *Optical Constants of Aluminum Films Related to the Vacuum Environment*, J. Opt. Soc. Am. **60**, 790 (1970)

[13] J.H. Halford, F.K. Chin and J.E. Norman, *Effects of vacuum deposition conditions on ellipsometric parameters, optical constants, and reflectance of ultrapure aluminum films*, J. Opt. Soc. Am. **63**, 790 (1970)

[14] C.H. Wang, W.C. Shih, R.E. Somekh, J.E. Evetts and D. Jackson, *Correlation of roughness, impurity, infra-red emissivity and sputter conditions for aluminium films*, Mat. Re. Soc. Symp. Proc. **354**, 523 (1995)

[15] M. Furukawa, Y. Yamamoto, H. Ikakura, N. Tanaka, M. Hashimoto, A. Sano and S. Shingubara, *Surface morphologies of sputter-deposited aluminum films studied using a high-resolution phase measuring laser interferometric microscope*, Applied Optics **35**, 701 (1996)

[16] W.D. Sproul, M.E. Graham, M.S. Wong, S. Lopes and D. Li, *Reactive direct current magnetron sputtering of aluminum oxide coatings*, J. Vac. Sci. Technol. **A13**, 1188 (1995)

[17] R.J. Kelly and R.D. Arnell, *Control of the structure and properties of aluminum oxide coatings deposited by pulsed magnetron sputtering*, J. Vac. Sci. Technol. **A17**, 945 (1999)

[18] B. Stauder, F. Perry and C. Frantz, *Chemical and structural analysis of aluminium-oxygen coatings obtained by d.c. magnetron reactive sputtering: some features of the process*, Surface and Coatings Technology **74-75**, 320 (1995)

[19] M.J. Verkerk and W.A.M.C. Brankaert, *Optical Properties of Reactively Evaporated Aluminium Films*, Journal of Materials Science Letters **6**, 115 (1987)

[20] D.R. Frear, A.N. Campbell, B.L. Draper and R.E. Mikawa, *Structure and Properties of Al-1%Si Thin Films on Si as a Function of Gas Impurities During DC Magnetron Sputtered Deposition*, Journal of Electronic Materials **18**, 517 (1989)

[21] A. Bergauer, H. Bangert, Ch. Eisenmenger-Sittner and P.B. Barna, *Whisker growth on sputtered AlSn (20 wt.%Sn) films*, Thin Solid Films **258**, 115 (1995)

[22] C.-C. Lee, D.T. Wei, J.-C. Hsu and C.-H. Shen, *Influence of Oxygen on some Oxide Films Prepared by Ion Beam Sputter Deposition*, Thin Solid Films **290-291**, 88 (1996)

[23] P. Würfel: *Physik der Solarzellen* (Spektrum Akademischer Verlag, Weinheim, Germany, 1995)

[24] B.O. Seraphin and A.B. Meinel, *Photothermal Solar Energy Conversion and the Optical Properties of Solids*, in: *Optical properties of solids*, edited by B.O. Seraphin (North-Holland, Amsterdam, 1976)

[25] O.P. Agnihotri, B.K. Gupta: *Solar Selective Surfaces* (JOHN WILEY & SONS, New York, 1981)

[26] C.G. Granquist and V. Wittwer, *Materials for solar energy conversion: An overview*, Solar Energy Mat. and Solar Cells **54**, 39 (1998)

[27] M.F. MacMillan, R.P. Devaty and J.V. Mantese, *Infrared properties of Pt/Al_2O_3*, Phys. Rev. **B43**, 13838 (1991)

[28] G.A. Niklasson and C.G. Granquist, *Optical properties and solar selectivity of coevaporated $Co\text{-}Al_2O_3$ composite films*, J. Appl. Phys. **55**, 3382 (1984)

[29] Q.C. Zhang, *Stainless steel in AlN by direct current magnetron sputtering technology*, Solar Energy Mat. and Solar Cells **52**, 95 (1998)

[30] H. Nakashima, M. Yonekura, H. Wakabayashi and M. Kominami, *Application of silver-dispersed AlN thin film to solar control glass*, J. Appl. Phys. **84**, 6287 (1998)

[31] R. Gampp: *Deposition und Characterisierung von metallhaltigen, amorphen Kohlenwasserstoffilmen zur Anwendung in Sonnenkollektoren*, VDI Fortschrittberichte, Reihe **5**, Nr.446 (VDI Verlag, Düsseldorf, 1996)

[32] A. Schüler, J. Geng, P. Oelhafen, S. Brunold, P. Gantenbein and U. Frei, *Application of titanium containing amorphous hydrogenated carbon films (a-C:H/Ti) as optical selective solar absorber coatings*, Solar Energy Mat. and Solar Cells **60**, 295 (2000)

[33] V.M. Shalev, *Electromagnetic properties of small-particle composites*, Physics Reports **272**, 62 (1996)

[34] H.G. Craighhead, B. Bartynski, R.A. Buhrmann, L. Wojcik and A.J. Sievers, *Metal/Insulator composite selective absorbers*, Solar Energy Mat. **1**, 105 (1979)

[35] R. Joerger, R. Gampp, A. Heinzel, W. Graf, M. Köhl, P. Gantenbein and P.Oelhafen, *Optical properties of inhomogeneous media*, Solar Energy Mat. and Solar Cells **54**, 351 (1998)

[36] P. Sheng, *Theory for the dielectric function of granular composite media*, Phys. Rev. Lett. **45**, 60 (1980)

[37] G.D. Mahan, *Long-wavelength absorption of cermets*, Phys. Rev. **B38**, 9500 (1988)

[38] A. Schüler, C. Ellenberger, P. Oelhafen, C. Haug and R. Brenn, *Optical properties of titanium containing amorphous hydrogenated carbon films (a-C:H/Ti)*, J. Appl. Phys., in press

[39] C. Ellenberger: *In situ Laserreflektometrie*, diploma thesis, University of Basel (1998)

[40] K.M. Debe, *Composite article comprising oriented microstructures*, US patent No. 5645929 (1997)

[41] R. Kuehn, V. Mikelsons and G.L. Dorer, *Radiation absorbing surfaces*, US patent No. 4582111 (1983)

[42] R. Kuehn, V. Mikelsons and G.L. Dorer, *Radiation absorbing surfaces*, US patent No. 4396643 (1983)

[43] H.G. Craighead and R.E. Howard, *Light-absorbing materials*, US patent No. 4284689 (1981)

[44] T. Kudo, M. Watase and A. Kanesaki, *Selective solar energy absorber*, GB patent No. 2102025 (1982)

[45] C.E. Johnson, *Ultra-black coating due to surface morphology*, US patent No. 4361630 (1982)

[46] J.J. Cuomo, J.M. Woodall and J.F. Ziegler, *Photon energy converter*, US patent No. 4005698 (1976)

[47] J. Eitle: *Characterization of solar selective surfaces at high temperatures*, PhD thesis, University of Basel (1992)

[48] P. Beckmann and A. Spizzichino: *The Scattering of Electromagnetic Waves from Rough Surfaces*, Pergamon, New York (1963)

[49] A.A. Maradudin and D.L. Mills, *Scattering and absorption of electromagnetic radiation by semi-infinite medium in the presence of surface roughness*, Phys. Rev. **B11**, 1392 (1975)

[50] S.K. Sinha, E.B. Sirota, S. Garoff and H.B. Stanley, *X-Ray and neutron Scattering from Rough Surfaces*, Phys. Rev. **B38**, 2297 (1988)

[51] J.M. Elson and J.M. Bennett, *Calculation of the power Spectral Density from Surface Profile Data*, Appl. Opt. **34**, 201 (1995)

[52] J.M. Elson, *Theory of light scattering from a rough surface with inhomogeneous dielectric permittivity*, Phys. Rev. **30**, 5460 (1984)

[53] P. Wong and A.J. Bray, *Scattering by Rough Surfaces*, Phys. Rev. **B37**, 7751 (1988)

[54] H.-N. Yang, T.-M. Lu and G.-C. Wang, *Diffraction from Surface Growth Fronts*, Phys. Rev. **B47**, 3911 (1993)

[55] J.Krug: *Die Entstehung fraktaler Oberflächen* (Verlag Harri Deutsch, Thun, Frankfurt am Main, 1990)

[56] F. Family and T. Vicsek, *Scaling of the active zone in the Eden process on percolation networks and the ballistic deposition model*, J. Phys. **A18**, L75 (1985)

[57] M. Plischke and Z. Rácz, *Dynamic scaling and the surface structure of Eden clusters*, Phys. Rev. **A32**, 3825 (1985)

[58] J. Krim and J.O. Indekeu, *Roughness exponents: A paradox resolved*, Phys. Rev. **E48**, 1579 (1993)

[59] M. Eden, in *Proceedings of the Fourth Berkley Symposium on Mathematical Statistics and Probability. Volume IV: Biology and Problems of Health*, ed. By J. Newman, University of California Press, Berkeley (1961)

[60] S.D. Sarma and P. Tamborena, *A New Universality Class for Kinetic growth: One-Dimensional Molecular-Beam Epitaxy*, Phys. Rev. Lett. **66**, 325 (1991)

[61] S.F. Edwards and D.R. Wilkinson, *The Surface Statistic of a Granular Aggregate*, Proc. R. Soc. London A**381**, 17 (1982)

[62] M. Kardar, G. Parisi and Y.C. Zhang, *Dynamic Scaling of Growing Interfaces*, Phys. Rev. Lett. **56**, 889 (1986)

[63] J.G. Amar and F. Family, *Phase Transition in a Restricted Solid-on-Solid Surface-Growth Model in 2+1 Dimensions*, Phys. Rev. Lett. **64**, 543 (1990)

[64] J.M. López, *Scaling Approach to Calculate Critical Exponents in Anomalous Surface Roughening*, Phys. Rev. Lett. **83**, 4594 (1999)

[65] A.G. Dirks and H.J. Leamy, *Columnar Microstructure in Vapor-Deposited Thin Films*, Thin Solid Films **47**, 219 (1977)

[66] R. Messier and E. Yehoda, *Geometry of thin-film morphology*, J. Appl. Phys. **58**, 3739 (1985)

[67] J.A. Thornton, *Influence of apparatus geometry and deposition conditions on the structure and topography of thick sputtered coatings*, J. Vac. Sci. Technol. **11**, 666 (1974)

[68] D.L. Chambers, C.T. Wan, G.T. Susi and K.A. Taylor, *Sputter deposition of aluminium and other alloys at cryogenic temperatures*, J. Vac. Sci. Technol. **A7**, 1305 (1988)

[69] S. Park, B. Khang, H. Jeong and A.-L. Barabási, *Dynamics of Ripple Formation in Sputter Erosion: Nonlinear Phenomena*, Phys. Rev. Lett. **83**, 3486 (1999)

[70] R. Cuerno and A.-L. Barabási, *Dynamic Scaling of Ion-Sputtered Surfaces*, Phys. Rev. Lett. **74**, 4746 (1995)

[71] M.A. Makeev and A.-L. Barabási, *Effect of Surface Roughness on the Secondary Ion Yield in Ion Sputtering*, Appl. Phys. Lett. **73**, 1445 (1998)

[72] S. Rusponi, G. Constantini, F. Buatier de Mongeot, C. Boragno and U. Valbusa, *Patterning a surface on the nanometric scale by ion sputtering*, Appl. Phys. Lett. **75**, 3318 (1999)

[73] E.A. Eklund, E.J. Snyder and R.S. Williams, *Correlation from randomness: quantitative analysis of ion-etched graphite surfaces using scanning tunnel microscope*, Surf. Sci **285**, 157 (1993)

[74] X. Wang, X.H. Liu, S.C. Zou, P.J. Martin and A. Bendavid, *Atomic force microscopy study on topography of films produced by ion-based techniques*, J. Appl. Phys. **80**, 2658 (1996)

[75] H. You, R.P. Chiarello, H.K. Kim and K.G. Vandervoort, *X-ray Reflectivity and Scanning-Tunneling-Microscope Study of Kinetic Roughening of Sputter-Deposited Gold Films during Growth*, Phys. Rev. Lett. **70**, 2900 (1993)

[76] C.V. Dharmadhikari, A.O. Ali, N. Suresh, D.M. Phase, S.M. Chaudhari, V. Ganesan, A. Gupta and B.A. Dasannacharya, *Dynamic scaling in growth of platinum films on Si(100)*, Solid State Communications **114**, 377 (2000)

[77] W.S. Wu and W.W. Webb, *Critical Liquid-Vapor Interface in* SF_6, Phys. Rev. **A8**, 2065 (1973)

[78] G.A. Held, J.L. Jordan-Sweet and P.M. Horn, *X-Ray Scattering Study of the Thermal Roughening of Ag(110)*, Phys. Rev. Lett. **59**, 2075 (1987)

[79] C. Thompson, G. Palasantzas, Y.P. Feng, S.K. Sinha and J. Krim, *X-Ray Reflectivity Study of the Growth Kinetics of Vapor-deposited Silver Films*, Phys. Rev. **B49**, 4902 (1994)

[80] G.J. Pietsch and M. Henzler, *Continuous Roughness Characterization from Atomic to Micron Distances: Angle-Resolved Electron and Photon Scattering*, Appl. Surf. Sci **39**, 457 (1989)

[81] J.M. Elson and J.M. Bennett, *Relation between the angular dependence of scattering and the statistical properties of optical surfaces*, J. Opt. Soc. Am. **69**, 31 (1979)

[82] Y. Wang and W.L. Wolfe, *Scattering from microrough surfaces: comparison of theory and experiment*, J. Opt. Soc. Am. **73**, 1596 (1983)

[83] E. Chason, M.B. Sinclair, J.A. Floro, J.A. Hunter and R.Q. Hwang, *Spectroscopic light scattering for real-time measurements of thin film and surface evolution*, Appl. Phys. Lett. **72**, 3276 (1998)

[84] J.B. Webb: *Formation of Thin Semiconducting Films by Magnetron Sputtering*, in: *Thin Films from Free Atoms and Particles* (Academic Press Inc., 1985)

[85] A. Schüler and P. Oelhafen, *Photoelectron spectroscopic characterization of titanium containing amorphous hydrogenated silicon carbon films (a-$Si_{1-x}C_x$:H/Ti)*, to be published

[86] S. Springer: *Characterization of Al-Ni-Si-oxides produced by magnetron sputtering for their potential application as solar absorber coatings*, diploma thesis, University of Basel (1999)

[87] J. Sellers, *Asymmetric Bipolar Pulsed DC*, ENI Technical Note, New York (1996)

[88] M.E. Graham and W.D. Sproul, *Pulsed-DC reactive sputtering - new opportunities*, Society of Vacuum Coaters 37th Conference Proceedings, 13 (1994)

[89] C.S. Bhatia, G. Guthmiller and A.M. Spool, *Alumina films by sputter deposition with Ar/O_2: Preparation and characterization*, J. Vac. Sci. Technol. **A7**, 1298 (1989)

[90] W.E. Spicer, *Photoemissive, Photoconductive, and Optical Absorption Studies of Alkali-Antimony Compounds* Phys. Rev. **112**, 114 (1964)

[91] S. Hüfner: *Photoelectron Spectroscopy: Principles and Applications*, 2nd ed. (Springer-Verlag, Berlin, 1996)

[92] M. Cardona and L. Ley (eds.): *Photoemission in Solids I, General Principles* (Springer-Verlag, Berlin, 1978)

[93] A. Messiah: *Quantum Mechanics* (North Holland, Amsterdam, 1961)

[94] J.H. Scofield, *Hartree-Slater subshell photoionization cross-sections at 1254 and 1487 eV*, Electron Spectroscopy and Related Phenomena **8**, 129 (1976)

[95] M.P. Seah and W.A. Dench, *Quantitative electron spectroscopy of surfaces: a standard data base for electron inelastic mean free paths in solids*, Surface and Interface Analysis **1**, 2 (1979)

[96] P.M.Th.M. van Attekum and J.M. Trooster, *Removal of X-ray satellites from Mg $K\alpha$ excited photoelectron spectra*, J. Electron Spectroscopy and Related Phenomena **11**, 363 (1977)

[97] D.A. Shirley, *High-Resolution X-Ray Photoemission Spectrum of the Valence Bands of Gold*, Phys. Rev. **B5**, 4709 (1972)

[98] S. Doniach and M. Šunjić, *Many-electron singularity in X-ray photoemission and X-ray line spectra from metals*, J. Phys. **C3**, 285 (1970)

[99] G.D. Mahan, *Collective excitations in x-ray spectra of metals*, Phys. Rev. **B11**, 4814 (1975)

[100] V.R. Weidner, J.J. Hsia and B. Adams, *Laboratory intercomparison study of pressed polytetrafluoroethylene powder reflectance standards*, Appl. Optics **24**, 2225 (1985)

[101] B. Carlson, M. Köhl and U. Frei, *Accelerated Life Testing of Solar Energy Materials, case study of some selective absorber coating materials for DHW systems, a report of Task X Solar Materials Research and Development*, IEA (1994), copies available at: Swedish National Testing and Research Institute, Borås, Sweden

[102] S. Zhu, F. Wang and W. Wu, *Simulations of reactive sputtering with constant voltage power supply*, J. Appl. Phys. **84**, 6399 (1998)

[103] W.D. Kingery, H.K. Bowen and D.R. Uhlmann: *Introduction to Ceramics*, 2nd ed. (WILEY INTERSCIENCE, New York, 1976)

[104] R. Reiche, F. Yubero, J.P. Espinós and A.R. González-Elipe, *Structure, microstructure and electronic characterisation of the Al_2O_3/SiO_2 interface by electron spectroscopies*, Surface Science **457**, 199 (2000)

[105] H.E. Bennett, *Specular Reflectance of Aluminized Ground Glass and the Height Distribution of Surface Irregularities*, J. Opt. Soc. Am. **53**, 1389 (1963)
H.E. Bennett and J.O. Porteus, *Relation Between Surface Roughness and Specular Reflectance at Normal Incidence*, J. Opt. Soc. Am. **51**, 123 (1961)

[106] E.L. Church, H.A. Jenkinson and J.M. Zavada, *Relationship between Surface Scattering and Microtopographic Features*, Phys. Rev. **B47**, 3911 (1993)

[107] F. Szmulowicz and B. Segall, *Calculation of optical spectra of aluminium*, Phys. Rev. **B24**, 892 (1981)

[108] W. Zahn and A. Zösch, *The dependence of fractal dimension on measuring conditions of scanning probe microscopy*, Fresenius J. Anal. Chem. **365**, 168 (1999)

[109] G. Rasigni, F. Varnier, M. Rasigni, J.P. Palmari and A. Llebaria, *Autocovariance functions, root-mean-square-roughness height, and autocovariance length for rough deposits of copper, silver, and gold*, Phys. Rev. **B25**, 2315 (1982)

[110] M. Rasigni, G. Rasigni, J.P. Palmari and A. Llebaria, *Study of surface roughness using a microdensitometer analysis of electron micrographs of surface replicas: I. Surface profiles*, J. Opt. Soc. Am.**71**, 1124 (1981)

[111] *JCPDS powder diffraction files*, International Centre for Diffraction Data (ICDD), USA (1996)

[112] B.D. Cullity: *Elements of X-RAY DIFFRACTION*, Addison-Wesley Publishing (1978)

[113] R. Hauert, J. Patscheider, M. Tobler and R. Zehringer, *XPS investigation of the a-C:H/Al interface*, Surface Science **292**, 121 (1993)

[114] K.-H. Ernst, J. Patscheider and R. Hauert, *XPS investigation of the a-C:H/Al_2O_3 interface*, Surface and Interface Analysis **21**, 32 (1994)

[115] H.L. Rosano, W. Gerbacia, M.E. Feinstein and J.W. Swaine, Jr., *Determination of the Critical Surface Tension Using an Automatic Wetting Balance*, Surface and Interface Analysis **21**, 32 (1994)

[116] W. Barthlott and C. Neinhuis, *Purity of the sacred lotus, or escape from contamination in biological surfaces*, Planta **202**, 1 (1997)

[117] R. Fürstner, C. Neinhuis and W. Baethlott, *Der Lotus-Effekt: Selbstreinigung mikrostrukturierter Oberflächen*, Nachrichten aus der Chemie **48**, 24 (2000)

[118] T. Onda, S. Shibuichi, N. Satoh and K. Tsujii, *Super-Water-Repellent Fractal Surfaces*, Langmuir **12**, 2126 (1996)

[119] R.H. Dettre and R.E. Johnson, Jr., *Contact Angle Hysteresis, II. Contact Angle Measurements on Rough Surfaces*, Advances in Chemistry **43**, 136 (1963)

[120] A.B.D. Cassie and S. Baxter, *Wettability of Porous Surfaces*, Trans. Faraday Soc. **40**, 546 (1944)

[121] M. Horie, *Plasma-structure dependence of the growth mechanism of plasma-polymerized fluorocarbon films with residual radicals*, J. Vac. Sci. Technol. **A13**, 2490 (1995)

[122] H.V. Boenig, *Plasma Science and Technology*, Cornell University Press, New York (1982).

[123] S. Agraharam, D.W. Hess, P.A. Kohl and S.A. Bidstrup Allen, *Plasma chemistry in fluorocarbon film deposition from pentafluoroethane/argon mixtures*, J. Vac. Sci. Technol.**A17**, 3265 (1999)

[124] J. Fink, N. Nücker, R.E. Sah, P. Koidl, H. Baumann and K. Bethge, *Composition and structure of plasma deposited a-C:H,F films*, Proceedings of the E-MRS Meeting **XVII**, 475 (1987)

[125] J. Geng, G. Gantner, P. Oelhafen and P.K. Datta, *Initial oxidation of Ti-Al intermetallics: An in situ MXPS study*, Applied Surface Science 158, 64 (2000)

[126] L. Golubović and R. Bruinsma, *Surface Diffusion and Fluctuations of Growing Interfaces*, Phys. Rev. Lett. **66**, 321 (1991)

[127] I. Hodgkinson, Q. H. Wu and A. McPhun, *Incremental-growth model for the deposition of spatially modulated thin film nanostructures*, J. Vac. Sci. Technol. **A16**, 2811 (1998)

[128] R. Messier, V.C. Venugopal and P.D. Sunai, *Origin and evolution of sculptured thin films*, J. Vac. Sci. Technol. **A18**, 1538 (2000)

[129] M. Kardar, *Roughening By Impurities At Finite Temperatures*, Phys. Rev. Lett. **55**, 2923 (1985)

[130] D.A. Huse and C.L. Henley, *Pinning Roughening of Domain Walls in Ising Systems Due to Random Impurities*, Phys. Rev. Lett. **54**, 2708 (1985)

[131] R. Buzio, E. Gnecco, C. Boragno, U. Valbusa, P. Piseri, E. Barborini and P. Milani, *Self-affine properties of cluster-assembled carbon thin films*, Surface Science **444**, L1 (2000)

[132] R.C. Ross and R. Messier, *Microstructure and properties of rf-sputtered amorphous hydrogenated silicon films*, J. Appl. Phys. **52**, 5329 (1981)

[133] R.C. Ross and R. Messier, *Reactive sputtering of amorphous silicon in Ne, Ar and Kr*, J. Appl. Phys. **54**, 5744 (1983)

[134] A.J. Pedraza, J.D. Fowlkes and D.H. Lowndes, *Silicon microcolumn arrays grown by nanosecond pulsed excimer laser irradiation*, Appl. Phys. Lett. **74**, 2322 (1999)

Related articles:

Appendix A

Optical selective coatings based on microstructured aluminium oxide

J. Geng, P. Oelhafen, D. Mathys, M. Düggelin, R. Guggenheim, S. Brunold and P. Gantenbein

published in:
Proceedings of the EUROSUN2000 Congress, June 2000, Copenhagen (Denmark)

Appendix B

Changing TiN film morphology by plasma biasing

J. Geng, A. Schüler, P. Oelhafen, P. Gantenbein, M. Düggelin, D. Mathys and R. Guggenheim

published in:
Journal of Applied Physics **86**, 3460 (1999)

Appendix C

Photoelectron Spectroscopy Study of Al-Cu Interfaces

J. Geng and P. Oelhafen

published in:
Surface Science **452**, 161 (2000)

Appendix D

A Photoelectron Spectroscopy Study of Ti/Cu Interfaces

J. Geng, A. Schüler, P. Reinke and P. Oelhafen

published in:
Journal of Applied Physics **84**, 2876 (1998)

Acknowledgments

This last section is *not* written because it is just *habit* to do so – it is a pleasure for me.

I am grateful to Prof. Dr. Peter Oelhafen who gave me the opportunity to work in his group. He was an ever open-minded adviser and rendered it possible to do my research in a rather self-employed way.

I want to thank Prof. Dr. Ernst Meyer for his interest in my work and that he took over responsibility for the 2nd report (*Koreferat*) on this thesis.

Dr. Andreas Schüler initiated me into the secrets of plasma deposition techniques, became always enthusiastic on principle physical problems and was a major source of inspiration. In the course of all the ups and downs I made friends with him.

Indeed, from the very beginning to the very end of my time in the group I was surrounded by friends: Dr. Thormen Wrase, Ralf Wahrenberg, Matthias Töwe, Dr. Teresa de los Arcos, Ivan Videnovic, Shui Ching Ho, Dr. habil. Petra Reinke, Dr. Gilbert Francz, Alain Gremaud, Dr. Yvette Kuster, Dr. Holger Stupp, Dr. Gerhard Gantner, Dr. Michael Gunnar Garnier, Dr. Roland Kilper, Simon Springer, Christoph Ellenberger and all the former group members sometimes visiting our laboratory. Roland Steiner is especially acknowledged, because he was always a helpful address not only for technical problems.

The coworking with Prof. Dr. R. Guggenheim, Daniel Mathys and Marcel Düggelin from the SEM laboratory Basel opened the door to the fascinating field of surface roughness: Thank you!

Surface topography investigations without *scanning probe techniques* in Basel? Unthinkable! I am grateful for the experts' support from Verena Thommen and Peter Reimann.

Dr. Paul Gantenbein, Stefan Brunold and Ueli Frei from the SPF Rapperswil were always present if some accelerated aging and/or optical investigations exceeding our possibilities were necessary. In addition, valuable discussions and advice pushed my work further.

I am pleased that I met Prof. Dr. Santu Datta from the University College Northumbria at Newcastle (UK). We had a fruitful coworking on an applied project ([125], not included in the present report) and I spent a few nice days with him in *The North* of England.

All experimental research would be impossible without technical help. Many thanks to all the mechanical and electronical experts in the institute. I want to acknowledge also the administrative helpers, especially our secretary Francois Erkadoo.

What would I be without my family's support and a lot of good old friends? I better do not think about it. Special thanks are dedicated to my parents Fritz and Rita, my brothers Reiner and Norbert – and to Reni.

Last but not least, I am grateful for the financial grants from the *Swiss Federal Office of Energy* and the *Swiss National Science Foundation*.

I owe my academical education to the following university teachers:

- Dr. M. Sohn, Prof. Dr. G. Weiss, Prof. Dr. F. Baumann, Prof. Dr. H. v. Löhneysen, Prof. Dr. C. Schmid, Prof. Dr. P. Wölfle, Prof. Dr. P. Würfel, Prof. Dr. G. Schön, Prof. Dr. E. Dormann, Prof. Dr. F. Hermann, Prof. Dr. J. Kühn, Prof. Dr. R. Decker, Prof. Dr. R. Rupp, Dr. O. Knab, Prof. Dr. R. v. Baltz, Prof. Dr. Th. Mannel, Prof. Dr. K. Hümmer, Prof. Dr. B. Zeitnitz, Dr. habil. N. Geng (Universität Fridericiana zu Karlsruhe)
- Prof. Dr. P. Oelhafen, Dr. habil. H.-G. Boyen, Dr. habil. P. Reinke, Prof. Dr. E. Meyer, Prof. Dr. C. Bruder (Universität Basel)